Seeing through the smoke:

using airborne or ground-based consumer-grade DSLR cameras in fire monitoring

by

Mirahmad Chabok

Thesis
Submitted to Flinders University
for the degree of

Doctor of Philosophy

College of Science and Engineering

August 2019

Table of Contents

Summary

In this research, a simple and novel solution is designed to reduce the smoke and haze effect on imagery acquired using consumer grade Digital Single Lens Reflex (DSLR) cameras that, after modification, might be mounted on unmanned aerial vehicles, manned aircraft or be captured from the ground. The presence of substantial amounts of haze or gaseous smoke particles, caused for example by an active bushfire at the time of data capture, dramatically reduces image visibility and quality due to electromagnetic radiation being scattered by atmospheric particulates. Although most modern hyperspectral and thermal imaging sensors can capture a large number of narrow range bands of the shortwave and thermal infrared spectral range, and therefore have the ability to penetrate smoke and haze well, the resulting images do not contain sufficient spatial detail to enable important objects to be located or to assist in search and rescue.

First, this research investigates the limitations of existing methods for penetrating smoke, and image visibility enhancement techniques. For example, many recently developed algorithms exploit the differences between two or more images of the same scene that have different properties. These approaches require exact co-registration of the images captured using multiple sensors which is a non-trivial step in the processing workflow and therefore are not applicable to dynamic scenes in airborne applications where ground objects and smoke particles can move quickly relative to each other.

Secondly, it examines multispectral, thermal and visible wavelength images collected over bushfire smoke to simulate and evaluate the main hypothesis of this research, i.e., the feasibility of using DSLR camera sensors for smoke penetration. The results from this simulation phase confirmed the research hypothesis and helped form the future research design methodology and structure.

Thirdly, based on achieved feasibility confirmation and results from previous sections the research investigates and verifies the spectral sensitivity of unmodified and modified DSLR camera sensors by taking measurements in a controlled laboratory environment with a spectroradiometer. The results show that DSLR camera sensors, after modification, can collect enough information between 700 nm – 1100 nm (the near infrared) that the resulting image data will, theoretically, be less affected by smoke and haze based on Rayleigh scattering theory.

Fourthly, an optical filter was designed to preserve the semi-natural colour appearance of the captured photographs while collecting near infrared radiation simultaneously with visible blue and green light. A custom-designed filter was manufactured so that it would allow visible blue, visible green and infrared radiation between 950 nm and 1100 nm to pass. Its spectral responsivity was verified and confirmed using laboratory spectroradiometry. The custom-designed filter enabled the camera to collect these three bands simultaneously without any co-registration requirement or any major negative effects on the visual appearance of the captured imagery.

Finally, a smoke penetration algorithm (SPA) was developed to enable effective scene visibility enhancement by eliminating or minimizing the smoke effect from collected data. This modified camera and custom-designed filter were used to collect data on the ground and on an aircraft flown over areas covered by smoke and results processed using the SPA. The final processed results as an outcome of SPA, show significant improvements in visibility confirming the efficiency of the proposed method.

Declaration

I certify that this thesis does not incorporate, without acknowledgment, any material previously submitted for a degree or diploma in any other university; and that to the best of my knowledge and belief it does not contain any material previously published or written by another person except where due reference is made in the text.

Mirahmad Chabok

Acknowledgments

First and foremost, I offer my sincere gratitude to my supervisor, Prof. Andrew Millington, for his mentorship, constructive advice, expert comments and his support in writing this thesis over the last four years and specially dedicating his time after retirement and thoughtfully reviewing the additions and corrections. I learnt a lot during my research from him and wouldn’t be able to finalize this research without his guidance. I also wish to thank my co-supervisor Prof. Jörg M. Hacker who encouraged me from beginning and all through my research. Special thanks to Airborne Research Australia (ARA) and Dr. Andrew McGrath who helped in collecting aerial data and installing the camera system on their aircraft and providing access to previously collected thermal and multi-spectral aerial data from bushfires.

I would also like to thank to the postgraduate student Chun Song who helped in conducting laboratory and spectrometry data collection and Dr. Rachel S. Popelka-Filcoff from the former School of Chemistry and Physical Sciences for access to the spectrometer.

Many thanks to the two external examiners of this thesis who identified some omissions that I have hopefully rectified. I would also like to thank all of my friends who contributed in some way to this research, particularly the people I worked with at Dronemetrex and the PhD students in the ‘Land Lab’ in the former School of the Environment at Flinders University.

Special thanks to Jen Pitman, senior ranger at Belair National Park, for having me in their prescribed burn safety briefing and granting access to the burn area for ground-based data collection.

Moreover, I express my deepest appreciation to my beautiful and lovely wife Shima, not necessarily for supporting me in all of our difficult moments, but for her patience, understanding and dedicating her full time in looking after our life’s blessing, Adrian. I

dedicate this dissertation to my wife, Shima and my son Adrian who have been my primary motivation. I'd also like to thank my family for their endless love and support throughout my life.

Finally, and most importantly, thanks to God for everything in my life, for blessings and lessons.

List of Figures

List of Tables

List of Acronyms and Abbreviations

AGL	Above Ground Level
ASD	ASD Inc. FieldSpec4® Hi-Res Spectrometer
CCD	Charge Coupled Device
CFA	Colour Filter Array
CMOS	Complementary Metal-oxide-Semiconductor
DCP	Dark Channel prior
DN	Digital Number
DOS	Dark Object Subtraction
DSLR	Digital Single-lens Reflex Camera
DSM	Digital Surface Model
EMR	Electromagnetic Radiation
EMS	Electromagnetic Spectrum
FOV	Field of View
IFOV	Instantaneous Field of View
InGaAs	Indium-Gallium-Arsenic
LWIR	Long-Wave-Infrared
MODIS	Moderate Resolution Imaging Spectrometer
mpixel	Mega Pixel
MWIR	Mid-Wave-Infrared
NDVI	Normalized Differential Vegetation Index
NIR	Near Infrared
QE	Quantum Efficiency
RADAR	Radio Detection and Ranging
RGB	Red, Green and Blue
SI	Silicon
SPA	Smoke Penetration Algorithm
SWIR	Short-wave-infrared
TFOV	Total Field of View
TIR	Thermal Infrared
TV	Total Variation
UAV	Unmanned Aerial Vehicle
UV	Ultra Violet

List of Symbols

$B_{(i,j)}$, $G_{(i,j)}$ and $NIR_{(i,j)}$	Blue, green and near-infrared values at pixel location i&j of input image
$\%T_{\lambda}$	Light Transmission Percentage
$I_{(i,j)}$	Input Image Covered by Smoke
$J_{(i,j)}$	Smoke-free Image
$J_{(i,j)}^{dark}$	Dark Channel of Colour Image
$t_{(i,j)}$	Medium Transmission
$t'_{(i,j)}$	Medium Transmission for the Local Patch
t_0	Minimum Medium Transmission Value
A/W	Relative Responsivity
Io	Incident light Intensity
^{o}K	Degree Kelvin
nm	Nano Meter
v	Volt
W	Watt
λ	Wavelength
µm	Micrometer
ω	Optional Haze Constant Parameter
$\Omega(i,j)$	Local Patch
a	Path Radiance

Chapter 1

Introduction

1. Introduction

1.1. Background

Optical airborne sensors are being widely used for collecting aerial images and spatial information for a wide array of applications. Data collected using this technology is being used for surveillance, topographic mapping, monitoring and many other applications. However, this technology is not easily applied to a non-clear atmosphere that is polluted by optically active substances such as gaseous smoke particulates in (Figure 1.1). Smoke from wildfires, also known as bushfires in Australia, can affect people, animals and plants. Fire is important natural phenomena in ecosystems throughout the planet. In certain climate zones, seasonal moisture accelerates the lush growth resulting in regular burn, whilst in some other zones, because of a scarcity of fuel, fires are infrequent. Its importance is underlined by the estimate that if there were no fire, forest cover could increase to over 50 percent of the vegetated land surface (Bond et al. 2004; Bowman 2005).

Image has been removed due to copyright restriction.

Figure 1.1. An aerial image captured by a typical consumer-grade digital camera from the Mt. Bolton Bushfire Victoria, February 2016 that shows how smoke can impact visibility. (The Courier 2016).

Major bushfires emit considerable quantities of trace gases and contaminants (Michel et al. 2005; Giglio et al. 2006; Chelsea et al. 2016), and such emissions are thought to greatly influence the chemical makeup of the air (Voulgarakis & Field 2015) along with the planet's climate system. The vast variety of emitted gases are generated by fire and these include carbon dioxide (CO_2), carbon monoxide (CO), methane (CH_4), nitrogen oxide (NO), non-methane volatile organic carbon compounds (NMVOCs) and nitrogen oxides (NOx): as well as fine particulate matter including organic carbon (OC) and white black carbon (BC) (Crutzen & Andreae, 1990; Andreae & Merlet, 2001). Bushfire emissions contribute to air pollution and can impair visibility (Hyde et al. 2017) by raising the quantity of pollutants (NWCG 2014), and can impact safe driving conditions on the ground. The quantity and chemical composition of these emissions coupled with fire plume dynamics and meteorological conditions can also impact the air quality (Hyde et al. 2017). Smoke from burning bushland is therefore a complex combination of aerosols and gases. The quantity and composition of the emissions is dependent on a vast range of factors associated with fuel characteristics (e.g., fuel form, structure, loading, chemistry, moisture) and fire behaviour (Religious et al. 2003).

Records of bushfires in Australia extend back to 1850, with over 700 fatalities having been recorded since in approximately a century and a half (Blong 2005). With the advances in optical digital camera technology to collect high spatial resolution imagery, there is both a need and an opportunity for effective exploitation of data from bushfires (and industrial and house fires). Hence, image processing technologies need to be developed concurrently in order to provide the best possible intelligence for decision makers in emergency situations such as these

1.2. Problem Statement

Fire is regarded as an oxidizing agent that produces a new kind of matter by combining another lump of matter with oxygen (Connelly & Geiger 1996). This rapid process generates additional heat that is enough to sustain the fire until all the fuel is consumed. During a bushfire, vegetation can release the solar energy collected over many years in just few minutes; this rapid decomposition produces carbon compounds because carbon dioxide combines with water (Thomas & McAlpine 2010, p. 3).

Depending on the size, morphology, orientation and distribution of smoke particles the light pathways can be changed considerably (Qiyuan et al. 2007). Light scattering is one of the major physical processes that contributes to the visible appearance of the captured image and its properties can be computed using the Maxwell’s equation (Mishchenko, Travis & Lacis 2002). According to the Maxwell’s electromagnetic theory, the shape of small particles has a direct influence on the light scattering properties. Figure 1.2. shows photographs of smoke particles captured by a scanning electron microscope (SEM) and shows that smoke particles from four different materials are typically distributed as a chain-like string. Each string is comprised of many primary spherical-shaped particles and this contributes to the light scattering model. The combustion style and fuel type affect the reflective index of smoke particles and are also major contributor to the light scattering phenomena (Smyth & Shaddix 1996).

Image has been removed due to copyright restriction.

Figure 1.2. SEM photographs of smoke particles generated from a: a) pyrolyzing wood fire, b) smouldering cotton fire, c) polyurethane foam fire, and d) flaming heptane fire. (Qiyuan et al. 2007)

Based on independent measurements by various researchers (e.g., Qiyuan, Hongyong, Liwei 2007; Xiang et al. 2014) smoke particle diameters range from 0.01 to 1.3 μm. This indicates that smoke particles will have a lesser impact on the sensors exploiting longer wavelengths in visible and infrared parts of the EMS. In the past few years, advances in airborne remote sensing technologies have made it possible to image beyond the limitation of optical sensors by utilizing short wave infrared (SWIR) from 1400 nm – 3000 nm, middle wave infrared (MWIR) from 3000 nm – 8000 nm or long wave infrared (LWIR) from 8000 nm – 15000 nm (Byrnes 2009). Although this capability allows sensors to penetrate smoke, clouds, fog and to see through other particles; some of the merit points in utilizing these sensors for seeing through smoke are listed as follows:

- Relatively low achievable spatial resolution
- Mono-colour imaging sensor
- Complex postproduction requirement
- Narrow field of view and ground coverage

- Accessibility and relatively high cost

The presence of substantial gaseous smoke particles, caused for instance by an active bushfire, at the time of data capture using a typical DSLR camera dramatically reduces the image visibility and quality. The large volumes of smoke and ash dispersed into the atmosphere complicate aerial missions, e.g., search-and-rescue operations and targeted aerial water bombing, due to diminished visibility. The ability to have high spatial resolution vision through gaseous smoke emanating from an active fire to the ground beneath is a critical factor for successful remote sensing applications such as quick disaster recovery, detecting and locating humans and flames (fire fronts) or locating smouldering trees.

This study evolved from my research and development work back in 2012 when I was working as a remote sensing specialist and photogrammetrist in a local engineering company in Adelaide, Australia. The organization was incorporating a particular NIR camera in an UAV framework that was created in-house created, and which was additionally the platform for a consumer-grade DSLR camera. The point of this incorporation was to simultaneously collect NIR and natural colour images to extract NDVI data from vineyards. One of the difficulties after data collection was to precisely align and co-register pixels between the two sensor images, and another issue was carrying two separate cameras on a lightweight UAV framework. These issues inevitably drove me to examine the likelihood of altering the DSLR camera by extending its spectral range to collect the data required for NDVI calculation. The modified camera collected red, green and NIR light and produced sensible NDVI information. To confirm its precision, Airborne Research Australia (ARA) recommended I setup the camera on one of their manned light aircraft that also had a multi spectral sensor, to verify the modified camera. At that time, I met with Prof. Jörg Hacker, the Chief Scientist of ARA (which at that time was part of the School of the Environment at Flinders University) who encouraged and inspired me to apply for a research higher degree at Flinders University on part-time basis while I was working for my employer. After a year I left the company and became a full-time student. At that time, high winter rainfall over a number of years in South Australia had led to much vegetation growth. This was trailed by a dry session during which various bushfires destroyed roughly 5.58 million hectares of land (CFS 2015). Smoke from these bushfires postponed aerial firefighting operations because of the low visibility conditions. This issue highlighted the importance of my underlying research objectives and goals which are discussed in the following section.

1.3. Research aims, objectives and question

1.3.1. Aim

The aim of this study is to produce a new method for seeing through gaseous smoke using a consumer-grade digital camera without compromising spatial resolution or image colour.

1.3.2. Objectives

The following specific objectives will be pursued to achieve the aim above:

1. To study and verify the sensitivity of a DSLR camera sensor in the near infrared region of the spectrum (700 nm – 1100 nm).
2. To develop and examine a custom optical filter for reducing light scattering effects.
3. To develop an image visibility enhancement algorithm for the images obtained using the custom-designed filter on a DSLR camera.

1.3.3. Research Questions

To address this research aim and to achieve the research objectives, the following research questions emerged:

1. Can images acquired by DSLR cameras, after modifications to full spectra, penetrate smoke? This question emanates from the first objective.
2. Is it feasible to design an optical filter to minimize the scattering effect on DSLR camera images without compromising true-colour? This question emanates from the second objective.
3. Can an image visibility enhancement algorithm be developed to improve smoke penetration from a modified camera setup? This question emanates from the third objective of this research.

1.4. Thesis structure

This research consists of six chapters which are described as below.

Chapter 1, *Introduction*: explores the background and states the problem, objectives, aims and research questions.

Chapter 2, *State of knowledge*: reviews previous studies and highlights gaps in knowledge that this study attempts to fill.

Chapter 3, *Methods*: discusses methods utilized to achieve the aim and objectives of this research, including the research framework, hardware and software development, data collection and analysis.

Chapter 4, *Hypothesis validation*: confirms the main hypothesis of this research which emanates from the first and second research questions and examines them using historical multispectral, thermal and optical imagery collected over a bushfire smoke.

Chapter 5, *Optical filter design*: discusses the key factors in designing a custom-filter and the tests conducted to confirm its spectral response using calibrated materials and spectrometry.

Chapter 6, *Measuring the camera and filter responses*: verifies the spectral response of the custom-designed optical filter and modified camera at different wavelengths using a FieldSpec4® Hi-Res spectrometer.

Chapter 7, *Algorithm development*: explains the image processing workflow and develops an algorithm for minimizing smoke effect on captured images using the custom-designed filter and modified DSLR camera.

Chapter 8, *Conclusions and Recommendations*: revisits the research problem, aim, objectives and questions; and discusses how each of these is addressed. It also summarizes the research findings and discusses future directions.

And appendices include two published papers with custom-designed filter spectral response graphs using reference materials.

1.5. Chapter Summary

This chapter discussed the foundations of the research and introduced the research problem, aim, objectives and questions. The research problem highlighted that images collected by a digital consumer-grade camera in an environment covered by haze or bushfire smoke are less than optimal for identifying fine objects and seeing through smoke due to the greatly degraded image quality and visibility. It also discussed that existing thermal, multispectral or similar sensors with longer wavelengths can penetrate gaseous smoke but because of their limitations as per listed in section 1.3, are not ideal in situations where natural image colour and spatial resolution is critical. The next chapter reviews the state of knowledge based on the research objectives.

Chapter 2

State of Knowledge

2. State of Knowledge

2.1. Introduction

Over the past decade research projects have been conducted in the field of enhancing visibility of the remotely sensed digital images from non-clear environments caused by haze, fog or gaseous particles. Digital camera technology has also dramatically advanced in recent years with the use of higher quality sensors with millions of small pixel arrays, hence spatial image resolution has been significantly increased.

This chapter provides a comprehensive review of the state of knowledge on bushfire and smoke formation and detection, light scattering by smoke particles, and improvements in image visibility in atmospheric conditions where there are many gaseous molecular particles. The first section provides background on, and an historical overview of bushfire formation, its anatomy and smoke detection. The second section discusses the theory of EMR and EMS as well as examining the pathways of EMR through atmosphere and EMR interactions with molecular particles. In particular, it focuses on the light scattering effect. The next section reviews the particle size and characterization of smoke particles. This is followed by a review of the effects of smoke particulates in TIR and SWIR imagery. Although there is no previous research directly related to the specific research area of this thesis to the author’s knowledge, two next two sections of this chapter discuss related studies in the context of the removal of haze from single and multiple images collected by a single or multiple sensors respectively. The chapter concludes with a section focusing on the spectral sensitivity of digital camera sensors and their application in remote sensing.

2.2. Wildland Fire Formation and Development

Bushfires can start as a result of applying heat to a fuel source by natural phenomena such as lightening or by humans setting fires. After applying heat, for instance, to a piece of wood, there are three phases in the formation of a fire: pre-ignition, ignition and combustion. In the pre-ignition phase, when heat is applied to a wood surface any water molecules stored in the fuel will absorb the energy and increase the temperature. Water molecules at the surface of the fuel are evaporated as the heat level rises and the surface temperature is maintained around 100 °C. Drier surfaces will get hotter than more moist ones because the temperature is no longer maintained by water evaporation and, as a result, terpenes, oils and resins in the wood begin to vaporize and create a haze of ignitable gases over the fuel. As the fuel temperature gets to around 130 – 190 °C wood begins to collapse chemically and at over 260 °C the cellulose in the wood creates a charred surface and a grey smoke emanates. At 280 – 500 °C, flammable gases from the lignin in the wood are released. In the ignition phase, the flammable gases are ignited as a result of piloted or unpiloted flames as the temperatures rise. For piloted ignition, the temperature of flammable gases should increase to around 320 – 500 C°, but for unpiloted ignition the temperature must be around 600 C° (Gann & Friedman 2013, p.134).

The process of chemical fuel decomposition and release of a gaseous cloud in absence of oxygen is known as pyrolysis (McGrattan et al. 2009). This process is maintained by the radiated heat from combustion and cloud of gases build up over the fuel which will eventually burn and then ignite any unburnt fuels. During flaming combustion, the gases released by pyrolysis start to burn the wood surface. The flame is comprised of an inner core of unburnt gases enclosed by a thin flaming envelope where enough oxygen combines with the gases and leads to combustion. As the fire gets hotter, greater amounts of burnable gas develop, and flame become longer as they move to incorporate more oxygen to maintain the burn (Thomas & McAlpine 2010, p.28). Therefore, fuel, heat and oxygen are the three essential elements for a flame to develop. Most of the carbon is released from a fire is in the form of carbon dioxide; the rest comprises a complex combination of gases and soot mixed with water vapor. Soot is mainly formed by fragments of carbon and tar that clump around small components of unburnt fuel to create lumps that are less easily burnt. They absorb heat from the surrounding area and form the orange to red colours in the center of a fire. When unburnt soot molecules above the flame cool down, black coloured smoke is formed above the flame. Char and ash keep building up in an upper layer of the fuel surface as it burns and although pyrolysis is yet continuing, it is normally not adequate to sustain the flames and therefore fire combustion stops, and the flames die down. Yet, when the oxygen interacts with the surface of that type of fuel, the released heat begins burning in the form of a slow and flameless combustion process known as smouldering combustion. Inside the fuel, carbon monoxide will be produced instead of carbon dioxide due to the lack of oxygen. When the flame goes out, the glowing combustion keeps burning the fuel without any flame and the energy discharged by the smouldering combustion transfers the heat to any nearby unburnt fuel and produces grey smoke. This develops large volume of smoke and carbon (Drysdale 2011).

The process of transferring the heat contributes to spreading the flame from a single location to other regions with unburned fuel, thermally deteriorates the unburnt fuels, and creates a flammable mix in front of the flame. Ignition of this flammable mixture spreads the flame to a larger region (Haseli 2012). Heat transfer happens in three forms; radiation, convection and conduction (Morvan, Méradji & Accary 2008). Radiated heat from burning fuel preheats the fuel ahead of the flame. As the fire spreads, radiation moves in all directions. Convection is the process of hot air movement, e.g., as blown by wind, which is vital in heating the crowns or plants on steep ground. Conduction accelerates the heat transfer process if there is any close contact between the fuel particles. If there is enough heat to evaporate the fuel moisture pyrolysis can happen, hence the amount of moisture stored within a solid fuel can affect the fire behaviour.

Fire will generally spread slowly against the wind direction (known as back-fire), very rapidly with the wind direction (head fire); and at intermediate rates elsewhere, i.e. at the flanks. These differences in spread rates create an elliptical shaped fire (Thomas &

McAlpine 2010, p.37). Nonetheless, the speed of spread of the head fire, and it’s intensity and the severity are the key characteristics of a burning fire. Fires can also be categorized into ground fires, crown fires and surface area fires (Paysen 2000). Ground fires are the slow fires that happen under the soil surface, roots and ground fuels above the soil. These fires penetrate the underlying deep minerals and are sensitive to soil moisture levels. They can burn for years and are one of the most challenging types of fire to control. When ground fuels are ignited, they burn gradually downwards and to the sides from the glowing combustion which produces carbon monoxide. This process may happen in an atmosphere with less than 20% oxygen levels of an ordinary atmosphere, as a result the fires can burn underground. However, to generate carbon dioxide at least 16% oxygen is required (Rein 2016).

Most of wildland fires start and end up as surface area fires that burn recently fallen leaves and branches, and lichens, shrubs, grasses and bushes. This potentially creates a big fire (Porterie et al. 2007). These fires are accountable for almost all large bushfires burning close to the ground but not those in tree canopies, which as known as crown fires. Crown fires take place when fire reaches the canopy of trees and they ignite. They can end up as huge fires that progress through the treetops with massive fire walls. Because of the leaves and small dead wood that is normally associated with these fires, they usually take place in woodlands and forests with combustible fuels; for example, Boreal and Cool Temperate coniferous forests and Eucalypt woodlands in Australia. Typically, canopies are designed to withstand ignition due to their large amount of moisture or fire-resistant.

Most massive fires spread out through surface fuels so comprehensive physical descriptions of surface fuel elements is required for managing these fires (Keane 2015). Surface fuel particles can be alive or dead and are typically different throughout the surface fuel. For example, herbaceous particles have different properties than fallen wood. There are a set of surface area fuel components that are common contributors to many fires and that are present in the majority of surface fuel beds of the world, particularly forests with fallen dead wood, shrubs, an herbaceous layer and litter. Dead woody fuels present in the surface fuel layers of all forest and woodland environments consist of twigs, branches and boles of fallen woody plants. They are primarily cellulose and lignin (Lutes et al. 2009). Freshly fallen fuels are known as litter and they varying considerably since they may include a broad range of fallen vegetation, e.g., conifer cones, bud scales and grass blades. Since the litter components are normally thin, they can dry out rapidly and easily ignite. The plant elements in the litter also usually have a heterogeneous spatial distribution and highly dissimilar fuel properties (Duff et al. 2017).

The surface fuel layer may contain shrubs which comprises woody and foliage components Shrubby fuels therefore vary in terms of dimension, form, and fuel particle distribution. Bushlands of Australia, as one of the world's major shrub environments, have a background of regular burning and many of the shrub types have developed unique adaptations for withstanding fire (Cruz et al. 2018).

In Australia, herbaceous plants are extensive and comprise a range of unique grass fuel categories in both seasonal and annual grasslands. Many grassland vegetation communities also have either tall (2 – 5 m high) shrubs or low (< 10 m high) trees, for example, species of *Acacia, Allocasuarina* or *Eucalyptus* (Mott and Groves 1994, pp. 369–392). In terms of the herbaceous components, rushes, grasses and sedges have long and straight leaves with high surface to volume ratios which develop strongly ignitable fuel surfaces (Fateh et al. 2014). Meanwhile, ferns and forbs may have large leaves and a structural skin that can protect them against sparking. Most herbaceous plants ultimately die over time and the quantity of biomass created by them are typically controlled by climate and morphologically harmonized for ignition and fast spreading wildland fires (Heaton et al. 2008).

2.3. Smoke Formation, Detection Techniques and Platforms

Bushfire smoke is comprised of a combination of gases and particulates with more than 100 detected substances including a range of aldehydes, phenolics and polynuclear aromatic hydrocarbons (Radojevic 2003). The main substances are carbon dioxide and carbon monoxide (Delichatsios 2005; Lyon & Quintere 2007; McAllister 2013). Most of these substances are produced by glowing and low intensity flaming fires and vary depending on the fuel composition, combustion type and fuel moisture (Werf et al. 2006). Smoke can degrade air quality, impair exposure, and impact visibility or the effective range at which firefighters could see through smoke (Torero & Simeoni 2010). Smoke particles can also affect wind and weather patterns. In the context of this research they also reduce the amount of the EMR reaching the ground, which can also affect weather. Small particles <10 mm diameter comprise less than 10% of the total weight of smoke particles but are the most crucial for human health (Karthikeyan et al. 2006). Fine particulate matter (<2.5 mm in diameter and known as PM2.5) are drawn deep into the lungs (Sastry 2002). These are the particles which travel the furthest and remain in the air for weeks. Fires of great intensity, i.e., with longer flames, produce proportionately bigger smoke particles than smouldering fires. Particle size also has the many effects on visibility in the environment.

Smoke plumes can cover large areas, crossing the borders countries and reaching over oceans from land sources. They impact large-scale weather condition patterns by affecting the quantity of solar energy reaching the ground surface by simply scattering and absorbing of the EMR. Lyons et al. (1998) showed that some smoke plumes were larger than 3,300,000 km^2, slightly less than half the area of the Australia. Figure 2.1 shows how smoke plumes cover very large areas. Although much of the plume in tie figure would be nearly invisible from the ground, the particles in it will still be interacting with ground weather patterns, visibility and atmospheric chemicals. Such plumes can move a thousand kilometers in a couple of days and persist for weeks (Fromm 2000; Voiland 2014).

Image has been removed due to copyright restriction.

Figure 2.1. Active wildfire captured by MODIS on September 2015 in eastern Sumatra, Indonesia. The smoke plume covers a relatively large area and has emanated in from the active fire fronts outlined by red (Voiland 2014).

Over the past decade a number of techniques have been developed to detect, locate and monitor smoke emitted from wildfires. These techniques are either based on satellite remote sensing or ground based detection methods. Smoke detection has prospective applications in air quality analysis, and fire detection and behaviour analysis (San-Miguel-Ayanz 2005), e.g., detection of small and smouldering fires (Wang et al. 2007) and reduction of the process of fire spread (Liu 2013). Remote sensing-based large-scale smoke detection has been a common method since satellite remote sensing has supplied worldwide observations of the Earth's surface. For example, the Moderate Resolution Imaging Spectroradiometer (MODIS) with 36 spectral channels captures data in the visible to far infrared parts of the EMS and can acquire abundant spectral information compared to many other space-based sensors, e.g., the Advanced Very High-Resolution Radiometer (AVHRR). However, smoke has no characteristic spectral reflectance signature because of the variability of the chemical composition. This combined with a large overlap of the spectral signal between smoke and other cover types such as cloud, water and plants, makes the accurate smoke detection process difficult (Li 2001). Among the numerous methods for space-based smoke detection, one of the most common methods is to merge three bands in satellite data to form a colour composition image (Chrysoulakis & Opie 2004) for visual smoke detection. These colour-based techniques only provide general details about smoke but fail when applied in the automated smoke detection techniques. There are other techniques for automatic and accurate smoke detection methods which are usually known as multi-threshold methods. These techniques are based on distinguishing the physical properties of smoke and other particles and use a set of thresholds to automatically examine all image pixels to filter non-smoke pixels progressively (Zhao & Ackerman 2010). They used MODIS images to analyses the spectral and spatial threshold along with some similarity structure filtering. Chrysoulakis et al. (2007) proposed a multi-temporal change detection method using two AVHRR images (one is acquired during the fire and the other without smoke e collected before fire) over the same area. The irregularities in NDVI and infrared radiances were used to recognize the plume locations.

Most of satellite-based methods for successful smoke detection can be influenced by the poor spatial resolution (Gong et al. 2006) and typically have infrequent revisit periods. Furthermore, it may take several hours to receive and use the data from satellites. Climate and specifically cloud coverage are other factors that compromise the collection of visually useful images from most satellites.

Airborne platforms have been suggested to fill the gaps between ground-based and satellite-based image acquisition. These platforms can be classified by aircraft type, sensor type, and manned and unmanned piloting. Manned aircraft platforms can carry large sensors including LIDAR, SWIR, multispectral, optical or thermal cameras with no payload restrictions as opposed to unmanned aerial vehicles (UAVs). LIDAR is an encouraging instrument for forest-fire monitoring and smoke detection, due to its high spatial resolution and sensitivity. While it typically has highly reliable smoke detection outcomes in locating small smoke plumes throughout the day and night (Utkin et al. 2003), the considerable effort required in implementing and mobilizing LIDAR sensors coupled with their high cost have made this option less popular than others. The type of imaging sensor to meet the fire intelligence requirements is very important. For example, it is essential that fire intelligence data from these sensors be supplied at the required spatial resolution with no considerable time lag. Aircraft with high-altitude flying capability can supply an extensive overall image of large regions but similar to satellite sensors are subject to cloud obscuration for collecting visible or IR images (Kaufman, Kleidman & King 1998). Moderate and low-altitude flying aircraft, such as small UAVs and suppression aircraft, are used to overcome this limitation.

UAVs are considered as a lightweight flying equipment similar but different to manned aircraft since they do not require a pilot on-board. The majority of them can be launched and operated remotely using a ground control station and a telemetry communication link (Allison et al. 2016). Based upon the take-off type, UAVs are classified as fixed-wing or VTOL (Vertical Take-off and Landing) (Watts, Ambrosia & Hinkley 2012). Originally UAVs were utilized for military applications such as reconnaissance and surveillance. Overtime, they have become widely used in civil remote sensing applications in agriculture, utility inspection, mapping, and natural resources and environmental applications (Colomina & Molina 2014). Advances in sensor systems and image processing have increased applications of the UAVs in many other sectors.

Most UAVs are equipped with optical sensors to capture the visible red, green and blue region of the EMS as a standard imaging payload. However, other sensors such as IR, TIR, SWIR and LIDAR sensors can be used as additional payloads for remote sensing applications (Zahawi et al. 2015). Lightweight remote sensing sensors on-board UAVs can provide high spatial, temporal and spectral resolution imagery (Yuan, Zhang, Liu 2015). In Australia firefighters have successfully trailed small quadcopters to collect infrared imagery from an overnight bushfire (Werner 2015). Zajkowski et al. (2016) used small UAVs equipped with thermal cameras and alive video feed above a prescribed burn area to evaluate the feasibility of using these new technologies in a complex operational environment.

UAVs can fly at low altitudes to supply extremely high spatial resolution images (Yuan, Zhang & Liu 2015) which can be used in applications such as cadastral work, urban planning, vegetation species categorisation and yield estimate (Colomina & Molina 2014; Gaitani et al. 2017). The expense of information collection and post-processing using UAVs is lower than that of equivalent approaches that supply the same accuracy (Puliti et al. 2015). Another advantage of using UAV platforms is the low energy consumption rate of electric and gas fuels (Banu et al. 2016). In addition, their safe operation does not risk lives since no human is directly engaged during the operation. Nonetheless, the feasibility of using UAVs in wildfire and forestry applications needs further evaluation to better understand the risks and benefits (Banu et al. 2016).

Due to the short flight time of the UAVs they must be launched and used nearby the fire area. The flight time of the aircraft above a fire is a key concern and a major challenge for most small UAV platforms (Ollero 2011). NASA and the US Forest Service have performed several small UAV tests to address the flight time issue in particular (Hinkley & Zajkowski 2011). In addition to flight time, the aerospace regulation and certifications to allow UAVs to fly in controlled airspace and beyond line of sight are still major issues in deploying these platforms effectively. Sensor stabilization, flying altitude and image motion (Chabok 2013), coordination, mission planning and image georeferencing are typically very challenging for these types of operations because the flight path design is limited by operational requirements and is not suitable for conventional airborne imaging, georeferencing and mapping missions.

Ground-based, especially video-based, systems are popular methods for wildfire monitoring and smoke detection and have been proven to be an effective method in the past decade (Utkin et al. 2003; Ko, Park & Nam 2013; Jakovcevic, Stipanicev & Krstinic 2013; Çetin et al. 2013). One of the significant benefits of video-based detection is that it has the ability to cover larger regions which is useful for long-range smoke detection in bushlands or forests where the origin of smoke origin may be few kilometers from the camera location; for example, a zoom video camera can cover up to 100 km^2 from a lookout tower (Çetin et al. 2013). Monitoring systems based upon CCD sensors are frequently utilized in smoke detection and are generally installed on the lookout towers which are taller than the surrounding trees and structures. While other sensors, such as IR and thermal cameras (Arrue, Ollero & De Dios 2000; Gade & Moeslund 2014), may be more capable in detecting smoke and flames and provide more reliable and useful data (Martinez-de et al. 2008), video-based monitoring systems are still an appealing method due to their low cost, ease of use and low maintenance requirements (Berie & Burud 2018).

The sizes of particles produced by wildfire smoke and its characteristics play an important role in success of remote sensing for fire and smoke detection and monitoring techniques. This aspect of the research is discussed in the next section.

2.4. Particle Size and Characterization

Wildfire smoke consists of microscopic particles known as aerosols which have the potential to impact both the environment and human health (Maynard & Kuempl 2005; Maynard et al. 2006). Figure 2.2 shows how the dimensions of particles of interest in aerosol behaviour vary from molecular arrays of 0.001 µm to dust particles as large as 100 µm (Kouimtzis & Samara 1998, p.3). Aerosols can be categorized according to their physical shape, size and the processes by which they are produced. Dust is a solid particle that develops by mechanical fragmentation of a source object, for instance, in industry by crushing or milling, or in the natural environment by erosion processes. Physicochemical processes such as combustion produces heat and water vapour. Burning as an oxidation process produces smoke. Fog and haze are fluid aerosols generated by the fragmentation of liquid or vapour combustion; while smog, a mixture of smoke and fog, includes solid and fluid particles created as a result of photochemical reactions and ‘vog’ is a mixture of volcanic ejecta and fog.

Image has been removed due to copyright restriction.

Figure 2.2 Range of aerosol particle size starting from 0.001 µm for molecular particles to large particles up to 1000 µm. Smoke particle size ranges from 0.01 µm to 100 µm (Kouimtzis & Samara 1998).

As soon as aerosols are in the atmosphere, their size, number and chemical arrangements can be changed through several mechanisms before they are eventually removed by natural processes. There are normally three groups of particles in terms of particle size d measurement; nucleation, accumulation and coarse form (Wilson and Suh 1997). Nucleation consists of particles < 0.2 µm diameter which are formed by the condensation of hot vapour or by gas to particle transformation. Accumulation form aerosol particle diameters ranges from 0.2 – 2 µm and grow from the nucleation mode by vapour condensation. They typically represent much of the surface area of aerosols in the atmosphere and a substantial part of their volume. Coarse form particles of > 2 µm diameter are primarily created by physical attrition; dust from rock and soil erosion, industrial dusts and water spray are the main components of coarse form particles.

Chemical composition has been identified as a function of particle size. Hao et al. (2013) and Wu et al. (2013) consider the differences between the fine (< 2.5 µm) and coarse (2.5 – 15 µm) forms. The primary elements of the fine portion of atmospheric aerosols are sulphates, nitrates, lead, carbonaceous products and thick organic matter. The coarse particulate portion comprises mainly crustal materials (Corbitt 1989, p.115). Aside from the contrast between the size and chemistry of aerosols, organic and anthropogenic sources provide a dissimilarity. Many causes leading to aerosol production are natural, e.g., volcanic eruptions, while others are anthropogenic, e.g., industrial discharges. However, there are some origins of aerosols in which the contrast between natural and anthropogenic is more difficult to make, e.g., dust emissions from soil and burning biomass.

In particle characterization, almost all the methods that have been designed to deal with the complexities caused by the polydispersity of particle systems, i.e., particles with a large variation in size (Caho et al. 2017). In the case where all of the components of the system have similar attributes, there is barely be any requirement for such complex characterization techniques. An overall particle population where all the aerosol particles possess the similar dimension are known as monodispersed particles. The actual particle dimension, in both monodispersed and polydispersed aerosols, includes a particle size distribution across a specific range. Numerous techniques that have been designed and implemented in particle characterization, particularly where particles sizes range from nanometers to millimeters. The dimension, quantity (Wang et al. 2011) and surface area concentration (Asbach et al. 2009) are the key criteria in defining aerosol particles. Particle size distribution is an important parameter for the assessment of particle density in atmosphere (Manigrasso et al. 2013) The method of quantitatively characterizing particle size distribution is to create a frequency histogram of the mass of particles in consecutive size intervals. In a constant distribution, i.e., monodispersed, the histograms create a smooth constant curve (John 2011, pp. 41–54).

In the past few years various techniques that include sun photometers (Queface et al. 2011), satellite data (Tesfaye et al. 2011) and ground-based Raman Lidar systems (Giannakaki et al. 2015) have been used as tools to measure particles (Wang et al. 2018). Specifically, they have been implemented to precisely measure the aerosol particle size, and their geometrical and optical characteristics. In fact, satellite remote sensing continually supplies accurate worldwide measurements of Aerosol Optical Thickness (AOT) (Kokhanovsky et al. 2010; Holzer-Popp et al. 2013).

Raman Lidar is an active remote-sensing tool which uses light from UV lasers light to measure the height and time-related properties of aerosols, the water vapour mixing proportion, temperatures and cloud optical properties. It operates by passing short pulses of UV light through the atmosphere. A small portion of the UV light energy is backscattered to the lidar transceiver in which it is captured and compiled as a time-related signal. By measuring the delay between the outbound pulse and the backscattered signal, it derives the distance to the scattering volume. Raman (1928) showed that light is inelastically scattered by atmospheric N_2, O_2 and H_2O particles. A Raman Lidar utilizes an array of narrow-band recognition channels particularly tuned to pick up the Raman backscatter from these particles. The raw signals coming from these detection channels are incorporated and refined to measure the aerosol backscatter coefficient, water vapour mixing percentage, the temperature level and the depolarization percentage. Giannakaki et al. (2016), conducted an extensive study to measure smoke aerosol particles from fire using a combination of Raman Lidar and satellite-based observations to identify the origin of raised aerosol layers and precisely measure the lidar and the depolarization ratios for biomass burning and mixtures of aerosols. They noticed a large range of lidar and depolarization ratios and microphysical properties for biomass burning aerosols that imply distinctions in the chemical structure of the various fuels that were burning. Their study showed that aerosol diameters from industrial pollution ranges from 0.07 – 0.16 µm, those from biomass burning are in the 0.11 – 0.28 µm range, while mixed aerosols ranges from 0.09 – 0.19 µm. Although UV absorption or satellite-based methods provides data on a variety of aerosol properties

(Torres et al. 2007; Dubovik et al. 2011), variable background reflectance above land surface areas makes the data collection process challenging, particularly at low optical densities.

NASA and PHOTONS (PHOtométrie pour le Traitement Opérationnel de Normalisation Satellitaire) have collaboratively established a global network of ground-based remote sensing systems, known as AERONET (AErosol RObotic NETwork), to supply regular and easily available public domain data on aerosol optical, radiative and microphysical properties for aerosol analysis and characterization. AERONET delivers more effective aerosol measurements compared to other systems since the observations are influenced less by surface area reflectance factors and are accumulated from semsor operating at different angles (Holben et al. 1998). These observations are often used for satellite data validation (Holzer-Popp et al. 2013). AERONET aerosol characterizations have been computed using the average values from a series of stations. A single record from one of the AERONET stations, for instance near a boreal forest, most likely will include smoke observations of trees of various ages and source. Therefore, research has been conducted to identify the origin and age for AERONET smoke observations, concentrating on individual burning activities using atmospheric transport modelling and satellite data (O'Neill et al. 2002; Eck et al. 2009; Dahlkötter et al. 2013). Sayer et al. (2014) classified collections of AERONET stations from biomass burning areas into near and remote origin to examine the ageing impacts on optical and microphysical smoke properties. Nikonovas, North & Doerr (2015) conducted research to measure the smoke aerosol properties using the AERONET networks near northern temperate and boreal forests for the period 2002–2013. They compared 629 fire attributions and noticed significant variations in the size distribution and optical particle properties between smoke plume age and various land cover types. They observed a 0.143 μm median radius for smoke plumes from burning cropland, 0.157 μm for grassland fires, 0.193 μm for Eurasian mixed forests, 0.185 μm for smoke plumes from shrubland with sparse tree cover, and 0.184 μm for woody savannas. The difference in size distributions relates to irregularities in plume distribution between the land cover types. They also noticed substantial distinctions between daytime and nighttime emissions, with former having larger particle sizes; as well as showing that smoke that was older than four days had a median radius of 0.02 μm compared to larger radius for fresh smoke plumes.

Light scattering is the most efficient method for investigating the properties of particulate matter and particularly for the measurement of particulate size (Jones 1999). The relationships between the size and optical properties of aerosols and the scatter the incident light, which is known as extinction of EMR, is discussed in the next section.

2.5. Pathways of EMR through Atmosphere and Light Scattering

When Isaac Newton was exploring a single stream of sunlight ray in 1666, he placed a glass prism in the light direction and noticed that it decomposed into a rainbow of colours: red, orange, yellow, green, blue, indigo and violet. He showed that every colour refracted at different angles which can be calculated and measured by a prism. He also noticed that objects appeared in the same colour as the illuminated light colour and that the reflection or refraction does not change the colour of illuminated light. Thus, he concluded that colour is not property of objects but is a property of light which is reflected from the objects. He also considered that light is a radiation of particles which are nowadays known as photons. The discovery of the colour spectrum by Newton was the beginning of the science of spectroscopy (Lenoble, Remer and Tanre 2013, p.138). In 1800, William Herschel used thermometers to measure the temperatures of the colour spectrum that had been discovered by Newton, he noticed temperatures increased from visible violet to visible red and that it increased further in regions beyond visible red, thus he discovered infrared light. A year later in 1801, when Johann Ritter was experimenting with a photographic plaque made of silver chloride, he noticed that it reacted intensively beyond visible violet, and hence discovered the ultraviolet range of EMS. In 1801, Thomas Young showed that light may also be considered as traveling waves. He diffracted sunlight through a small slit and then projected the light rays that emanated from the slit onto screen with two small slits. Light passing through these slits was then re-projected onto another screen, which was close to the slits, and formed two overlapping patches on the screen. When Young reduced the size of slits and placed them side by side, the light projected onto the screen formed a distinct band of colours separated by dark regions. To describe these bands, he coined the term ‘interference fringes’ term and measured the wavelengths (Kipnis 1991, pp. 122-124). Maxwell, in 1873, explained the electromagnetic nature of radiation and showed that electromagnetic waves consist of electric and magnetic fields that move in space until absorbed by matter. In 1885, Heinrich Hertz verified Maxwell's electromagnetic theory and created electromagnetic waves in his laboratory. He used two small brass conductors, placed a few millimeters apart and connected to induction coils, to make an electrical oscillator. He passed a high-tension current through this circuit and noticed that the spark jumped as a result of accumulating the electrical charges. He noted that another spark jumped simultaneously in an antenna in the shape of a loop which was located few meters away. This experiment confirmed Maxwell’s hypothesis and demonstrated that electromagnetic waves can transmit energy in space without the aid of a physical conductor. These Hertz waves were later renamed radio waves (Norton 2000, p. 83).

In 1895, Wilhelm Conrad Röntgen noticed that when an electric current pass through a bulb in which the air pressure is low, the bulb produces rays which can penetrate objects including the human body. As the nature of these rays was unknown at that time, he named them x-rays. They were quickly adopted in radiography. In 1912, Max Von Laue experimentally diffracted x-rays using a crystal and showed that they had extremely short wavelengths beyond the ultraviolet region of spectrum. Later Henri Becquerel in 1896, Marie Curie in 1898 and Paul Villard and Ernest Rutherford in 1900 discovered there were even shorter wavelengths in the EMS – gamma rays. During the Second World War, with identification of microwave radiation, long range radio detection and ranging (radar) was developed to detect moving objects at longer distances by measuring reflected radio waves from their surface. Thus, by this time all the possible frequencies and wavelengths of electromagnetic radiation had been discovered. Gamma-rays with extremely short wavelengths in one end of spectrum contain very high frequency and have high energy levels, whereas radio waves in the other end, have very long wavelengths, lower frequency and very low energy levels. (Figure 2.3).

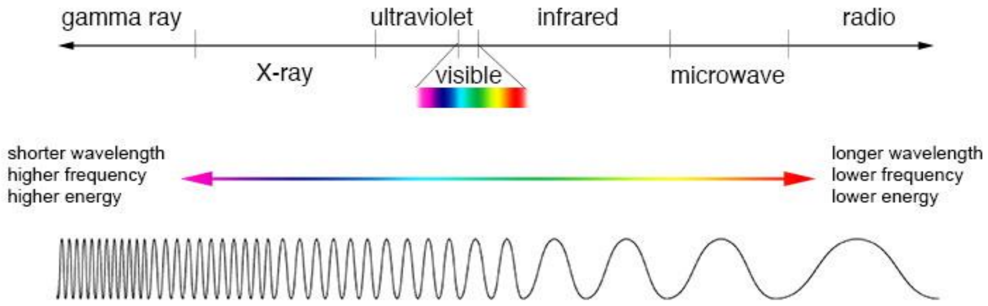

Figure 2.3. The full range of the electromagnetic spectrum and the correlations between wavelengths, frequency and energy (Courtesy of NASA GSFC Astronomer's Toolbox).

Although there are many forms of EMR across the spectrum from gamma-rays to the radio waves, only visible light as a small portion of the spectrum can be sensed by our eyes. Fortunately, the development of ultra-sensitive detectors allows us to capture invisible radiation and to translate it and visualize its affects. For example, a digital television remote controller uses a light emitting diode which is invisible to the human eyes but can be seen by holding it in front of a digital camera, this means that a digital camera is sensitive to infrared light. The Sun, as the source of EMR, emits radiation across most of the EMS, though gamma rays which contain super high energy photons that result from nuclear fusion are converted to a lower energy photon before reaching the Sun's surface and therefore are not emitted into space. However, x-ray, ultraviolet, visible, infrared and radio waves are emitted from the Sun. The distribution of the EMR energy emitted by the sun peaks in the visible light range (Figure 2.4).

Image has been removed due to copyright restriction.

Figure 2.4. Absolute solar spectral irradiance shows distribution of the EMR energy versus its wavelength. It can be seen that the maximum emitted energy from the sun is in the range of visible spectrum at λ~450 nm (Thuillier et al. 1998).

When EMR travels through the space, only a few forms of EMR can pass through the atmosphere. The major components of the Earth's atmosphere create selective transmission of various forms of EMR. For example, it is mostly closed to incoming UV radiation, long wavelength radio waves and long wavelength infrared. The primary components that effectively absorb electromagnetic energy are water vapour (H_2O), carbon dioxide (CO_2) and ozone (O_3) (Joseph 2015, p.45). Though different aerosols absorb EMR at different wavelengths. For example, water vapour strongly absorbs EMR between 5.5 – 7 µm and at > 27 µm. Carbon dioxide effectively absorbs EMR in the mid and far infrared region between 13 – 17.5 µm and ozone absorbs strongly the UV portion of the spectrum (Figure 2.5).

Image has been removed due to copyright restriction.

Figure 2.5. Various forms of EMR that are transmitted or absorbed as a result of interaction with atmosphere, note that visible light is less absorbed and more transmitted to the ground surface (Joseph 2015, p.45).

Areas of EMS with minimal or no absorption of EMR are known as atmospheric windows. As discussed above (*cf.* Figure 2.4), most of emitted energy from the Sun is in visible and infrared regions with a small amount of UV. This is known as incoming solar radiation or insolation. Insolation can be partially scattered, absorbed or reflected. Absorption happens when incoming solar radiation encounters a gas or particular object but not released directly by that object. Scattering is a process in which incoming solar radiation is redirected by particulate or atmospheric gases and its distribution is changed. Reflection occurs when solar radiation interacts with the ground surface and is redirected back through the atmosphere (Figure 2.6).

The interaction of EMR with the atmosphere may prevent it from reaching the ground due to the processes of scattering or absorption. The absorbed illumination energy which emerges as the excitation energy of particles will be dissipated primarily by its transformation into heat or will lost through radiative decay. Because many substances exhibit high absorption in the infrared and ultraviolet regions, which considerably minimizes scattering magnitude, most light scattering measurements are carried out utilizing visible illumination. Scattering is only detected when a substance is heterogeneous, either as a result of regional density variations in the pure component or because of the optical heterogeneity for spread particles in a medium (Xu & Scarlett 2002, p.57). The extent to which absorption and scattering take place depends upon the atmospheric conditions, the length of the path through the atmosphere and is wavelength dependent. These effects happen due to the interaction of the EMR with particles created by air pollution, dust or water molecules suspended in the atmosphere in fog or in clouds. Each of these have different effects on the radiation that passes through the atmosphere and affects how much of the radiation reaches the earth surface.

Image has been removed due to copyright restriction.

Figure 2.6. EMR can be scattered, absorbed, transmitted or emitted when encountering clouds, aerosols, gas molecules and ground objects (USGS 2017).

Figure 2.7 illustrates a basic scheme for light scattering geometry. In this figure, which for illustration purposes is simplified, the polarization direction is assumed to be either parallel to a hypothetical plane, called horizontally polarized (E_h), or perpendicular to the plane in the Z direction, called vertically polarized (E_v). While the incident light is passing through the scattering media it will be transmitted, unless the particles are highly absorbing or the particle density is so high, in which case multiple scattering will occur. If multiple scattering does occur, the scattered light from one particle acts as the incident light of another particle. Encountered incident light by the particles will be scattered unevenly in all directions.

Image has been removed due to copyright restriction.

Figure 2.7. Light scattering geometry in a laboratory environment (Xu & Scarlett 2002)

In Figure 2.7, K_o is the wave vector of the incident light traveling along the X axis in vacuum. Its magnitude ($K_o = 2\pi/\lambda$) is the wavenumber of the incident light for each given wavelength (λ) and $\lambda = \lambda_0/n_0$ (where n_0 is the reflective index of the medium). For polarized light this vector is oriented in a specific direction but for non-polarized light it is oriented randomly. Both the intensity of scattering and intensity variations are a function of both the incident light and the scattering direction. Typically, the scattering direction is defined as the direction that is at an angle θ from the X axis, which is known as the scattering angle, and an angle φ from the Z axis, which is known as the azimuthal angle. The propagation directions of the incident scattered and transmitted light forms a plane which is known as the scattering plane. In figure 2.7, the azimuthal angle is presumed to be 90°, I_o is intensity and K_s is the wave vector of scattered light, respectively. The scattering vector or so-called momentum-transfer vector is defined as the momentum transfer between a particle and the incident light ($K = |K_s - K_o|$) which is defined as Equation (2.1):

$$K = \sqrt{(|K_o - K_s|)^2} = \sqrt{K_0^2 + K_s^2 - 2K_o . K_s} \qquad (2.1)$$

$$\cong \sqrt{4K_0^2 Sin^2\left(\frac{\theta}{2}\right)} = 4\pi n_0 \sin\left(\frac{\theta}{2}\right)/\lambda_0$$

In the light scattering process, an incident light source located at a distance much larger than the particles size, illuminates the medium. Since scattering intensity is determined at a far distance between the sensor and particles, both scattered and incident light act as a plane-wave. The cross section in between the viewing cone of the sensor and incident light defines the scattering volume in which there may be only one particle or a lot of particles. Scattering happens as a result of the electric field alteration by all particles in the scattering volume when illuminated by the incident light. Because light scattering is omnidirectional, the intensity acquired by the sensor is proportional to its sensing area and inversely proportional to the square of its radius from the scattering medium. While the suspension scatterer (air or homogeneous liquid) can also scatter light, its magnitude can be ignored when compared to the magnitude of the scattering from other particles. There are a few exceptions to this, for example when the volume of the particle is similar to that of the medium molecules or if the medium used is not homogeneous (Xu & Scarlett 2002, pp. 60-63).

Light scattering properties can be computed by directly solving Maxwell's equations (Mishchenko, Travis & Lacis 2002, p.60). The T-matrix solution, known as the most effective algorithm for calculating light scattering properties for non-spherical particles, introduced by Waterman (1971); Waterman (1995); Wielaard, Mishchenko, Macke & Carlson (1997) and Mishchenko, Travis & Lacis (2002). In this technique, which is also known as null filed method, the incident and scattered electric fields are stated in spherical vector wave function (Equations 2.2 – 2.3).

$$E^{inc}(r) = \sum_{n=1}^{\infty} \quad \sum_{m=-n}^{n} [a_{mn} RgM_{mn}(kr) + b_{mn} RgN_{mn}(kr)] \qquad (2.2)$$

and

$$E^{sca}(r) = \sum_{n=1}^{\infty} \quad \sum_{m=-n}^{n} [p_{mn} M_{mn}(kr) + q_{mn} N_{mn}(kr)] \qquad (2.3)$$

where k is the wavenumber for each given wavelength (λ). $Rg\ M_{mn}$ and $Rg\ N_{mn}$ from Equation 2.2 and M_{mn} and N_{mn} in Equation 2.3 are regular and propagating spherical vector wave functions respectively, p_{mn} and q_{mn} are the expansion factors of the scattered field and are primarily unknown, whereas a_{mn} and b_{mn} are computed by simple analytical expressions. Since the Maxwell's equations are linear therefore there is a linear relationship between the expansion factors of the scattered and incident fields.
Since the elements of the T-matrix are not related to the scattered and incident fields and only depends on the refractive index as well as morphological parameters of the scattering particle, therefore, the T-matrix must be estimated in advance for a given scattering particle (Mishchenko, Travis & Lacis 2002). The Stokes vector, defined by George Gabriel Stokes in 1852, are a series of values that used to describe the elements of scattered and incident light which describe either the indicative of the physical characteristics or provide direct measure of the scattering medium. Equation 2.4 shows the transformation matrix between the incident and scattered light.

$$\begin{bmatrix} I^{\mathrm{sca}}(\theta) \\ Q^{\mathrm{sca}}(\theta) \\ U^{\mathrm{sca}}(\theta) \\ V^{\mathrm{sca}}(\theta) \end{bmatrix} = \frac{1}{r^2}\frac{1}{k^2} \begin{bmatrix} F_{11}(\theta) & F_{12}(\theta) & 0 & 0 \\ F_{12}(\theta) & F_{22}(\theta) & 0 & 0 \\ 0 & 0 & F_{33}(\theta) & F_{34}(\theta) \\ 0 & 0 & -F_{34}(\theta) & F_{44}(\theta) \end{bmatrix} \begin{bmatrix} I^{\mathrm{inc}} \\ Q^{\mathrm{inc}} \\ U^{\mathrm{inc}} \\ V^{\mathrm{inc}} \end{bmatrix} \qquad (2.4)$$

Where (I, Q, U, V) are the Stocks vector parameters of the incident and scattered light, r is the distance from the detector to particles, k is a wave number and Fi (θ) describe various properties of the scattered light, for example, total intensity of incident light, degree of polarization and non-sphericity factor of particles (Hovenier et al. 2003). Using the T-matrix approach, the angular alignment of the elements of Stokes scattering matrixes can be calculated for randomly distributed and oriented particles. Several studies have been conducted on the light scattering process caused by smoke particles. Aggarwal & Motevalli (1997) used the spherical model as the shape approximation of smoke particles to study the light scattering effect, however, the SEM micrographs of smoke mixtures show that they are actually not spherical but more branched in chains. It was argued by other researchers (Manickavasagam & Menguc 1979; Liu & Mishchenko 2005; Klusek, Manickavasagam & Menguc 2003; Qiyuan et al. 2007) that the spherical model by itself cannot illustrate morphologic properties of smoke mixtures such as particle alignment hence cannot lead to a considerable improvement of extinction and scattering related to those measured from the Mie theory. Therefore, the impacts of smoke agglomeration and array morphology with in-depth frameworks of smoke mixtures were considered to study. Qiyuan et al. (2007) discussed that although the individual smoke particles are almost spherical, the combination of smoke particles in a chain-like shape is clearly non-spherical. He used spheroid models to approximate the shape of smoke particles for studying the effects of the non-spherical morphology of smoke mixtures in light scattering. Smyth & Shaddix (1996) In addition to the size distribution and alignment of the smoke particles, their refractive index is an important parameter to consider in light scattering, this index depends on the type of burning fuel and also combustion form as discussed at section 2.3. Smyth & Shaddix (1996) showed that the imaginary portions of smoke particles refractive indexes produced by flaming fires are bigger than those from smouldering fires. Qiyuan et al. (2007) used this method to measure the light scattering from smoke particles caused by smouldering and flaming fires. They concluded that the non-spherical property of grey smoke particles generated from smouldering fires has considerable effects on their light scattering than those produced by flaming fires which is a function of the wavelength of the incident light and spectral sensitivity of the imaging sensor.

Three types of scattering occur:

- Rayleigh scattering
- Mie scattering
- Non-selective scattering or Mie scattering of large particles

The first type of scattering is called Rayleigh or molecular scattering which occurs when atmospheric particles are considerably smaller than the wavelength of radiation (< 1/10 λ) these are mainly gaseous molecules. The amount of Rayleigh scattering is inversely proportional to the fourth power of wavelength. As a result, shorter wavelengths are affected more than longer wavelengths. This explains the blue appearance of a clear sky, as visible blue radiation (λ ~ 400 nm) has five times greater scattering from visible red radiation (λ ~ 600 nm).

Mie scattering occurs when the diameter of the particles in the atmosphere are approximately the same as the wavelength. Dust and water vapour are important agents for Mie scattering. In Mie scattering more of the intensity of the scattering goes in forward direction in a single dimension (Figure 2.8). If EMR interacts with particles that are several times larger than the radiated wavelength, then Non-selective scattering occurs with strong forward scattering peak and smaller degree of backscattering. Large smoke particles, water droplets and dense clouds are the important non-selective scattering agents.

In cases of Rayleigh or Mie scattering, imaging sensors receive the energy reflected by atmospheric particles as well as the energy reflected from ground objects. Energy reflected from molecular particles in the atmosphere is known as path radiance or atmospheric light. By estimating this component, the image visibility can be enhanced using the advanced image processing techniques, this is broadly discussed at Section 7.3.

Image has been removed due to copyright restriction.

Figure 2.8. Mie and Rayleigh scattering pattern (Hungate, Watkins & Borengasse 2007, p. 34).

Unlike scattering which reflects the EMR and degrades the captured image, atmospheric absorption affects the amount of energy in certain wavelengths. Absorption relatively degrades the reflected energy from ground objects before reaching the imaging sensor. Similar to scattering, the absorption effect can be corrected by comparing simultaneous measurements made at several bands. Interaction of EMR with ground objects is also important in remote sensing but is not relevant to the context of this research, therefore is not reviewed in this chapter.

2.6. Smoke particles effect on multi-spectral and TIR imaging

Sensor systems such as multi-spectral and thermal cameras that have formerly been limited to utilize due to the high-cost and technology aspects, are now becoming commonly available and economical. Similarly, new airborne sensor platforms, especially small, unmanned aircraft, are helping new applications for airborne remote sensing. Multi-spectral sensors systems incorporate multiple spectral bands for sophisticated fire monitoring and detection. For example, most recently an advanced multi-spectral geostationary operational environmental satellite (GOES-16) was launched by NASA and become operational on December 2017 for real-time detection and monitoring of wildfires. GEOES-16 utilizes an advanced baseline imager (ABI) technology for imaging Earth’s environment and has 16 spectral bands (two visible channels, four near-infrared, and ten infrared bands from 0.45 – 13.6 µm) with extremely high temporal resolution from 30 seconds to 15 minutes) and relatively good spatial resolution from 0.5 – 2 km. In July 2017, southern California faced a record-breaking heatwave which triggered two large wildfires and captured by GEOES-16 satellite (Figure 2.9).

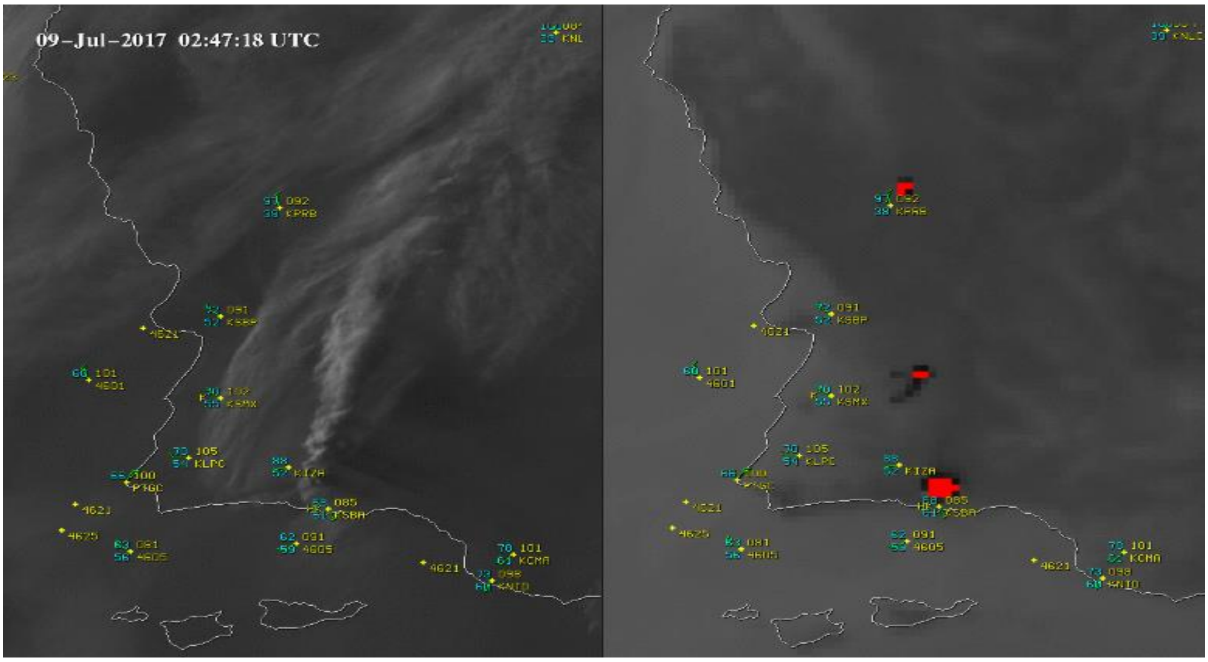

Figure 2.9. GEOES-16 red band (0.64 µm) (left image) showing the smoke plumes and the same scene collected with shortwave IR (3.9 µm) band (right image) showing transparent smoke plumes with identified hot spots in reds (Courtesy of NASA).

While this newly launched satellite sensor has very high temporal resolution, its spatial resolution is not enough for detecting targets and small objects. There is a trade-off between temporal and spatial resolution for satellite sensors. For example, WorldView-3 multi-spectral sensor with sensitivity from 0.45 µm – 2.365 µm and spatial resolution of 3.7 m at SWIR bands can revisit the same area of interest every 4.5 day with 20 degree or less off-nadir angle (DigitalGlobe 2018).

Images from these multi-spectral sensors can be affected by environmental conditions such as presence of aerosols, fog, haze and smoke particles in atmosphere as well as variations in the sun illumination while imagery is being captured, which degrade the image visibility and lead to loss of spatial resolution. Several models have been developed over the past decades to compensate for the atmospheric conditions in remote sensing (Hadjimitsis et al. 2010). Richter (1996) introduced a new method focusing on individual spectral band and matching the histograms between haze regions and clear areas to correct haze in SPOT HRV and Landsat TM satellite images. Chun et al. (2004) adopted a homomorphic filter to enhance the image visibility for ASTER data. Du, Guindon and Cihlar (2002) used the wavelet transformation to enhance the spatially varying haze with decomposed images. Liu et al. (2011) used virtual cloud point method with the background suppressed haze thickness index to enhance the image visibility for high spatial resolution satellite imagery. Chavez (1995) took the band correlation property of atmospheric scattering into account and used the dark-object subtraction method to minimize the effect of uniform haze. Makarau, Richter, Muller and Reinartz (2014) calculated the haze thickness by taking channel correlation property into account to enchase randomly distributed haze on satellite imagery. WorldView-3 uses an additional atmospheric sensor as part of its payload with slightly wider swath to detect the atmospheric particulates at 31m resolution, therefore estimates the exact atmospheric conditions for every captured image. Figure 2.10 shows an image captured by Worldview-3 sensor over an active fire after applying the atmospheric corrections.

To address both low temporal and low spatial resolution space-based multi-spectral imaging, airborne multi-spectral cameras are developed to collect high-spatial resolution imagery by flying at lower altitudes. For example, the autonomous modular sensor (AMS) has been developed by NASA and actively used for wildfire monitoring and remote sensing. It can be deployed on manned or unmanned aircraft and is able collect 12 spectral bands from 0.42 to 11.26 µm (Ambrosia et al. 1999). Between 2006 and 2010 the AMS was used on the Ikhana unmanned aircraft (Figure 2.11) and NASA’s B-200 King Air to evaluate its capabilities and operational readiness to provide support to national emergency demands for wildfire data. NASA has updated the AMS

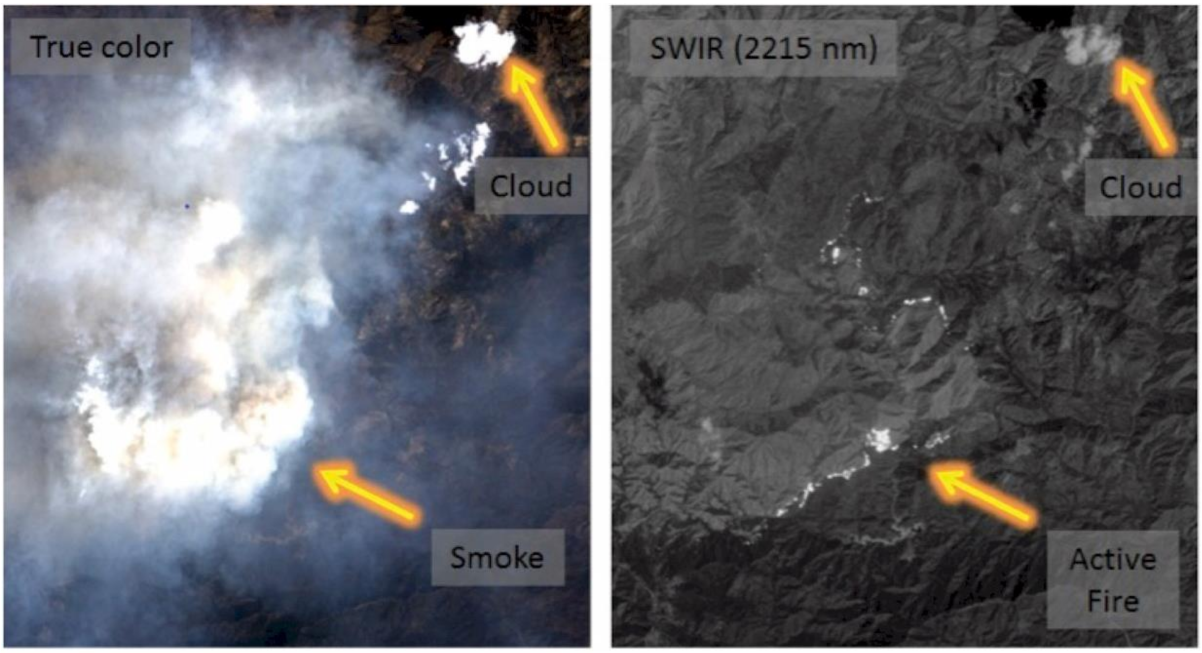

Figure 2.10. left image captured by WorldView-3 optical sensor over an active wildfire with smoke and cloud, right image captured using the same sensor at 2215 nm band which has passed through smoke and cloud with clear fire location (Courtesy of NASA).

Figure 2.11. NASA's IKHANA unmanned aircraft equipped with AMS multi-spectral sensor to collect and transmit remotely sensed data from wildfires in near real-time to the command centre with 20 hours endurance and up to 40,000 feet flight altitude (Courtesy of NASA Ames research centre).

with new firmware and improved remote command control system which has been initially tested in January 2018 and is subject to more flight test by the end of 2018 (NASA 2018).

Figure 2.12 shows an image captured by NASA AMS sensor using the IKHANA UAV over the Basin Fire Complex in California on July 2008.

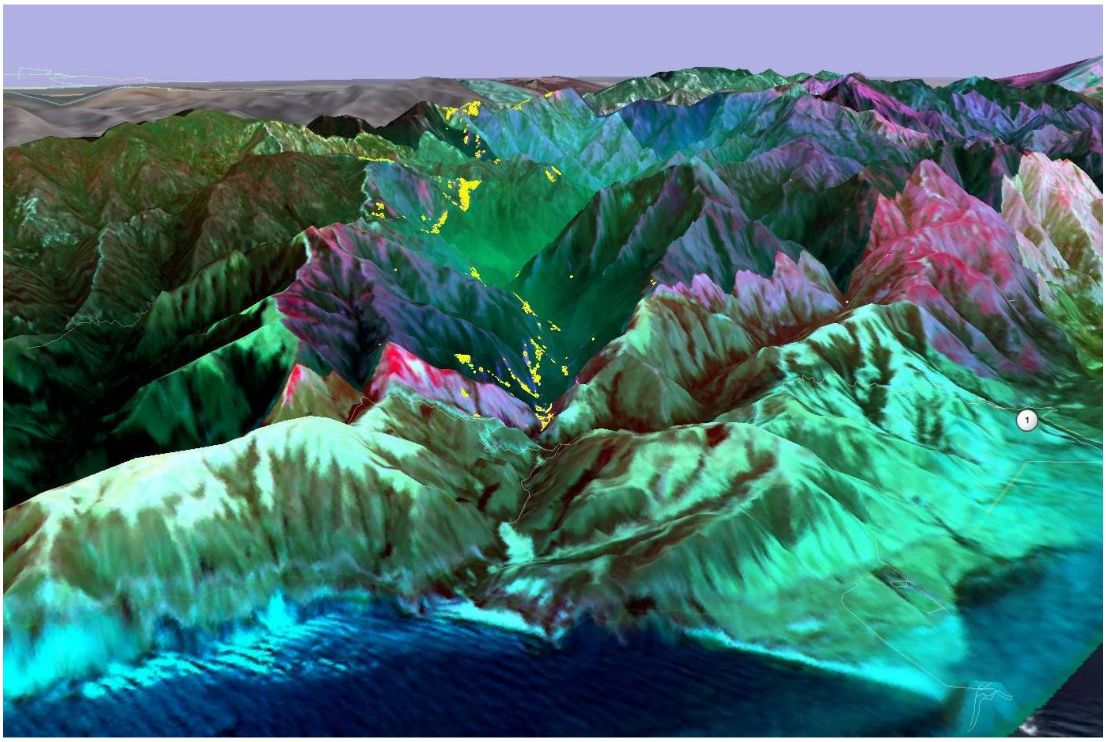

Figure 2.12. Multi-spectral AMS image captured over an active fire in California and overlaid onto elevation data within Google Earth. The yellow sections represent active fire regions with purples and reds showing burned areas (Courtesy of NASA and Google).

There are other imaging sensors such as thermal cameras which can be used on lightweight and low-cost UAVs or hand-held devices which are mainly used in firefighting for identifying hot spots, seeing through smoke, locating and rescuing people, safe navigation during rescue missions and many other industrial applications. Unlike optical cameras in which reflected radiation is measured by the sensor, thermal cameras measure the emitted radiation from objects and convert the intensity of the recorded energy to a visible image. Atmospheric windows in the thermal region of spectrum are from 3 – 5 µm and 8 – 14 µm (Sabins 1996) which define therefore the typical operational ranges for thermal cameras (Figure 2.3). As discussed in section 2.3, depending on the wavelength of the incident light and particle size, light can be scattered in three forms: Rayleigh, Mie and Non-selective scattering. This means cameras operating at longer wavelength of the EMS, such as thermal cameras, are less prone to the effects of scattering process compared to cameras operating at visible wavelengths, therefore thermal cameras can see through smoke particles due to significantly reduced scattering.

In bushfires, in addition to the dense smoke in the vicinity of a fire front, large areas up to several kilometers away can be affected by gaseous smoke in the lower atmosphere (Dennekamp et al. 2011), and visibility levels significantly drop in such areas. In these situations, having high-spatial resolution insights to detect small objects such as road signs and ideally a true colour vision from the scene is crucial. The lack of visibility may cause series injuries or death. Although advanced multi-spectral and TIR sensors can penetrate smoke and provide valuable information such as hotspots and temperature variations objects, due to their monochromatic imaging sensor and low-spatial resolution, visual interpretation of captured images is very challenging. Figure 2.13 shows how visibility can be dramatically degraded by gaseous smoke particles in areas located further away from the fire source.

The spatial resolution of a TIR sensor is dependent on its total field of view (TFOV) and also its instantaneous field of view (IFOV). TFOV, is described as the projection of the camera sensor at the target surface, and IFOV is defined as the field of view of a single pixel in the sensor’s detector array (Kaplan 2007, pp. 40-43). As discussed in section 2.2, the amount of photon energy decreases as the wavelength increases, therefore, to ensure that enough energy reaches the detector, thermal sensors have larger IFOVs and as a consequence have coarser spatial resolution. Thermal camera manufacturers publish the spatial resolution of the thermal sensors as a constant number in radiance which is used for calculating the IFOV of the thermal detector at any given distance. TOFV depends on the focal length or angular field of view of the camera lens. Figure 2.14 shows how IFOV is calculated at a given distance. For example, for a thermal camera with published spatial resolution of 0.002 radians the IFOV at 500-meter distance would be: 0.002*500=1 meter.

Image has been removed due to copyright restriction.

Figure 2.13. low visibility in areas located 12km away from the 2006 Victorian Alps bushfire in Australia. Road travel in these areas will be hazardous due to low visibility. (Courtesy of Country Fire Authority- CFA, Melbourne).

Different objects with various colours, shapes and sizes may appear in an airborne or space-borne image, some of these objects may be easily interpreted and identified by human brain while others may not. Visual image interpretation is defined as a practice of seeing, identifying and communicating the information. Three important aspects that aid the visual interpretation of airborne or space-borne images are: the vertical perspective of features, frequent use of non-visible wavelengths for image collection

Image has been removed due to copyright restriction.

Figure 2.14. TFOV of a thermal camera sensor which effectively is the total projection of the camera sensor at given distance d, and IFOV is the field of view of a single detector component or pixel at that distance (Kaplan 2007, p.41).

and, finally, the scale and resolution of the features (Campbell and Wynne 2011). The experience of the image interpreter and image properties such as quality, texture, tone, shadow, pattern, association, shape and size are some of the main elements that contribute to successful visual image interpretation (Lillesand, Kiefer and Chipman 2015, pp. 59-62). There are some other issues utilizing TIR or multi-spectral sensors for collecting, processing and analysing the collected data over a large area as follows. Low-cost TIR and multi-spectral cameras contain some undesirable anomalies such as horizontal banding noise and non-homogeneous radiometry (Fernández-Guisuraga, Sanz-Ablanedo, Suárez-Seoane and Calvo L., 2018). Additionally, to collect high-spatial resolution TIR imagery, a large volume of raw data has to be captured, for instance using a low-altitude UAV to cover a large area. Handling, processing and managing this large volume of data is labour-intensive and requires powerful computer resources to generate the final usable multi-spectral data for further analysis.

Figures 2.15.a and 2.15.b show two aerial images captured by ARA using a thermal and a DSLR camera simultaneously over the same area, in a clear smoke-free atmospheric conditions, to compare the effects of spatial resolution. Comparing these two images shows that due to the greatly coarser spatial resolution and black and white appearance of thermal image, the human brain can easily misinterpret the contents of the thermal image.

(a) (b)

Figure 2.15. (a) Grayscale image represents the temperatures of the objects captured using a FLIR thermal camera and (b) a true colour image captured by a Canon DSLR camera at 500-meter height.

In remote sensing, in order to use multi-resolution and multi-source data, image fusion trajectory have been developed as part of digital image processing techniques to extract high quality information from imagery (Pohl and Genderen 2015). These techniques have been used by researchers to improve the spatial resolution of thermal images by merging information from another high-resolution image which is usually from the visible part of the EMS. (Rodriguez et al. 2011; Zhao et al. 2013; Poujol et al. 2016). One of the main requirements for thermal image fusion is a good image registration between the high spatial resolution visible and the low spatial resolution thermal image. Since images are captured using two different sensors, feature matching between two sources can be challenging (Sonn, Bilodeau & Galinier 2013). For example, image fusion fails or gives very poor results if the visible image is covered by smoke and image visibility is degraded. Improving the scene visibility for the images captured by a single digital camera is discussed in the next section.

2.7. Single image visibility enhancement

Haze and Smoke in the atmosphere at the time of image acquisition, scatters or absorbs radiation as travels from ground objects to the sensors. These processes degrade image contrast and quality. Thus, identification of ground features becomes difficult and is sometimes impossible (Narasimhan & Nayar 2002). Over the past decades, many different approaches to minimize the effects of haze in visible imagery and enhance scene visibility have been developed, e.g., Vincent (1972), Chavez (1988), Guindon & Zhang (2002) and Fattal (2008).

Liu et al. (2011) introduced a three-step haze removal technique from high resolution satellite imagery comprising haze detection, haze modelling and haze removal. In this method, a background haze thickness index is used to estimate relative haze thickness for haze reduction. This technique requires a clear region of the image without haze for calculating the background haze thickness. Human intervention is also required during the entire process using this technique. He, Sun & Tang (2011) presented a new technique based on a dark channel prior method. They observed that in clear atmospheric conditions at least one colour channel of a captured image has some pixels with very low intensities. Their work was inspired by the dark object subtraction (DOS) method introduced by Chavez (1988) for correcting atmospheric scattering effects in optical data. The DOS method attempts to identify several pixels with very low reflectance. Due to the presence of haze, these identified pixels are not completely dark and therefore their DNs are not zero and are considered as a measure of haze thickness. Assuming constant haze over the entire image, subtracting the haze thickness from initial image provides a haze-free image. He, Sun & Tang (2011) improved the DOS method by searching for dark objects in local and non-overlapping patches instead of the whole image. They showed that in an image covered by haze, the path radiance or amount of the light scattered by the particles contribute in estimated dark channel values which can then be used for estimation of a haze transmission map.

Long et al. (2014) improved the speed and performance of He, Sun & Tang's (2011) method by introducing a low-pass Gaussian filter instead of the initial soft matting method used by He, Sun & Tang (2011) to eliminate the halo artefacts and also verified that the dark channel prior method is a suitable technique in remote sensing. They collected one thousand haze-free remote sensing images and then calculated the dark channel images based on He, Sun & Tang's (2011) method for each of them. The intensity histogram of the computed dark channels for all the sample images showed that the intensity of >74 percent of the pixels in the dark channels was less than 25; thus, confirming the validity of this method in remote sensing. Based on this, the pixels covered by haze will have higher intensity in areas with denser haze and this can be used for estimating the haze thickness over the entire image and restoring a haze-free image.

In the last two years Zhai & Ji (2015) and Jiang et al. (2016) have developed new optimized methods for haze removal from a single image using a combination of techniques. Zhai & Ji introduced a further scene transmission optimization compared to He, Sun & Tang (2011) by implementing a total variation (TV) regularization technique which is a common method in digital image processing for noise removal. TV-regularization is based on the principle that reducing the total variation of a signal with a close similarity to the original signal, removes unwanted noise and preserves important details (Rudin, Osher & Fatemi 1992).

Jiang et al. (2016) argued that because there is a high correlation between visible red and visible blue channel DNs under a clear sky condition, a direct line can be defined in two-dimensional blue and red space. The direction of this line depends on physical characteristics of the scene, such as, amount of haze. The amount of haze in any pixel has a direct correlation with its distance from this line, this makes it possible to estimate a haze map to be subtracted from the original image for haze-free image restoration. Figure 2.16 shows a sample image that partially covered by haze and optimized by this method.

Image has been removed due to copyright restriction.

(a) (b)

Figure 2.16. Efficiency of eliminating the haze from a single optical image (a) using the proposed method by Jiang et al. Because there are clear regions in the entire scene, the haze-free image (b) can successfully be restored (Jiang et al. 2016).

In summary, He, Sun & Tang's (2011) method is the most efficient way for single image haze removal and is commonly used as the basis for other related research for increasing scene visibility. However, a basic requirement that is common to all of these methods is to identify the parts of the image with no or minimal haze contamination in order to estimate the haze map and restore the haze-free image. Therefore, if the entire scene is covered by smoke or haze, these methods would lose their effectiveness. If an area sensed is entirely covered by haze and there are no clear regions, the restored image using He, Sun & Tang's (2011) method does not provide any additional details.

2.8. Multi-image visibility enhancement

In addition to single sensor image visibility enhancement discussed in the previous section, the use of multiple imagery has also been considered by researchers for scene visibility enhancement. Schechner and Karpel (2005) introduced a method for scene visibility enhancement by using a polarization filter on a camera that enabled it two images to be captured at different angles. The method is based on the fact that scattered atmospheric light is partially polarized, and by taking this into account the image formation process is modelled and used to invert the process and remove haze. Since this method relies on the partial polarization of the atmospheric light, it will be less effective as the degree of polarization decreases. For example, it may fail in conditions of fog or dense haze. Liang et al. (2015) proposed a new method aiming at handling dense haze and optimizing scene visibility in which four images are collected at different polarization angles. However, polarized-based methods using two or more images from the same scene at different angles are not applicable for dynamic scenes in which haze particles move rapidly, such as bushfires, compared to the rotation speed of the polarized filter.

Another approach to multi-image visibility enhancement is to use a pair of cameras, one acquiring NIR imagery and the other colour visible imagery. Because of relatively lower scattering of NIR radiation compared to visible radiation, NIR images can capture more details than a visible image in a hazy environment. This spectral difference property between two different images has been widely exploited in computer vision for improving image quality and eliminating haze effects. Schaul, Fredembach & Susstrunk (2009) showed that in outdoor photography using digital colour cameras, distant objects are usually blurred and hard to see. They proposed a solution in which fusion was applied to a pair of NIR and visible images based on a weighted least square multiresolution decomposition method. This method requires multiresolution fusion criteria for maximizing the contrast of each individual pixel to improve the haze effect. Feng et al. (2013) used the stronger penetration capability factor of the NIR light to minimize the scattering effect in visible light to unveil details of distant features in landscape photography. In their method, they used a pair of NIR and visible images. The NIR image was used to find clear regions of the image for haze thickness and atmospheric light estimation. They then used He, Sun & Tang's (2011) developed method for estimating the haze thickness and path radiance. Vanmali, Kellar & Garde (2015) introduced an optimized method for removing the haze from a pair of visible and NIR image with less complexity and computation time compared to other proposed methods. They refined the dark channel prior method proposed by He, Sun & Tang (2011) to improve the accuracy of atmospheric light estimation. Figure 2.17 illustrates results from the application of their method and shows the improvement in the contrast and in vivid colour perception.

Image has been removed due to copyright restriction.

Figure 2.17. Pairs of images that illustrate haze removal using Vanmali, Kellar & Garde's(2015) method. The images on the left are hazy images and those on the right are the same images after the application of the method. (Vanmali, Kellar & Garde 2015).

In the research on NIR-guided visibility enhancement, all of the methods proposed are based on a pair of NIR and visible image acquired simultaneously with the implicit assumption that the pair of images are well aligned and accurately co-registered. Image alignment is critically important in making sure that every pixel from one image is precisely aligned with the corresponding pixel in the other image. It is the main requirement before image fusion algorithms can be applied. These methods cannot be easily adopted and used in challenging environments with dynamic backgrounds caused, for instance, by the motion of smoke particles; or if the cameras or other sensors are mounted on moving platforms such as UAVs or manned aircraft. Therefore, the following section reviews the possibility of collecting NIR data simultaneously with other visible bands without using multiple cameras.

2.9. Spectral response of DSLR camera sensors

With recent advances in optical sensor technology, high-resolution DSLR cameras that are deployable on manned and unmanned or any airborne and ground-based platform, are being increasingly used in remote sensing for applications that include environmental studies (Levin, Ben-Dor & Singer 2005), crop monitoring (Sakamoto et al. 2012), agricultural studies (Yang et al. 2014) and crop identification (Zhang et al. 2016). These studies have shown that a DSLR camera can be used in collecting radiometric information that can be used in analysis for a range of environmental applications. Images captured by a DSLR camera have many advantages over satellite imagery such as lower cost, near-real-time data capture and higher spatial resolution. The sensors used inside DSLR cameras are either of the charge-coupled device (CCD) or complementary metal-oxide-semiconductor (CMOS) types. These sensors collect true colour information by employing a Bayer filter which arranges RGB colour filters across the pixel array of the camera sensor and collects one of the three main colours for each pixel. The processor in the camera then applies various de-mosaicking algorithms and interpolates a co-registered red, green and blue values for each individual pixel. This is explained in more detail in section 4.3. The spectral resolution of a DSLR camera describes the relative efficiency of EMR detection by the colour filters used in the camera's detector.

Mangold, Shaw & Vollmer (2013) conducted a comprehensive study on the physics of NIR photography using DSLR cameras. DSLR camera sensors contain millions of light detectors made of silicon, which converts incident light to an electric signal. Silicon-based detectors have a typical sensitivity response curve (Figure 2.18). This spectral response curve means that a typical DSLR camera has the potential to detect NIR radiation. They found that silicon-based DSLR camera sensors have high sensitivity from the visible to the NIR regions of the EMS (400 nm – 1100 nm). In human eye, stimulation of long, middle and short wavelength-sensitive cones with light generates the visual sensation. Because human visual sensation is limited to the visible regions of the EMS, the NIR part of EMR is usually blocked in DSLR cameras using an IR cut-off filter so that image colours can match the human visual sensation. This cut-off filter does not alter the camera sensor's sensitivity to NIR light but just filters out the incoming EMR in NIR region of the EMS. Therefore, if the cut-off filter is removed, a DSLR camera will capture an image that also contains the response of NIR radiation.

Image has been removed due to copyright restriction.

Figure 2.18. Typical sensitivity curve of a silicon sensor starting from 250 nm (UV) to above 1100 nm (NIR). S-cones, M-cones and L-cones are respectively short, middle and long wavelength cones perceivable by humans from 400 nm – 700 nm (Sadeghipoor et al. 2013).

Indeed, Rabatel, Gorretta & Labbe (2011) showed that a DSLR camera sensor can be modified to simultaneously collect red and NIR light in one image by removing the NIR cut-off filter. They used the data obtained from the modified camera to calculate a normalized difference vegetation index (NDVI) for crop monitoring applications. Figure 2.19 shows spectral response of a typical DSLR camera sensor. It is clear that the sensitivity of each of the red, green and blue channels also encroaches into the NIR. Therefore, it can be argued that R, G and B respectively are in fact R+NIR, G+NIR and R+NIR. By modifying the camera by adding a custom filter to block blue light, the NIR component of blue light would be collected in blue channel. This finding is an aid to designing custom filters with desired wavelengths for specific applications. Rabatel, Gorretta & Labbe (2011) obtained highly satisfactory results for computed NDVI values using a modified camera sensor and showed that a typical DSLR camera senor has more potential in remote sensing than simply obtaining photographs in the visible wavelengths.

Image has been removed due to copyright restriction.

Figure 2.19. The spectral response of red, green and blue channels of a typical silicon sensor used in DSLR cameras. (Rabatel, Gorretta & Labbe 2011).

2.10. Chapter Summary

In this chapter wildfire formation, combustion stages and fuel types was reviewed followed by a discussion of smoke particulate components and techniques for detecting them. Smoke particle size and characterization methods were also discussed, and it was shown that incoming solar radiation can be partially scattered, absorbed or reflected and that the magnitude of EMR scattering is a function of morphological and optical properties of aerosols as well as total intensity of incident light, degree of polarization and the non-sphericity factor of particles.

Multi-spectral and TIR imaging sensors mounted on various platforms such as satellites, manned or unmanned aircraft are subject to image visibly degradation due to the presence of aerosols in the atmosphere. The visibility issue, caused by for instance wildfire smoke, is not noticeable in the SWIR and TIR region of EMS. However, although imaging cameras utilizing TIR or SWIR sensors can penetrate wildfire smoke, they are not capable of providing true colour, high-resolution images for detecting small targets such as people. In Section 2.3 the fact that although small UAVs by potentially fly at low altitudes to capture high-spatial resolution multi-spectral and TIR imagery was discussed. However, powerful computer resources and skilled operators are required to process the large volume of collected raw data to final deliverables for further analysis. Another issue in using TIR or SWIR imagery is their mono-colour or false-colour composite image outcomes. Although with image processing techniques such as image fusion and pan-sharpening using a pair of high and low-spatial resolution images it is possible to improve the quality of a low-resolution image, these techniques could fail to provide the outcomes required if the high-spatial resolution images are covered by smoke.

Consumer-grade DSLR cameras can capture high-spatial resolution colour imagery but can be degraded by smoke particles if captured in an environment in which smoke is present. In Section 2.7 research on scene visibility enhancement using single colour images collected by DSLR cameras was reviewed. Attention was paid to the limitations of using a single image. Following that discussion, research on improving the visibility of a hazy image using multiple images, such as NIR and visible image pairs, from the same scene was reviewed. It was concluded that multi-image-based solutions require very careful image alignment and registration before further processing can be attempted, and that sometimes this will require special equipment and cameras. Therefore, they cannot be considered as an easy-to-use, practical solution, this leads to an unambiguous knowledge gap in studying feasibility of collecting high spatial-resolution imagery over smoke-covered areas which is the focus of this thesis.

Chapter 3

Research Design and Methods

3. Research Design and Methods

3.1. Introduction

This chapter consists of two main parts, the first of which explains the main framework that was developed to address the research problem. The second part presents the approaches and methodologies that were applied.

3.2. Main Framework

Existing solutions and methods for penetrating smoke particulates in airborne remote sensing, as well as pertinent developments in different domains including image enhancement and haze removal methods were reviewed and discussed in the previous chapter. Although existing thermal or multi-spectral imaging sensors can penetrate smoke, the following problems were identified and highlighted in using such sensors in the context of this research:

- Monochromatic imaging sensors often have a too coarse spatial resolution to identify small, important objects
- When sensors are deployed on low altitude UAVs to address the spatial resolution issue, their effective ground coverage is relatively small due to the small FOV. Therefore, a very high number of images need to be collected to cover the entire scene which increases the required flight time
- Complex post-processing requirements in terms of skilled operators and powerful computers with specialized image processing software tools are normally required to process and produce usable data from these sensors

To recap from Chapter 1, following research questions were outlined:

4. Can images acquired by DSLR cameras, after modifications to full spectra, penetrate smoke? This question emanates from the first objective.

5. Is it feasible to design an optical filter to minimize the scattering effect on DSLR camera images without compromising true-colour? This question emanates from the second objective.
6. Can an image visibility enhancement algorithm be developed to improve smoke penetration from a modified camera setup? This question emanates from the third objective of this research.

Based on these questions a research design framework was developed (Figure 3.1) which outlines the steps required to develop a new method to penetrate smoke particulates at fine spatial resolution in a non-monochromatic image.

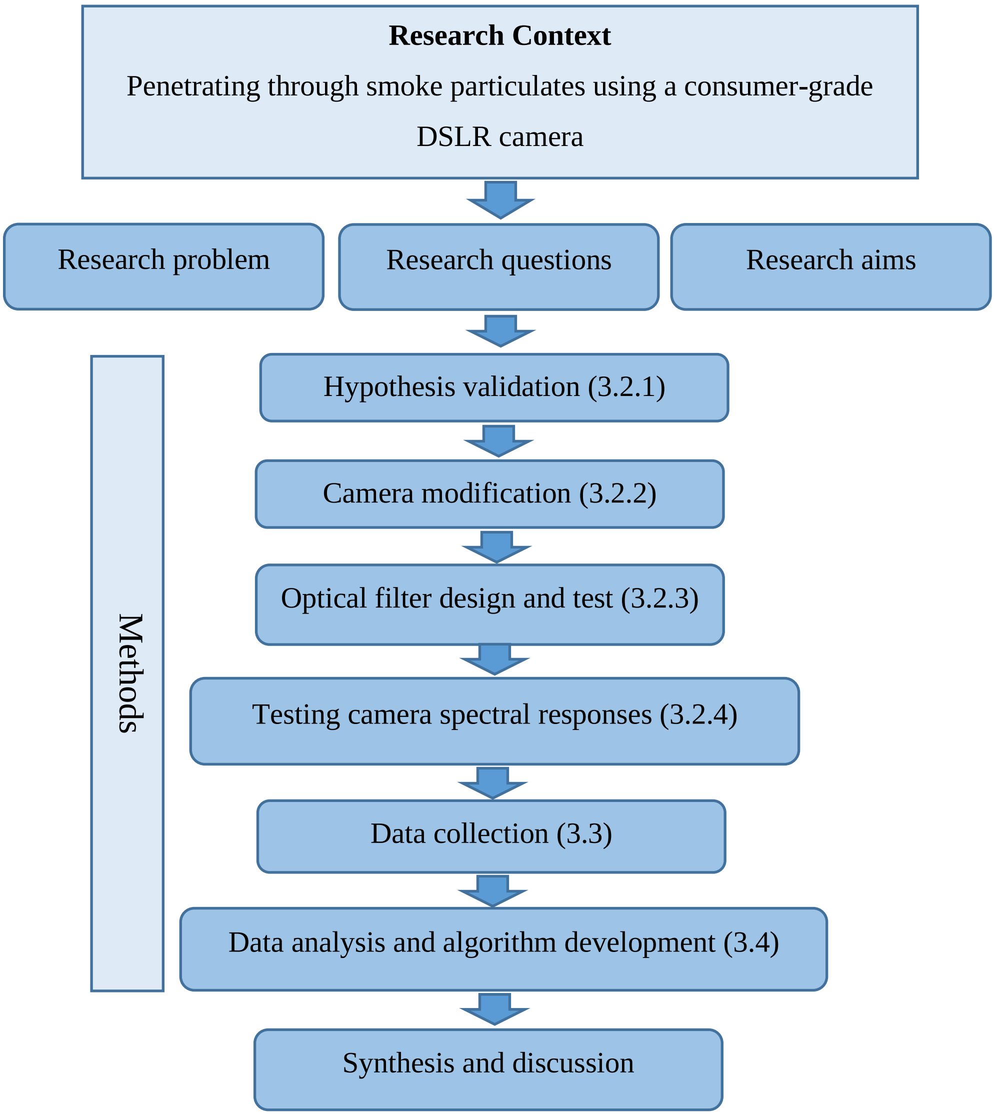

Figure 3.1. The research design framework, the numbers refer to the sections of this chapter.

3.2.1. Hypothesis validation

The very first action prior starting this research was to confirm the feasibility of the main hypothesis, which originates from the first and second research questions. Consumer-grade DSLR cameras are affordable and typically available with high-spatial resolution and large sensor size, i.e., a large ground footprint as opposed to TIR or multi-spectral SWIR sensors. However as discussed in Section 1.3, the existence of substantial numbers of smoke particulates in atmosphere at the time of data capture, caused for instance by an active bushfire, can minimize the spatial resolution and visibility of the images captured by DSLR cameras.

The spectral response of a typical DSLR camera sensor was discussed in Section 2.9 and it was shown that the silicon-based sensors used inside these cameras are naturally sensitive to the visible and NIR part of EMS but, because of the fact that human vision is limited to the visible EMS, the NIR radiation is intentionally blocked by camera manufacturers. The filter used to block IR radiation is known as an IR cut-off filter. Many images have been captured by DSLR cameras over smoke but as explained above they contain no information at IR wavelengths and hence they not suitable for further analysis for this research.

Required dataset for hypothesis validation must have these specifications:

- Collected from a bushfire smoke area
- Contain at least three main visible bands (400 -700 nm)
- Contain at least one NIR band between 700 – 1100 nm

For this purpose, following multi-sensor dataset was identified and sourced from ARA archive imagery which was captured over a bushfire using their research aircraft (Tables 3.1 – 3.3):

- Hyperspectral aerial imagery captured by an AISA EAGLE (Specim Limited, Oulu, Finland) hyperspectral scanner with 244 spectral bands (400 nm – 970 nm).
- TIR images collected by an FLIR A615 (FLIR Systems, Inc. USA) thermal camera with 7.5 µm – 13 µm spectral sensitivity.
- Optical images captured by a Canon EOS1D consumer-grade DSLR camera with three spectral bands (RGB from 400 nm – 700 nm)

All of these images were captured simultaneously over the same area.

Table 3.1 AISA EAGLE Hypesrspectral camera specifications

Detector Type	Progressive scan CCD camera
Spectrograph	High efficiency transmissive imaging spectrograph.
Spectral Range	400 – 970 nm
Number of spectral bands	244
Spectral sampling/band	2.3 nm
Spectral resolution	3.3 nm
Spatial Resolution	0.52m @1000m AGL
Frame Rate	50 Hz
Dynamic Range	12-bit

Table 3.2 FLIR A615 thermal camera specifications

Detector Type	Uncooled microbolometer
Image size	640 × 480 pixels
Spectral Range	7.5 µm – 13 µm
Spatial Resolution	1.3m @ 1000m AGL and 13mm focal length
Detector Pitch	17 µm
Frame Rate	50 Hz
Dynamic Range	16-bit
Standard Temperature Range	-20°C to 2000°C
Accuracy	± 2°C or ±2% of Reading

Table 3.3 Canon EOS-1D camera specifications

Detector Type	CMOS APS-H (27.9 x 18.6 mm)
Spectral Range	400 – 650 nm
Number of spectral bands	3
Image Size	4896×3264
Spatial Resolution	0.28m @1000m AGL and 20mm focal length
Dynamic Range	12-bit

The AISA EAGLE hyperspectral camera utilizes a silicon-based imaging sensor, like that used in consumer-grade DSLR cameras but with narrower bands and higher spectral sensitivity. Data from the AISA EAGLE camera was processed and each individual band was analysed to examine the light scattering effects in visible (400 nm – 700 nm) and NIR (700 nm – 970 nm) wavelengths. For this process, accurate position and IMU data captured by RT4000 (Oxford Technical Solutions, Oxford, UK) inertial and dual-GPS navigation system used in NAVGRAPH software (Oxford Technical Solutions, Oxford, UK) were used for image geo-referencing. The geo-referenced imagery was used to analyse and simulate light scattering effects at different wavelengths.

Images from the DSLR camera were used to study the effect of smoke particulates in the context of spatial resolution and how this can affect scene visibility spatially in automated image matching and feature detection applications. In this case PhotoScanPro ver. 1.4.4 (Agisoft LLC, St. Petersburg, Russia) was used for pixel correlation. Both TIR and DSLR imagery were captured with adequate overlap (> 70%) for geo-rectification and image mosaicking. These data were collected over an active bushfire located 20 km north east of the Parafield Airport in South Australia (Lat: -34° 42´, Long: 138° 50´) on November 2013 (Figure 3.2).

The ECO-Dimona manned aircraft owned by ARA was flown at 600m AGL over a 130 ha area. As mentioned earlier it was equipped with AISA EAGLE spectral imaging senor, a FLIR A615 TIR camera and a Canon EOS1D optical DSLR camera. Figure 3.3 shows the aircraft pod with ASIA EAGLE hyperspectral sensor and its storage unit.

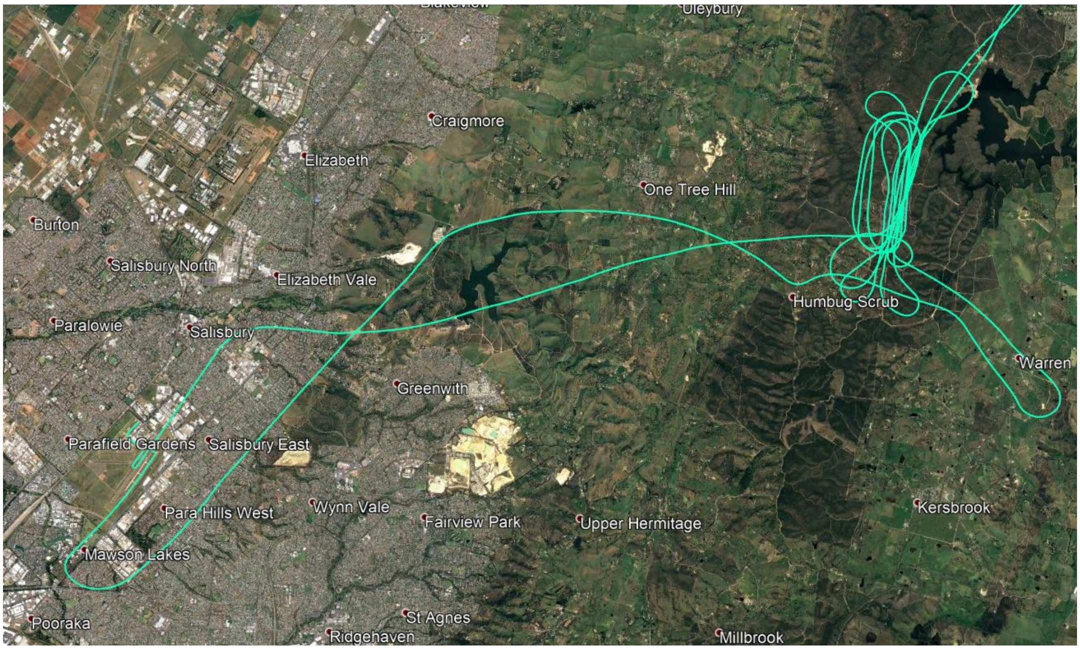

Figure 3.2 Green lines show the flight path of the ARA aircraft taking-off from the Parafield airport, flying over bushfire area in nine flight lines, and then returning to the airport (Courtesy of ARA and Google Earth).

Figure 3.3. The AISA EAGLE hyperspectral sensor with high power data acquisition system and storage unit on ECO-Dimona aircraft pod.

The AISA EAGLE is a push broom scanner with a focal length of 17 mm and 1024 spatial pixel counts with 2.3 nm spectral sampling per pixel. It can scan the ground across a flight line with 0.7 m-ground resolution at 1000 m altitude (AGL) collecting 244 spectral bands per each pixel and up to 50 images per second. The spatial resolution of the data collected over the bushfire was 0.5 m at 600 m AGL with a swath width of 410 m on the ground. In this camera, each band includes radiometric calibration metadata for computing radiance of the ground features using the CaliGeo program (Specim Limited, Oulu, Finland) as a plug-in to ENVI image processing software (Exelis Visual Information Solutions, Inc. USA). The FLIR A615 camera acquires data over a 640×480 pixel area at a focal length of 13.1 mm. It was used to collect TIR imagery simultaneously over the bushfire with 0.8 m-spatial resolution at 600 m AGL. The Canon DSLR EOS1D camera acquires a 4896×3264-pixel image and has a 20 mm focal length. It was used to collect RGB images (400 nm – 700 nm) at 20 cm image resolution over a 900×600 m ground coverage for each image at 600 m AGL. These datasets were processed radiometrically and geometrically in further analyses to simulate the smoke pentation capability of a silicon-based imaging sensor in the NIR region of EMS using ENVI image processing software. Chapter 4 will discuss the (satisfactory) outcome of this verification exercise and how it led into the modification a consumer-grade DSLR camera sensor to detect a full spectrum between 400 nm – 1100 nm, and how a custom optical filter was designed to address the objectives of this research.

3.2.2. Camera modification

In Chapter 1 the light scattering effects of smoke, fog, haze and other particles in the atmosphere were discussed along with how they can potentially compromise the quality and visibility of digital images, particular reference was made to images captured by DSLR cameras. Rayleigh's scattering law states that the amount of radiation scattering by particles in the atmosphere is inversely proportional to the fourth power of wavelength, which means that the scattering effect is more apparent in the blue end of the visible spectrum. In contrast, NIR is less scattered than visible radiation and as a consequence NIR images are less affected by smoke, haze and fog than RGB images.

DSLR camera sensors are made of silicon, which is inherently sensitive to the visible and shortwave IR regions of the EMS between 400 and 1100 nm. The response curve of a silicon sensor is usually measured by recording the output from the sensor for illumination by EMR at a number of different wavelengths. Figure 3.4 shows a typical response curve plot of silicon sensors.

Image has been removed due to copyright restriction.

Figure 3.4. Spectral response curve of a typical silicon sensor (Darmont 2009).

As discussed in Section 2.9, most DSLR cameras use a NIR cut-off filter, a so-called hot-mirror, in front of the sensor to prevent radiation between 700 nm – 1100 nm contaminating the visible (400 nm – 700 nm) image. However, the camera's spectrum can be easily modified by removing the cut-off filter. Modifying the camera and enabling it to capture NIR light was an essential step toward achieving objectives of this research. The camera modification for this research was conducted by an optical and laser manufacturing company (Maptek Pty Ltd. SA, Adelaide). The modification involved removing the IR filter and replacing it with neutral glass which made it possible to take advantage of the full EMS region of the silicon sensor and enabled the desired EMR wavelengths to pass through the lens using screw-in optical filters in front of the camera lens. The reason for using a neutral glass as a replacement for the hot-mirror filter was to avoid altering the lens focal length. This modification (Figure 3.5) can be commonly done for any DSLR camera by certified technicians at a reasonably low cost.

Image has been removed due to copyright restriction.

Figure 3.5. Removing the hot-mirror filter from a DSLR camera sensor (Kolarivision 2017).

With the DSLR camera modified to full spectra (200 nm – 1100 nm, i.e., parts of the ultra-violet, visible and NIR spectra), external screw-in optical filters can be used to selectively filter UV, visible and SWIR radiation to capture required wavelengths. Before discussing the methodology used in external filter design, the internal components of a typical consumer-grade digital camera are illustrated at Figure 3.6.

Image has been removed due to copyright restriction.

Figure 3.6. Components of a digital camera sensor (Golowczynski 2016).

The items labelled in Figure 3.4 are:

A – Bayer filter array

> Most consumer-grade digital cameras use the Bayer filter array for colour determination.

B – Anti-aliasing filter

> Determines the frequency of light passing through and normally results in minor blurring of the image, though it prevents the aliasing effect or the distortion of pixels. The blurring effect typically is rectified by manufacturers using a sharpening filter.

C – Infrared cut-off filter (hot mirror)

> A cut-off or hot mirror filter is located in between the lens and the anti-aliasing filter that blocks the NIR radiation and only allows visible radiation to pass through to the sensor.

D – Charge pump circuit

Charge pump circuit enables signal amplification at each pixel location and converts charge to voltage.

E – Pixel

When radiation falls onto a camera sensor, pixels measure the amount of light (photons) and release electrons from the silicon, which creates a charge at each photosite.

F – Microlenses

Microlenses increase the sensitivity of the sensor by funnelling light into each pixel.

G – Black pixels

There are some pixels on the sensor that are not exposed by radiation and are typically shielded from light. This allows the camera to measure the amount of dark current during an exposure with no illumination and enables the camera to estimate how much dark current has built up in the active pixels. Therefore, by subtracting this value from them, the amount of noise in the image captured can be reduced.

3.2.3. Optical filter design and spectral response test

There are commercially available optical filters used in photography that allow visible light in a specific region of spectrum to pass through the filter while wavelengths are blocked. A custom-filter was required for this study as it had to transmit blue and green light (450 – 600 nm), filter red and some portion of the IR (600 – 950 nm) and pass anything > 950 nm. This filter was custom made for this research project by Wavelength-Tech (Wavelength Opto-Electronic Pte. Ltd., Singapore) in January 2015 and took six months to build as a separate production line had to be developed by

Wavelength-Tech with the result that the filter was almost ten times more expensive than a typical optical filter. The custom-made filter was delivered in July 2015 and a series of spectral analyses using a FieldSpec4® Hi-Res ASD was conducted to validate its spectral response. Table 3.4 shows the technical specification of this spectrometer. For these tests, a white panel and nine other different materials (Table 3.5) with various spectral responses were selected and used with and without the custom-designed filter to measure their spectral signature. Spectral response curves from this experiment compared against each other to verify the spectral response of the filter. Chapter 5 will discuss these experiments and the results in more details.

Table 3.4 FieldSpec4® Hi-Res ASD technical specification

Wavelength	350 – 2500 nm
Resolution	3 nm @ 700 nm and 8 nm @ 1400/2100 nm
Scanning time	100 milliseconds
Wavelength accuracy	0.5 nm
Channels	2151
VNIR detector	(350-1000 nm) 512 element silicon array
SWIR1 and 2 detectors	(1001-1800 nm) & (1801-2500 nm) Graded Index InGaAs Photodiode, TE Cooled

Table 3.5. Target materials used for measuring the response curve of the custom-designed spectral filter.

Target name	**Type of material**
White panel with 100% reflectance	polytetraflouroethylene (PTFE) and cintered halon
Brick	Brown clay
Concrete	Grey concrete pavier
Steel	Galvanized iron sheet
Garden Mulch	Milled pine
Green Leaves	Eucalyptus sp.
Marble	Grey Purbeck Marble
Sand	Beach sand
Timber	Cedar construction timber
Tree Bark	*Eucalyptus* sp. bark

3.2.4. Camera response test methodology

Considering the design principles of the filter it was anticipated that it would allow natural colour images to be captured when used with the modified camera. Number of photographs were captured with the modified camera equipped with the custom-designed filter and compared with the photographs captured by a non-modified consumer-grade camera from the same scene. The results were satisfactory, and the camera-and-filter combination produced acceptable colour images compared to a non-modified DSLR camera, even after the visible red has been blocked and replaced with NIR radiation between 950 nm – 1100 nm.

In addition to visual comparisons between photographs, further tests were carried out with the FieldSpec4® Hi-Res ASD spectrometer in a laboratory environment under controlled lighting conditions using homogenous black, grey and white cards (Figure 3.7) with uniform reflectance. These cards have very low, medium and high light reflectance factors that allow the full reflectance characteristics of the camera sensor to be investigated.

Image has been removed due to copyright restriction.

Figure 3.7. Black, white and grey targets used for studying the reflectance characteristics of the camera (Courtesy of Mikonava.com).

Images collected from these three targets were analysed in Photoshop CC2015 to extract their digital numbers (DN) and were compared to the corresponding DN values obtained using the FieldSpec4® Hi-Res ASD spectrometer from the same targets using a bivariate linear regression model. Since the camera consists of three bands each with a 100 nm range (400 nm – 500 nm, 500 nm – 600 nm, 600 nm – 700 nm), the FieldSpec4® Hi-Res ASD output were statistically standardized to 1 nm intervals to sample every 100 readings to make the comparison with the corresponding bands of the camera (*cf*. Section 6.2.1).

3.3. Data collection instruments

In previous sections of this chapter, the methods used to design a custom spectral filter and modify a DSLR camera were introduced. In this section the data collection methods, materials, hardware and software tools are discussed. As discussed in Section 3.2.1 an archive multi-sensor data acquired over a bushfire were collected from ARA. These were used for initial analyses and hypothesis validation. To study and analyse imagery from the combination of camera-and-filter three datasets were collected (Table 3.6):

- The first was collected by taking hand-held photographs from a small burn-off area on October 2015.

- A second set was gathered by collecting airborne data over a prescribed burn on November 2016. Controlled burning or burning-off is a common practice on Australian farms for disposing of agriculture and forestry waste or reducing the bushfire hazard and generates substantial amount of smoke. There are stringent safety regulations in Australia for controlled burns, the area must be cleared for four meters and a person must attend all times with enough water available to readily extinguish the fire (CFS n.d.).

- A new series of data were collected from a large prescribed burn area on March 2018 in Belair National Park on the fringes of South Australia (SA) (Figure 3.8). The prescribed burn carried out by Department of Environment and Water (DEW) as part of the Mount Lofty Fire Cooperative Prescribed Burn Program and affected about 7 hectares of the national park. The delivery of the prescribed burning program in the Mount Lofty Ranges is organized by the Mount Lofty Ranges Fire Cooperative in collaboration with representative and volunteers from Country Fire Service (CFS), DEW, Forestry SA and SA Water. The aim of this burn was to minimize potential bushfire fuels in the area to protect communities and also for ecological reasons such as regeneration of plant species. Entire prescribed burn operation took about 8 hours with significant smoke column developed during the burn which was visible in nearby areas several days after that.

Table 3.6 summarizes the data collection details with exact location.

Table 3.6. Data collection methods, sensors and details of burns.

Camera Type and Model	Spectral Filter	Geographic coordinates	Burn type and materials	Date

			of the test area		
Archive data collection	AISA EAGLE hyper spectral camera, FLAIR A615 and CANON EOS 1D (c.f. section 3.2.1)	NA	-34.7171, 138.8311	Natural Bushfire	13 November 2013
Ground data collection	Modified Sony DSLR RX1 400-1100 nm, 6000*4000 pixel, 35mm-focal length lens	Custom-designed filter	-34.7667, 138.7703	Agriculture and forestry waste disposal	26 October 2015
Aerial data collection	Modified Canon DSLR EOS 6D, 400-1100 nm, 5472*3648 pixel, 50mm focal length lens	Custom-designed filter	-35.1051, 138.7867	Prescribed burn	30 November 2016
Ground data collection	Modified Canon EOS 6D 1100 nm, 400-1100 nm, 5472*3648 pixel, 50mm focal length lens	Custom-designed filter	-34.7667, 138.7703	Agriculture and forestry waste disposal	18 March 2018

Figure 3.8. Safety briefing before starting control burn (top image) and collecting ground-based photos from burn area (bottom image) in Belair National Park, South Australia 18 March 2018.

For the aerial data collection, the camera-and-filter combination was mounted in an underwing pod of one of the ECO-Dimona aircraft owned by ARA. The pilot on this flight was my co-supervisor Assoc. Prof. Jörg Hacker. I accompanied him in the second seat (Figure 3.9) and aircraft flight altitude was 600 m AGL.

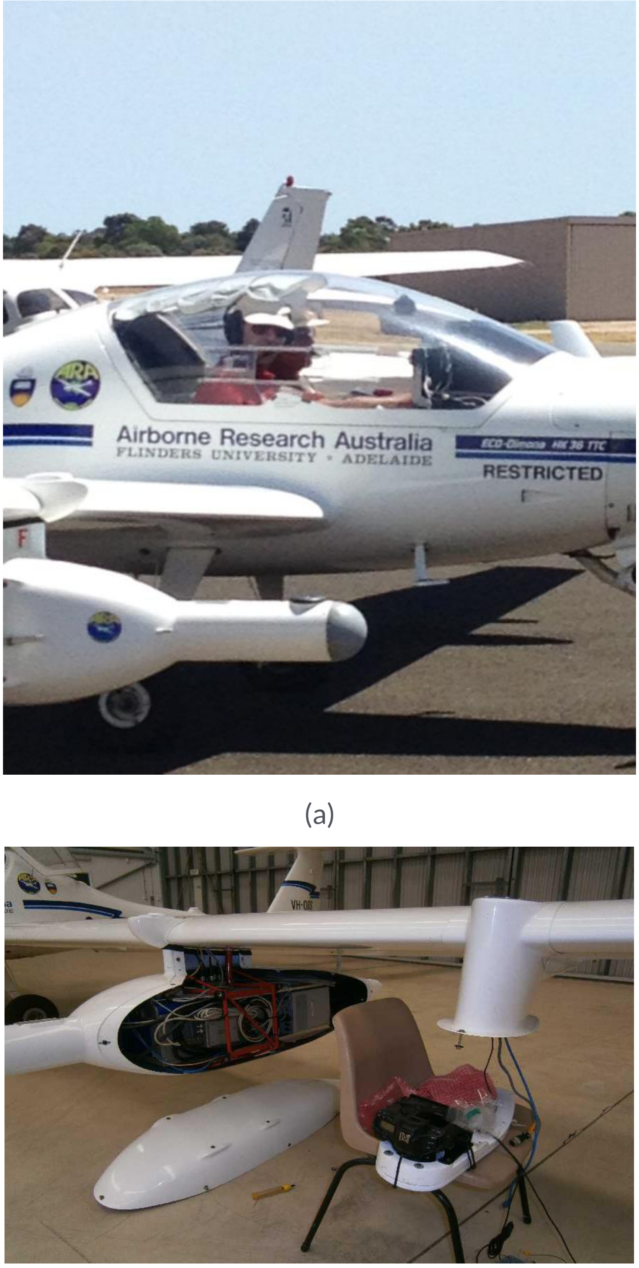

(a)

(b)

Figure 3.9.(a) The ECO-Dimona aircraft before take-off for aerial data collection equipped with the proposed modified camera and custom-designed filter, (b) The camera setup in an underwing pod.

3.4. Data analysis and image processing methods

To address the issue of reduced image visibility and clarity under hazy conditions several haze and atmospheric correction methods have been introduced over the past two decades (*cf.* Sections 2.7 – 2.8). These methods are based on the principle of dark object subtraction in which the darkest pixels in the image are identified and spatially homogeneous haze is reduced by subtracting a constant value corresponding to the dark pixels identified This technique has been optimized by later researchers.

In this research, a new method for removing the smoke effect in the photos captured using custom-designed filter and camera system has been developed (Figure 3.10).

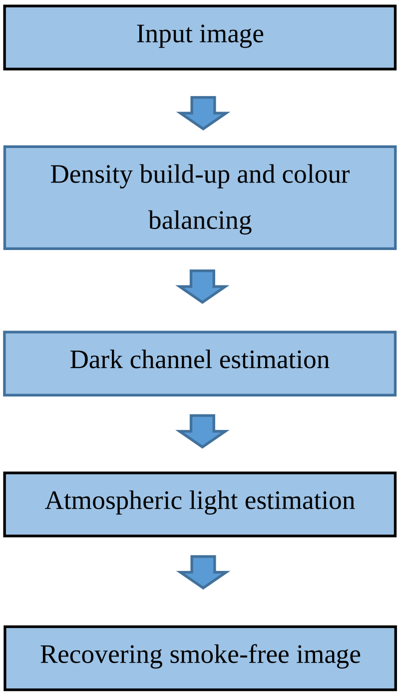

Figure 3.10. Image processing steps for minimizing the smoke effect.

As illustrated in Figure 3.10, the technique first builds up the image density for the visible blue and green channels using the NIR channel and then implements the atmospheric correction based on an improved dark object subtraction method in which very low intensity pixels in local patches across the image are identified. In an image covered by smoke, the dark pixels provide an estimation of the smoke transmission and modelling. This allows a high-quality smoke-free or a minimal smoke image to be recovered. Algorithm development and its implementation was done in C-Sharp (Microsoft Corporation, US. 2015). Chapter 7 will discuss this in detail with experiments conducted and the results acheived.

3.5. Chapter Summary

In this chapter, the framework of this research was introduced; the methods for data collection and analysis were explained and the instruments and software utilized were discussed. Initial research design was based on analysing evidences to confirm feasibility of the research objectives. This was conducted by examining an archive of multi-sensor imagery from a bushfire to simulate and study light scattering effects on the visibility at specific wavelengths. DNs of selected regions covered by smoke in archived imagery were further analysed with image processing software to validate the main hypothesis of this research.

Although the camera modification made is a known modification that has been widely been implemented in variety of applications, this was a necessary component of this research therefore its modification methods are briefly discussed. After camera modification, the specifications of a custom-filter to selectively transmit specific regions of EMS to the camera sensor was discussed, and the methods and materials used for analysing camera and filter spectral responses were further elaborated.

For this research, data collection had to be conducted in bushfire or similar situations where there was smoke in atmosphere. Given the fact that there are highly restricted fire ban seasons in South Australia, organizing an experiment in the open to generate smoke from a controlled fire was logistically complicated. Therefore, the research capitalised on a natural bushfire in November 2016 that I was able to overfly using one of ARA's research aircraft to collect some aerial data using the modified camera and filter combination. In addition, collection of ground photography of a controlled burn area in natural woodland vegetation was organized with the state CFS as part of the Mount Lofty Fire Cooperative Prescribed Burn Program to collect data from the controlled burn in Belair National Park early in 2018.

Finally, data analysis and the workflow for designing a smoke penetration algorithm (SPA) were discussed. The next chapter will examine how the archive data collected in 2013 were used to validate the research objectives.

Chapter 4

Hypothesis Validation

4. Hypothesis Validation

4.1. Introduction

This chapter attempts to examine and validate the main hypothesis of this research which emanates from the first research question. As discussed in Section 3.2.1, three types of archive airborne data were accessed and post-processed for this purpose. These data were collected simultaneously over a bushfire using an AISA EAGLE hyper-spectral push-broom scanner, a FLIR A615 TIR camera and a Canon EOS1D consumer-grade DSLR camera.

The AISA EAGLE data were acquired between 400 nm and 970 nm in 244 narrow (2.3 nm) spectral bands and were a vital component in simulating light scattering effect at those wavelengths. The wavelength range of this sensor is very close to that of a typical consumer-grade DSLR camera but with higher spectral sensitivity. In addition, with a combination of bands from the AISA EAGLE imagery it was possible to form a colour composite image and study the visual appearance of the resulting image. In this chapter data processing and analysing details used for each of hyperspectral, TIR and DSLR archive imagery are discussed.

4.2. Hyperspectral data pre-processing

Figure 4.1 shows how an AISA EAGLE hyperspectral camera scans the ground across flight path with its 1024-pixel spectrograph each with 244 bands and 2.3 nm spectral sampling. Geo-referencing and radiometric calibration need to be applied to pushbroom hyperspectral imagery to prepare them for further analysis. In airborne pushbroom line scanning sensors the image is built line by line using a linear array of CCD detectors perpendicular to the flight line as aircraft moves forward. Every pixel of a given line has its own position and orientation in sensor-space and must be transformed to the object space by geo-referencing. Geo-referencing of pushbroom imagery is more complicated than for frame-based imagery as it requires instantaneous attitude and accurate position at each line of captured imagery. Therefore, a precise GPS/IMU system is required onboard the aircraft to determine these parameters. GPS and IMU systems must be fully integrated with the hyperspectral sensor with precisely synchronized timing for each scanned line. Figure 4.2 shows the procedures required for post-processing and preparing the pushbroom hyperspectral imagery.

Image has been removed due to copyright restriction.

Figure 4.1. ASIA EAGLE hyperspectral camera scans the ground objects across direction of flight using a spectrograph with 1024 pixels and 244 band per each pixel from 400 nm (Blue) to 970 nm (NIR). (Geoinformatics 2018)

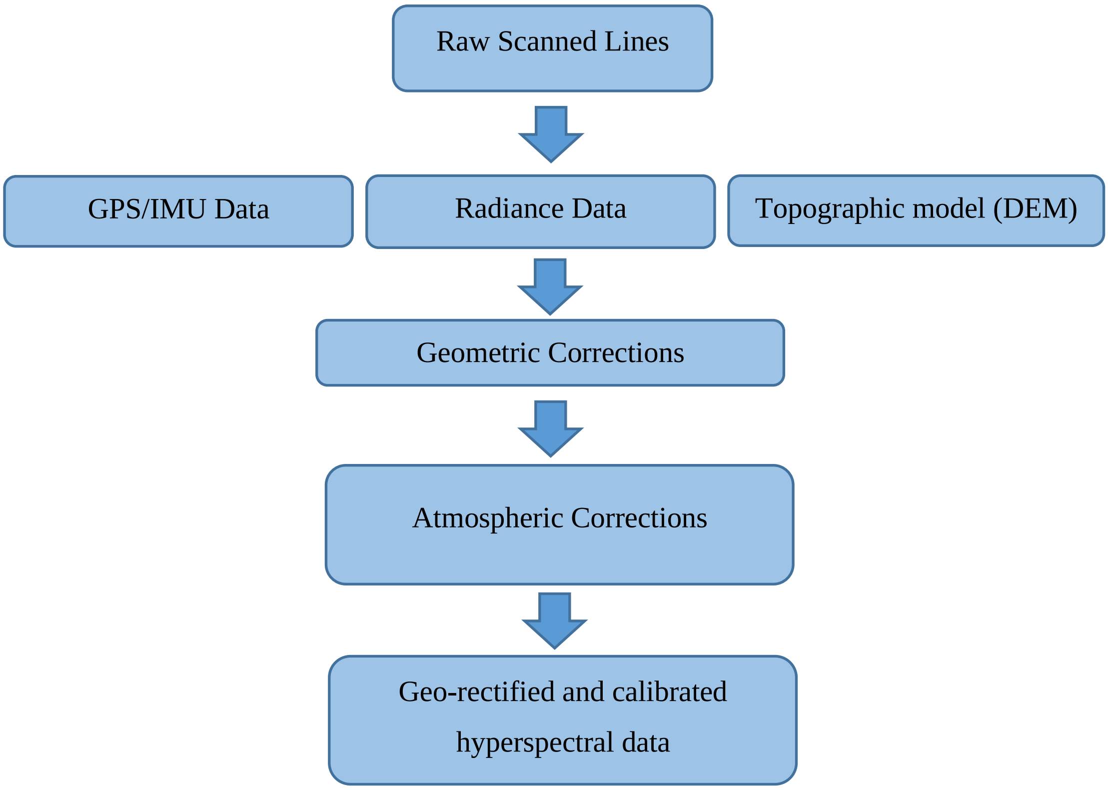

Figure 4.2. ASIA EAGLE hyperspectral data processing workflow.

The raw data from AISA EAGLE are typically stored as a pair of ENVI BIL format including '. raw' and '.hdr' files (Sensors 2018). The radiometric calibration normalizes the data to remove internal electrical system noise (Oppelt and Mauser 2007) and transforms the DN numbers to physical radiometric values or radiance (Warren, Taylor, Grant and Shutler 2014).

Accurate position and orientation data was captured by a RT4000 inertial and dual-GPS navigation system with 250HZ position and attitude output supplied by Oxford Technical Solutions, Oxford, UK. The RT4000 GPS/IMU system was connected to the AISA Eagle camera to time-tag the beginning of each line acquisition with GPS time. These raw GPS data were post-processed using a PPP (Precise Point Positioning) technique in NAVGRAPH software (Oxford Technical Solutions, Oxford, UK). This technique removes GNSS system errors and provides sub centimetre positioning accuracy. Any minor angular error in accurately aligning the GPS/INS system and the hyperspectral camera, which is known as boresight miss-alignment, could cause a significant error depending on the distance between the camera and the ground. The RT4000 GPS/IMU system was precisely aligned and calibrated with the AISA EAGLE camera by ARA engineers.

Using accurate position and orientation data every individual scanned line was geo-referenced and geo-rectified utilizing a 1" global digital elevation model (DEM) in ENVI software. DEM is not essential as ENVI software can use an ellipsoid surface for geo-rectification, but this would cause a large error in mountainous and hilly terrain without accurately projecting the image pixels to the ground surface. Using the dark subtraction method (Chavez 1988), atmospheric correction was applied in ENVI software to remove the effects of atmospheric scattering before producing the geo-referenced and calibrated hyperspectral data (Figure 4.3).

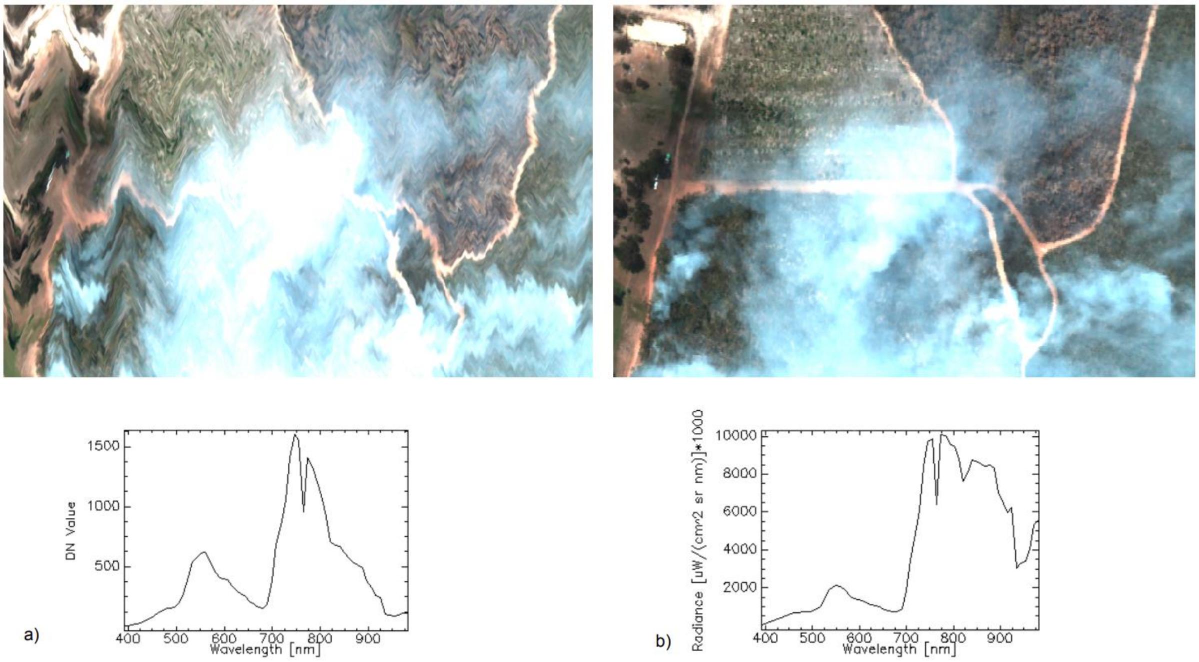

Figure 4.3. (a) Data collected by AISA EAGLE data and a spectral response curve before geo-referencing and radiometric correction, (b) Image and spectral reflectance curve after applying radiometric correction and geo-referencing. After applying corrections, the spectral reflectance at λ>750 nm is improved, this indicates the effectiveness of applying atmospheric corrections in reducing smoke scattering effect.

Figure 4.4 shows the hyperspectral orthomosaic as a three-band true colour RGB composite image (400 nm – 700 nm). This image shows how smoke plumes from bushfire obscure scene visibility.

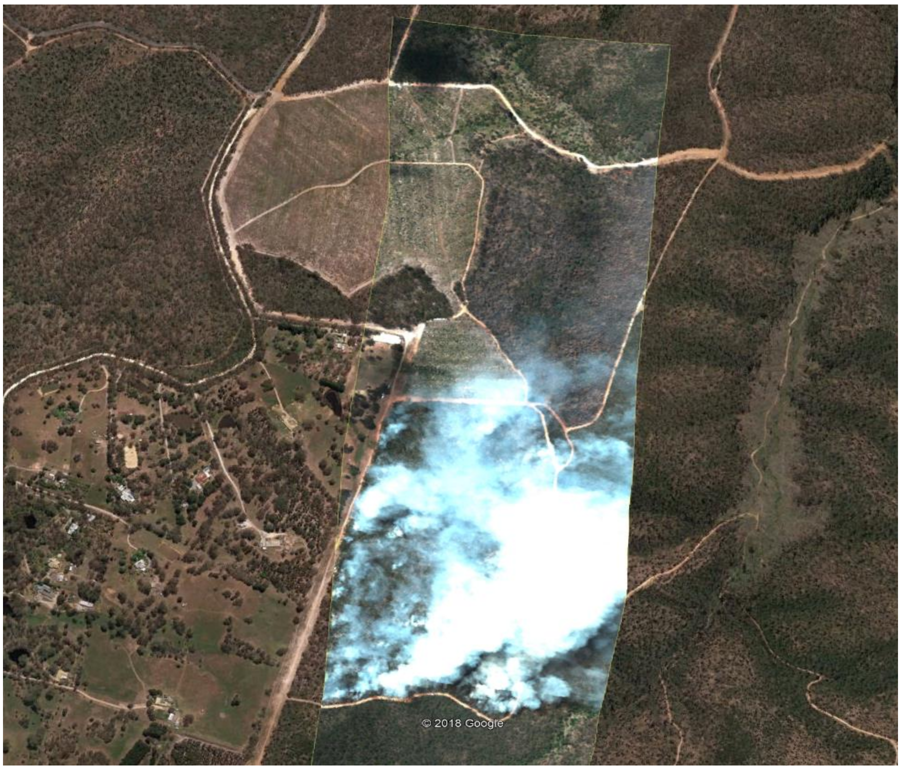

Figure 4.4. Orthorectified AISA EAGLE hyperspectral data produced as a true colour composite image and overlaid on Google Earth imagery. Smoke plumes are visible and obscure the ground view.

4.3. Thermal and DSLR image processing:

Collected TIR imagery using a FLIR A615 thermal sensor with 14-bit raw DNs, which represent at-sensor radiance, were processed with ENVI image processing software and stored as 16-bit ENVI single band files. A set of quick overview images in JPG format were created simultaneously to visually check of image quality. Since the DNs do not cover the full 14-bit dynamic range, a contrast stretch was applied to the TIR imagery. A linear contrast stretch was applied based on maximum and minimum threshold of the histogram to cover full dynamic range of the scene. A custom developed TIR image processing script by ARA was used in ENVI to create a file containing the TIR frame number and the frame time in seconds to three decimal places. It uses the lens and camera model file with GPS/IMU navigation data as well as a DEM model to geo-rectify and mosaic the TIR imagery (Figure 4.5). After mosaicking, DN values were converted to absolute temperatures in ENVI software based on the empirical line correction method (Smith and Milton 1999).

Figure 4.5. Orthorectified TIR imagery from a bushfire with transparent smoke plumes, overlaid on GoogleEarth. It illustrates heat distribution as a grayscale image where black to white colours with various levels of grey in between represents the temperature difference. In this image bright pixels show the hot spots or flaming fire.

Thermal imagery represents the level of radiated heat from objects and as a result the distinction between fine ground features is challenging. Due to the small sensor size a of a thermal camera and relatively small ground coverage of a single image, a large number of overlapping photographs need to be collected and mosaicked to cover a large area. A typical workflow for image mosaicking starts with aerial triangulation and pixel matching between overlapping photographs, which is required to establish geometrical relationships between multiple imagery. A fully automatic pixel matching process extracts common features and key points to match images.

Since none of the thermal, DSLR and hyperspectral camera sensors that had been used to acquire the images in the archived dataset were mounted on a stabilized camera mount, forward and sideways motion of the aircraft at the time of exposure had some impact on the pixel quality and image geometry. The resulting motion blur effect can be calculated using the equation 4.1 (Chabok 2013).

$$\mathrm{b} = \frac{v \times t \times f}{\mathrm{c} \times \mathrm{h}} \times 1000 \qquad \text{Equation 4.1}$$

where

l = motion size in pixel
v = ground speed in km/h at the time of exposure
t = exposing time in seconds
f = focal length in mm
h = flying height above ground in meter
c = camera sensor pixel size in micron

This values of b for the thermal and DSLR imagery are therefore calculated using equation 4.2 as follows:

$$\mathrm{b\_thermal} = \frac{180 \times 0.01 \times 24.5}{600 \times 17} \times 1000 = 4.3\, pixels$$

$$\mathrm{b\_DSLR} = \frac{180 \times 0.001 \times 50}{600 \times 5} \times 1000 = 3\, pixels$$

Those numbers show that during the exact exposure time aircraft motion will have caused a 4.3-pixel blur for thermal imagery and a 3-pixel blur for the DSLR camera image. Image quality will be degraded accordingly. This motion also creates a geometrical instability over the entire frame (Figure 4.6) which is elaborated in more detail in Appendix 3.

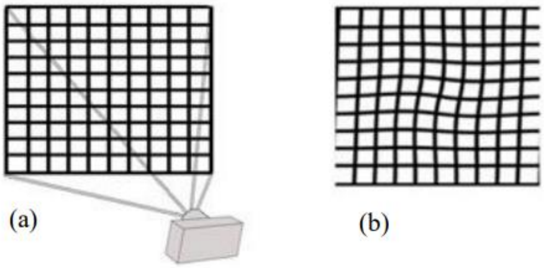

Figure 4.6. (a) shows image pixels as regular grid without any camera motion and (b) illustrates how pixels can be randomly distorted due to the camera motion (Chabok 2013).

These effects degrade the spatial resolution of any imagery acquired and also influence the quality of pixel matching and image mosaicking which is more sensible for thermal imagery than DSLR. Images from the DSLR camera were processed using PhotoScan software and key points representing common pixels in overlapping images were extracted. Figure 4.7 shows three overlapping images with extracted key points in blue dots. Areas covered by smoke do not contain any key points as the pixel quality in those areas are greatly degraded.

Figure 4.7. Pixel correlation and key points extraction on three overlapping DSLR camera images captured over a bushfire smoke.

Orthorectification and mosaicking of these images requires a 3D elevation model (DEM) which can be either reconstructed from the same frames or an existing DEM model can be used. In this research, a DEM model was generated using the same image frames in PhotoScan. To generate a DEM model, PhotoScan uses pair-wise depth map reconstruction that computes relative depths for each pixel of an image and generates dense point clouds (Aiger, Mitra & Cohen-Or 2008).

Dense point clouds generated from the images used at previous step included many noises and outliers around smoke area caused by smoke particulates. These data were visualized in 3D in PhotoScan to highlight the noise and artificial objects (Figure 4.8).

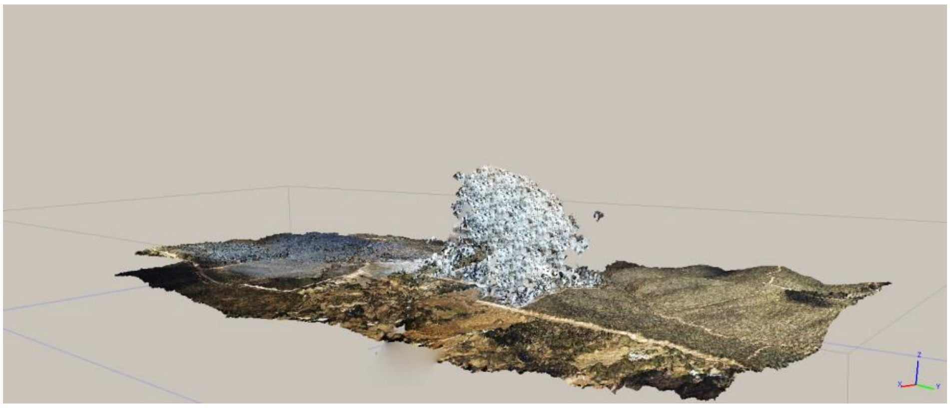

Figure 4.8. Smoke particulates effect on image matching and generating dense point clouds. Grey artificial points on the left and in the centre show noises caused by smoke particulates.

These point clouds used as a basis for DEM generation in PhotoScan for image orthorectification. Final mosaicked image contained a gap as per illustrated in Figure 4.9 because of unsuccessful image matching around smoke area.

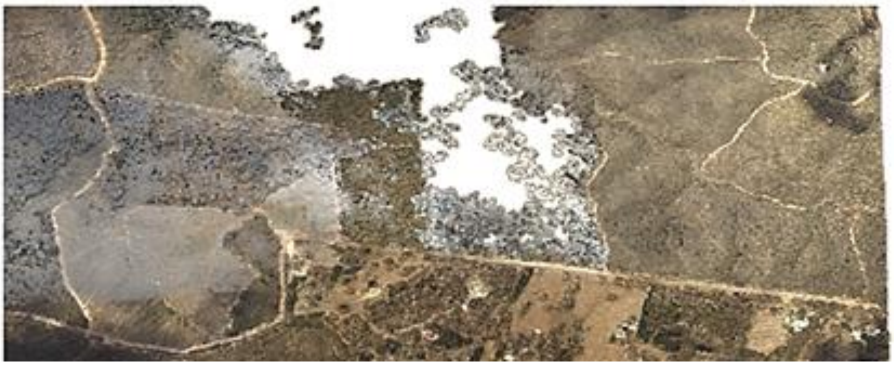

Figure 4.9. Smoke particulates effect on mosaicking DSLR camera imagery which creates a large data gap (grey pixels) in the centre of the image.

4.4. Smoke penetration analysis on hyperspectral imagery

Orthomosaiced hyperspectral data from AISA EAGLE sensor was analysed in ENVI image processing software at each individual wavelength from 400 nm – 970 nm to study the effect of light scattering on image visibility. Figure 4.10 shows an area covered by smoke in hyperspectral imagery at different wavelengths and how image visibility is enhanced with an increase in the wavelength. For illustration purposes only

20 subsets of 244 are displayed in Figure 4.10, however all of the 244 bands were analysed in ENVI software to study smoke visibility effect at different wavelengths. In these images, 24 randomly selected pixels were identified in areas completely covered by smoke, which are marked as red crosses in Figure 4.10. Statistics of the DNs for these points were computed in ENVI for each of the 244 individual bands. Table 4.7 summarises these statistics in terms of minimum and maximum values and means and standard deviations.

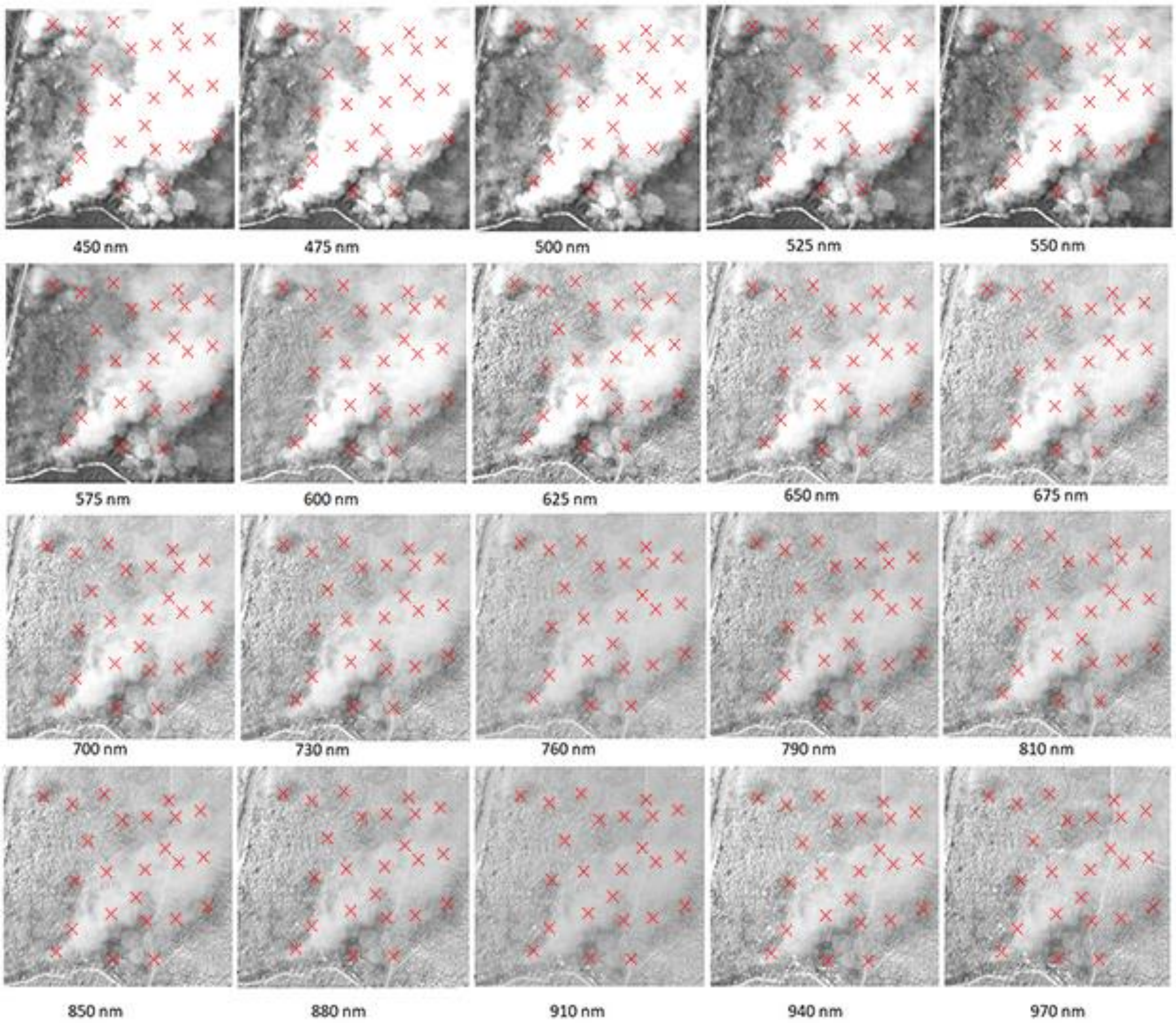

450 nm 475 nm 500 nm 525 nm 550 nm

575 nm 600 nm 625 nm 650 nm 675 nm

700 nm 730 nm 760 nm 790 nm 810 nm

850 nm 880 nm 910 nm 940 nm 970 nm

Figure 4.10 Twenty subsets of AISA EAGLE hyperspectral image between 400 nm to 970 nm. It is clear that image visibility improves as wavelength increases. Red crosses indicate where DNs were extracted for each individual band (see Table 4.7).

The hyperspectral camera data were extremely useful in visualizing light scattering effects at different wavelengths and informed the design of an optical filter to block and transmit specific regions of EMS to meet the objectives of this research. A visual inspection of wavelengths shows that starting from about 750 nm onwards smoke particulates become ‘transparent’ and that this effect is more pronounced above 900 nm. To identify this inflection point the spectral profile of the selected points (*cf.* Table 4.7) were plotted (Figure 4.11).

Table 4.1 Statistical summary of the reflectance values for highlighted pixels in Figure 4.10

Band	Min	Max	Mean	Std Dev
400 – 450 nm	0.0650	0.1136	0.0983	0.0112
450 – 475 nm	0.0983	0.1730	0.1517	0.0159
475 – 500 nm	0.1061	0.1962	0.1709	0.0191
500 – 525 nm	0.1007	0.1895	0.1647	0.0186
525 – 550 nm	0.0986	0.1951	0.1705	0.0200
550 – 575 nm	0.0895	0.1827	0.1608	0.0197
575 – 600 nm	0.0846	0.1777	0.1571	0.0199
600 – 625 nm	0.0727	0.1618	0.1418	0.0191
625 – 650 nm	0.0657	0.1511	0.1298	0.0183
650 – 675 nm	0.0627	0.1449	0.1261	0.0182
675 – 700 nm	0.0606	0.1332	0.1157	0.0160
700 – 730 nm	0.0629	0.1194	0.1064	0.0128
730 – 760 nm	0.0370	0.0627	0.0565	0.0060
760 – 790 nm	0.0792	0.1384	0.1244	0.0137
790 – 810 nm	0.0586	0.1021	0.0896	0.0095
810 – 850 nm	0.0677	0.1145	0.1008	0.0106
850 – 890 nm	0.0697	0.1163	0.1012	0.0103
890 – 910 nm	0.0531	0.0792	0.0709	0.0066
910 – 940 nm	0.0256	0.0372	0.0329	0.0030
940 – 970 nm	0.0614	0.0926	0.0810	0.0074

This analysis was computed using data from the 24 randomly distributed points above smoke-affected region for 244 bands. Table 4.1 shows minimum and maximum reflectance value for the selected points with the mean and standard deviation. The standard deviation decreases as the wavelength increases which indicates lower reflectance at higher wavelengths. To better demonstrate this effect a spectral profile of the selected pixels using ENVI software was generated (Figure 4.11). A lower reflectance shows that smoke has minimal effect on pixel values which only happens at wavelengths beyond 950 nm, i.e., when the smoke is ‘transparent’. Therefore, this wavelength was selected as the lowest infrared wavelength at which EMR would be transmitted in the custom-designed filter to be used in this research (Section 5.2).

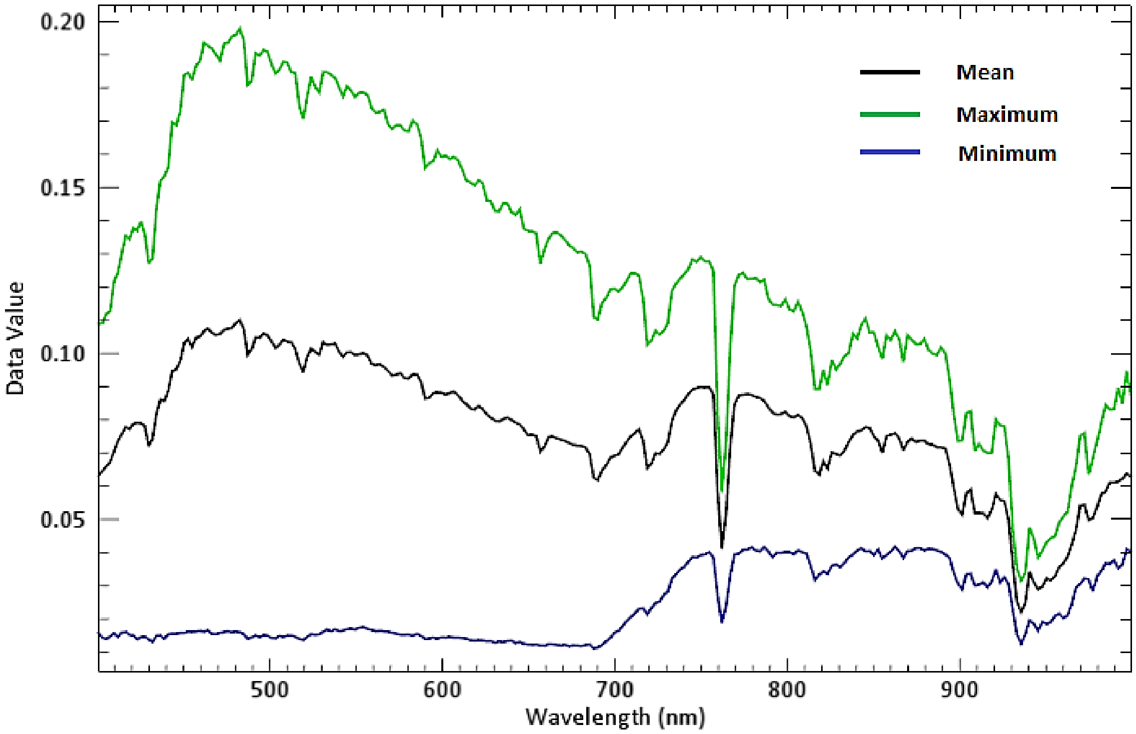

Figure 4.11 Spectral profile of the highlighted pixels in Figure 4.7 from 400 to 970 nm for 244 bands. From 400 to 700 nm there is a high reflection caused by smoke particulates whereas from 700 to 950 nm this reflection decreases and gets minimal beyond 950 nm wavelength.

4.5. Chapter Summary

Multi-sensor airborne data from a bushfire in the ARA image archive, which included multiband hyperspectral, single-band thermal and three-band optical DSLR camera imagery, was explored to study the feasibility of achieving the objectives of this research and also to validate the main hypothesis.

The post-processing steps were undertaken to prepare these sensor data for this analysis were discussed and it was concluded that although thermal imagery penetrates smoke, there are some issues that need to be addressed. First, for large areas many images would need to be collected to create a uniform mosaic due to the small ground coverage of a single thermal image. Second, monochromatic pixels coupled with pixel blur caused by aircraft motion can affect image matching techniques and can degrade the spatial resolution. For DSLR camera imagery, the presence of smoke caused a data gap in image mosaicking with was accompanied by artificially created noise.

The hyperspectral pushbroom scanner image did not have any of these issues because of its integrated onboard direct geo-referencing which created a large mosaic for the entire bushfire area after image orthorectification and radiometric correction. The geo-rectified image from the hyperspectral sensor was used to analyse smoke transparency at wavelengths from 400 nm to 970 nm. A statistical summary of spectral reflectance values for distributed pixels spread across a selected region of the hyperspectral image, that was completely covered by smoke, was computed for all 244 bands. By comparing the standard deviation of the reflectance values, significant improvements in image visibility and low reflectance were found at wavelengths > 950 nm.

From these analysis from ARA archive data it can be posited that using a DSLR camera, which also has a silicon-based sensor with 400 – 1100 nm wavelength sensitivity, it may be possible to penetrate smoke as was the case with these hyperspectral images. This analysis also validates the main hypothesis. However, to accomplish this modification to a consumer grade DSLR is required and a custom-filter has to be designed to selectively transmit IR light above 950 nm in one of the selected bands of the DSLR camera sensor. The next chapter will discuss design criteria for this and how a specific band was selected to collect IR light, along with the results of the performance tests of the custom-designed filter.

Chapter 5

Optical Filter Design and Evaluation

5. Optical Filter Design

5.1. Introduction

In 1802, Thomas Young suggested that colour vision is a result of activities of three distinct receptors in the brain and that the eye contained different wavelength-sensitive cells. Helmholtz developed Young's hypothesis and showed that the cone receptors of the eye were either short wavelength (blue), medium wavelength (green) or long wavelength (red). He additionally suggested that the quality of the detected signals by the receptor cells influences the brain in colour interpretation. Helmholtz found that people with ordinary colour vision require three wavelengths of light to see serious of colours. He found that people could not recognize the colours if they only used two wavelengths (Goldstein 2009).

Based on Helmholtz finding, at least three wavelengths of light have to be transmitted directly or via an optical filter to the camera sensor, so it can form a recognizable colour image for human eyes. A typical DSLR camera image sensor contains an array of photosensitive components that form detector arrays (*cf.* E in Figure 3.6). These arrays collect light (photons) from a scene and convert them into an electrical signal, which is digitized and processed. Each pixel must contain three primary colours to generate a colour image. Bayer (1970) showed that a colour filter array (CFA) pattern allows the formation of all the colours of a scene captured by a single photograph. This CFA pattern (*cf.* A in Figure 3.6) is known as a ‘Bayer pattern’ and is used in most consumer-grade digital camera systems. After an image has been captured, each pixel only contains single colour information. However, information for all three primary colours is needed to construct a colour image. The missing information is interpolated using the information collected by the neighbouring pixels. The colour interpolation process constructs a natural colour image, the quality of which depends on the spectral characteristics of the optics, quantum efficiencies of the sensor and filters (OnSemi 2015). The quality of the final image depends on the interpolation algorithm used.

Because the blue and green bands in a typical CMOS sensor can potentially sense NIR radiation, once the camera is modified to capture full spectra, the wide dynamic range of NIR (700 nm – 1100 nm) will strongly contaminate the blue, green and red channels. Figure 5.1 shows how blue, green and red channels are sensitive to NIR radiation with varying spectral sensitivity, this will cause a red appearance in the image captured. Figure 5.2 shows two images captured by a non-modified and a modified consumer-grade DSLR camera and how the resulting image after modification is affected by NIR radiation. To avoid this effect in this research, a custom optical filter was designed to only allow radiation of λ >950 nm to pass through it. This NIR range (950 nm – 1100 nm) has a very low Quantum Efficiency (QE). The fraction of photon flux that contributes to the photocurrent arrays in a camera sensor is known as QE (Fowler et. al 1999). This low QE minimizes the effect of NIR light in the blue and green bands. Therefore, the custom-designed filter only allows visible blue and green light to pass plus NIR radiation > 950 nm. This allows the NIR radiation > 950 nm to be recorded in the red channel of the CFA without affecting the blue and green channels. As a result image captured will look more natural when viewed by the human eye.

Image has been removed due to copyright restriction.

Figure 5.1. Spectral response and quantum efficiency of a typical silicon-based sensor with CFA filter (OnSemi 2015).

Figure 5.2. Images from a non-modified consumer-grade DSLR camera image on the left, and a modified camera image without any external filter on the right. The second image shows how NIR radiation contaminates the blue, green and red channels in the CFA.

5.2. Design criteria

Optical filters are devices that can transmit selected radiation in a specific range of wavelengths while blocking all other wavelengths (Madsen and Zhao 1999). In designing the custom optical filter for this research, in addition to transmitting at least three wavelengths of EMR as argued by Helmholtz and discussed in previous section, two more conditions were considered:

- to capture NIR radiation in the same digital image as visible light; and
- the preservation of natural colours in resulting photographs.

They are commonly used in photography and many other types of optical instruments to restrict the transmission of EMR to particular wavelengths of interest. The frequency responses of the optical filters describe their characteristics and specify how the magnitude of each frequency component of incident light is modified by the filter (Madsen and Zhao 1999). The actual blocking provided by a filter is determined not only by the part of the EMS it is designed for, but also by any physical imperfections of the filter. Surface and mounting imperfections can cause scattered light to pass through the filter due to a high transmission region of spectrum via unblocked paths near the edges or mounting (Prabhat n.d.). Therefore, it is important to evaluate the blocking performance of an optical filter, whether an off-the-shelf standard or custom-designed; as is the case in this research.

Figure 5.3 shows the spectral transmission curve of the custom-designed filter used in this research, which allows EMR between 400 and 600 nm (visible blue and green) to pass, blocks radiation in the range 600 nm – 950 nm and the allow radiation at λ > 950 nm to pass. This custom-designed filter used with a modified camera to capture series of photographs to verify if preserver original colours. A non-modified camera was used to capture photographs from the same scenes as a reference (Figure 5.4).

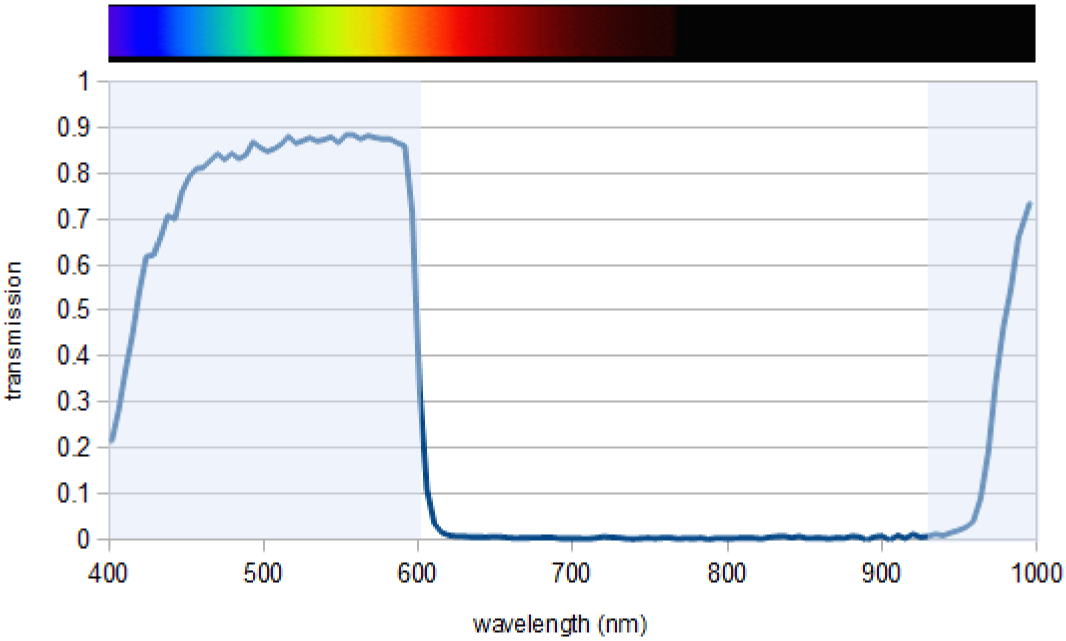

Figure 5.3.Spectral transmission curve of the custom-designed optical filter used in this research derived from spectrometry measurements.

Results of this comparison showed that images captured with the combination of custom-filter and modified camera produce almost the same quality colour images as a non-modified DSLR camera. The difference is a slight colour loss in the yellow to red parts of the EMS caused by replacing the red band of the camera with the a NIR (950 – 1100 nm) band. However, this slight colour loss does not create any major perception changes nor visual image interpolation issues for natural scenes.

In addition, the combination of the custom-designed filter and modified camera can potentially capture less scattered light in the red band of the CFA because of Rayleigh scattering (Figure 5.5).

Figure 5.4. The left-hand images in each pair were captured by a non-modified camera, while those to the right were captured by the modified consumer-grade DSLR camera with the custom-designed filter.

Image has been removed due to copyright restriction.

Figure 5.5. Rayleigh-type scattering curve, for particle sizes <λ/10 scattering is inversely proportional to λ4 (Bucholtz 1995).

5.3. Measuring the Spectral Response of the Optical Filter

The performance of the custom-designed filter was studied using a spectrometer as a laboratory reference instrument to test the response of the filter for a range of materials (*cf.* Section 3.2.3). Spectrometers measure spectral radiance or irradiance for various spectral ranges and consists of four basic sections (Bentham 1997):

1) the input optics which collect radiation at a given FOV and transmit it to a monochromator;
2) a monochromator that divides the radiation into wavelength ranges;
3) a detector that measures the radiation in each wavelength range; and
4) a control and storage system to define the data and logs it.

High specification spectrometers are frequently used to measure the transmission properties of optical filters.

The FieldSpec4® Hi-Res ASD spectrometer used in this research is based on a bare fibre bundle, with optional collecting optics, which has a variable FOV. It measures either reflected or emitted irradiance from the objects located in the FOV. In this research, the materials in the FOV were illuminated and reflected light was measured. The collected spectral power is measured by three linear detector arrays in three different spectral regions (400 nm – 1000 nm, 1001 nm – 1800 nm and 1801 nm – 2500 nm) with spectral sampling at 3, 5 and 8 nm respectively. The device is calibrated so that it converts the read-out signal in digital numbers (DN with 16-bit binary digit) to spectral irradiance.

5.3.1. Laboratory setup and spectral analysis of the custom-designed filter

The following steps show the laboratory setup used to verify the spectral response of the optical filter with the FieldSpec4® Hi-Res ASD spectrometer:

1) An ASD Illuminator halogen-based 12v, 50W lamp, with a correlated colour temperature of 3000 $^{\circ}K$ (equivalent to 11000 candle power) was used as the light source.
2) The lamp beam angle was set to 12°.
3) The distance from the light source to the target sample was set at 66 cm.
4) The incident angle was set to 65 °.
5) The distance from the tip of the fibre optic cable to the target was set at 15cm and the FOV was 22 °.

The FieldSpec4® Hi-Res ASD was used to measure the frequency response of the custom-designed filter and its performance in terms of the passing/blocking band and transmittance of the filter. This type of accurate measurement is critical in understanding the response from deep blocking to high transmission over a very short range of wavelengths, thus leading to steep and deep spectral edges. This filter was designed for a consumer grade digital camera, so the wavelength range of interest is 400 nm to 1100 nm.

To perform spectral analysis of a source, monochromatic light at a wide range of wavelengths is required to create a spectral response or spectral signature of the illuminant. A monochromator is used to sample the wavelengths reflected from the source and produce a monochromatic signal. A monochromator is basically a variable filter that specifically isolates and transmits a particular wavelength or range of wavelengths from the full range of measured light and blocks light that falls outside that wavelength or range of wavelengths. It typically accomplishes this using passage and exit slits, collimating and focus optics, and a wavelength-dispersing component; for example, a diffraction grating or prism.

In modern spectrometers, charge coupled device (CCD) and linear locator arrays have facilitated the improvement and development of fixed grating spectrometers. As the incident radiation hits the individual pixels over the CCD, the intensity of each pixel shows the region of the spectrum that the internal electronics has translated. While photodetectors can be portrayed in a wide range of ways, the most essential differences between them is the material the detector is made from. Si (Silicon) and InGaAs (Indium-Gallium-Arsenic) are the most typical semiconductor materials used in spectrometers. The FieldSpec4® Hi-Res ASD is configured so that it has three separate holographic diffraction gratings with three separate detectors. Each detector is also covered with the appropriate order separation filters to eliminate second and higher order light (BWTek n.d.).

In the spectrometer, the visible and near-infrared (VNIR: 400 nm – 1000 nm) part of the EMS is measured by a 512-channel silicon photodiode array (CCD). Each detector is geometrically aligned to receive radiation within a narrow range (1.4 nm) and converts incident radiation into electrons. This photocurrent is then converted to a voltage, and is continually digitized and processed by a 16-bit analog-to-digital converter. The spectral data obtained is then passed to the controller unit for further analysis (Elvidge et al. 2010). The spectrometer performs the reflectance measurement by calculating the ratio between the DN of the new target surface relative to the DN of the white reference panel. Therefore, all sets of measurements of different reference materials were preceded by measurements of spectrometer white reference panel, which is set as the white reference scan in the system software.

5.3.2. Measuring the filter response

In this research, a range of natural materials commonly found in urban and rural environments (*cf.* Table 3.5) were used to verify the blocking and passing bands of the optical filter.

Figure 5.6 shows the filter performance on the white reference panel. The panel is made of polytetraflouroethylene (PTFE) and cintered halon. Its key characteristics are that it is almost 100% reflective within the 350 nm - 2500 nm range, and that it uniformly scatters light in all directions within this range. Software supplied by FieldSpec4® Hi-Res ASD calculates the ratios for reflectance or transmittance of the material being collected by the spectrometer using the reference panel. The blue line in Figure 5.6 is almost flat at a reflectance value of 1.0, which equates to 100% transmission if we deem air to be a cuvette. The orange curve represents the reflectance across the range of wavelengths using the filter developed for this research. To minimize the effect of light leakage into the fiber optic, i.e., light bypassing, the filter was held close to the fiber optic probe so that it made a very tight contact with the tip (Figure 5.7) and eight measurements for each sample were made. Figures 5.8 – 5.9, that show the percent transmission plotted against wavelength for green leaves and marble, are averages of eight measurements. Percent transmission (%T) is the typical unit used to quantitatively measure rate of optical filters light transmission. It is measured at a particular wavelength and is the percentage of the ratio of transmitted light intensity (I) to incident light intensity (Io):

$$\%T_{\lambda} = I/Io * 100$$

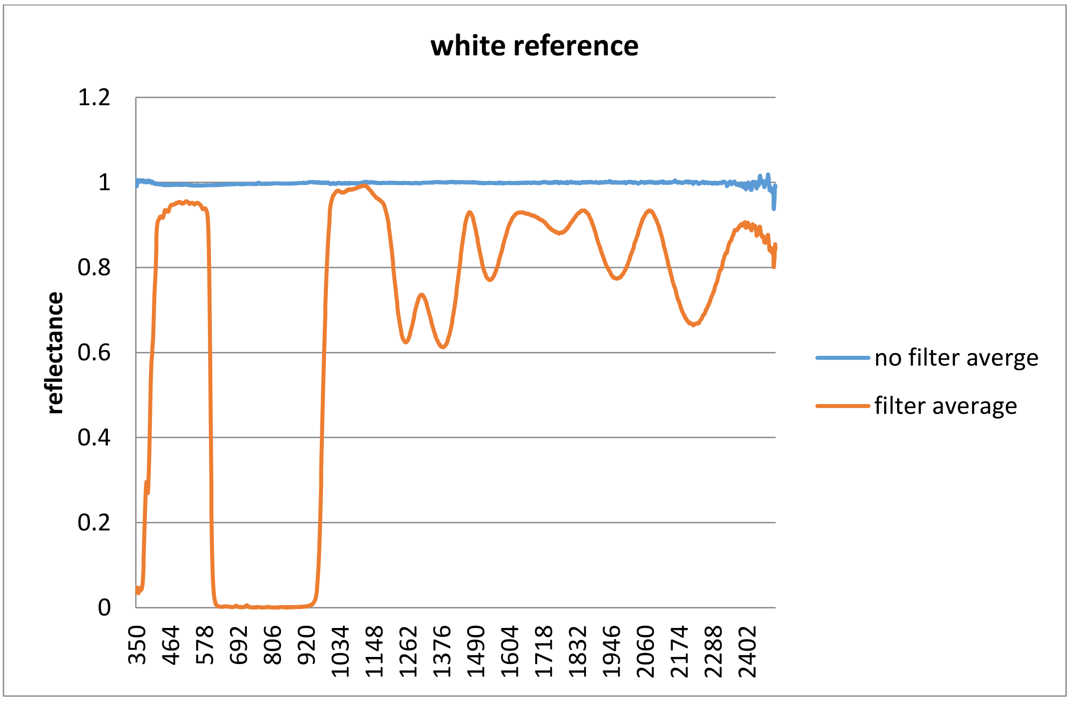

Figure 5.6. The reflectance (transmission percentage) of a white reference panel. Blue and orange lines show the reflectance of a white panel without and with the custom-designed filter respectively, performance dips at 1150-1450nm.

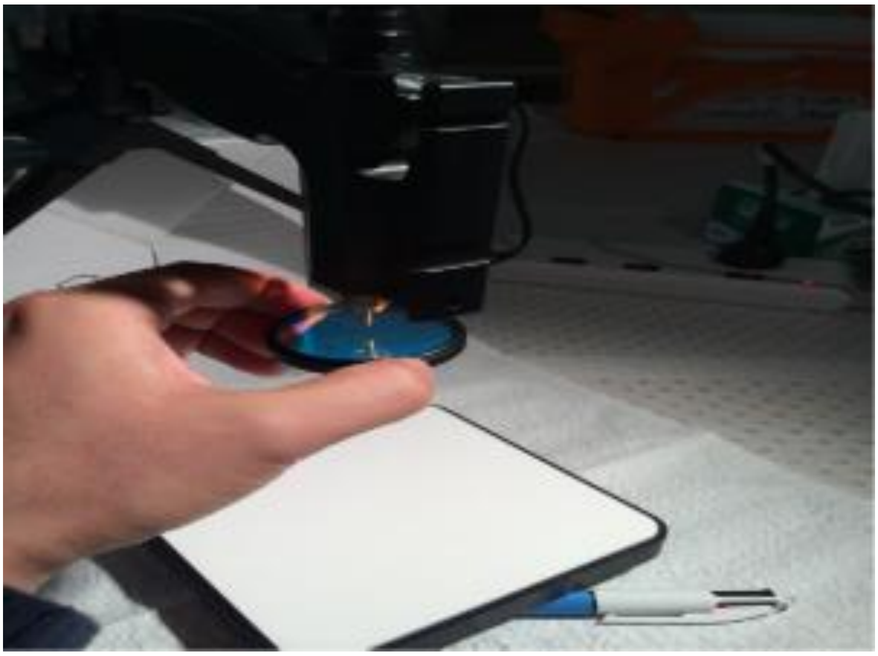

Figure 5.6. Using the probe of the FieldSpec4® Hi-Res ASD spectrometer to measure the specification of the custom-designed filter on a white reference panel.

The filter blocks light from about 600 nm to 950 nm. Reflectance (transmission) starts to decrease dramatically at 584 nm (reflectance = 0.94) (Figure 5.6). By 600 nm the reflectance (transmission) has dropped to 0.51 and by 615 nm it is only 0.016. Between 615 nm and 950 nm nearly all light (reflectance = 0.014) is blocked. Beyond 950 nm reflectance (transmission) increases to 0.51 at 979 nm and 0.95 at 1007 nm. The absorption region at $\lambda = >1200$ nm is not relevant to this research and is not discussed. Figures 5.8 and 5.9 show the reflectance curves for green leaves and marble. The reflectance spectra for the other materials used in this experiment are provided in Appendix 1.

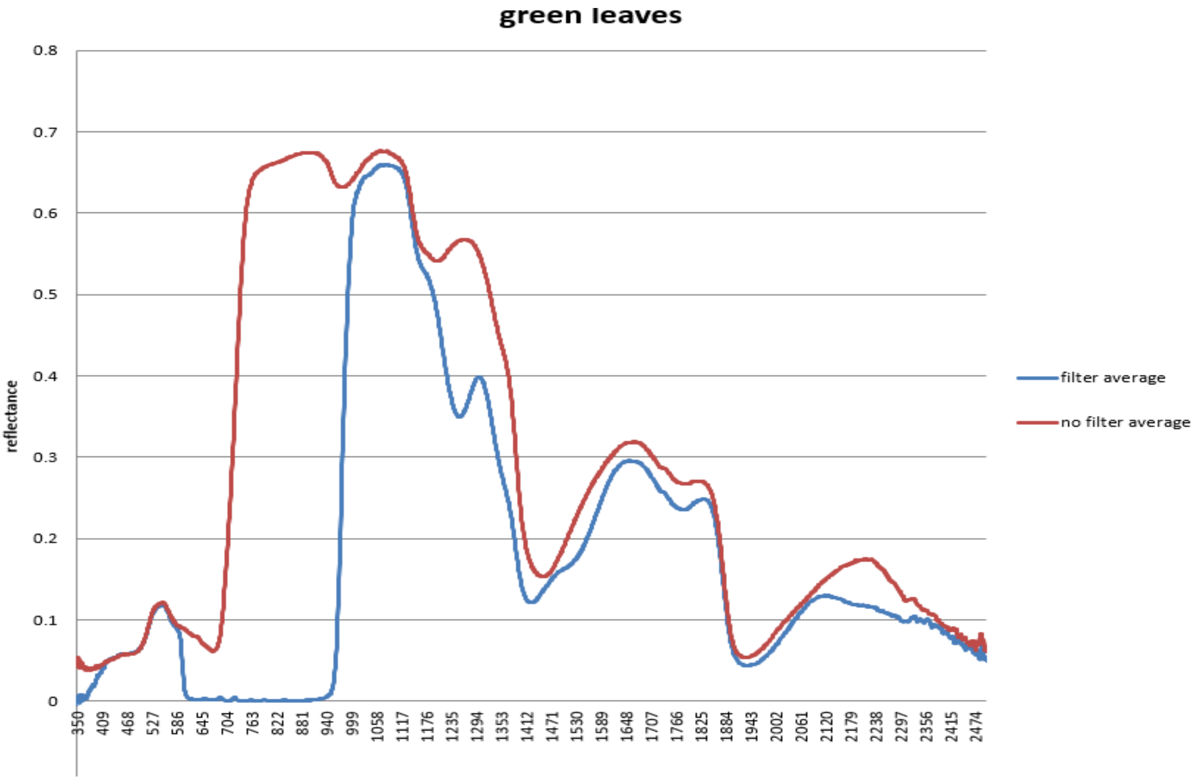

Figure 5.7. Reflectance curve of green leaves with and without the custom-designed filter. Blue colour represents the filter spectral response and how it absorbs the light from 600 – 950 nm wavelength and follows the red curve (green leaves reflectance curve without filter) in other regions of EMS.

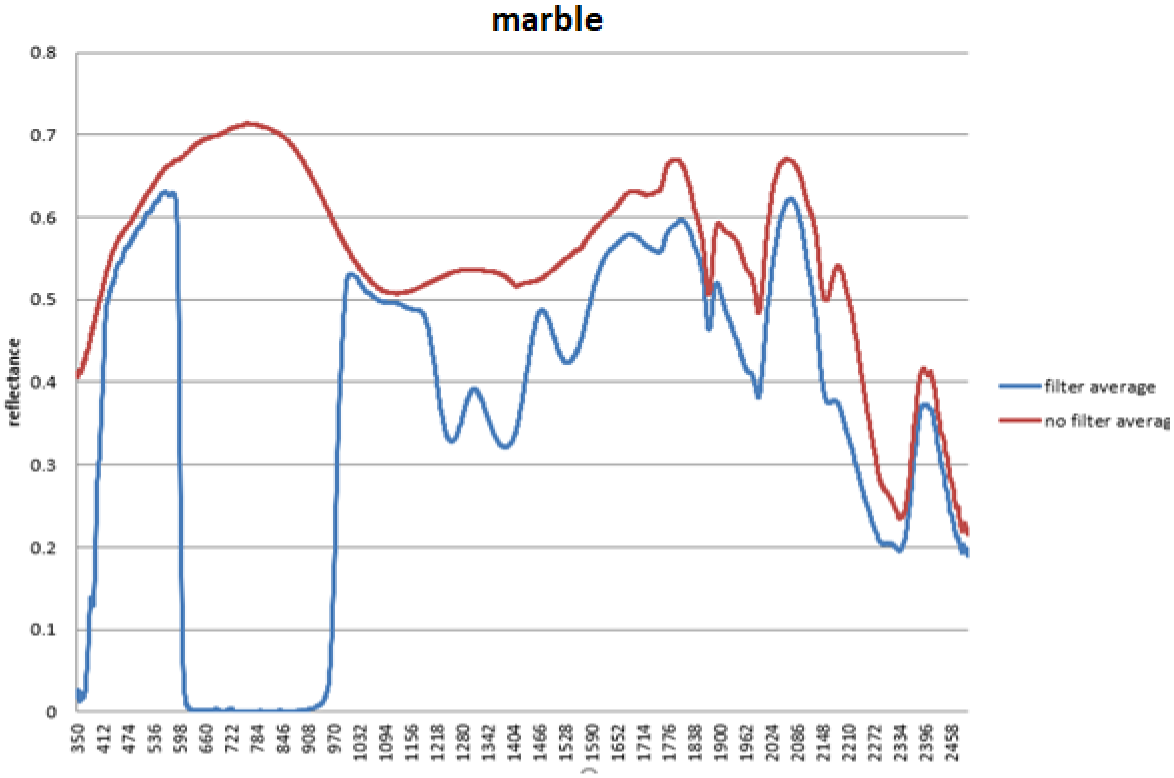

Figure 5.8. Reflectance curve of a marble with and without the custom-designed filter plotted in blue and red colours respectively. Beyond 600 – 950 nm absorption area, the filter shows additional absorption of EMR between 1200 – 1600 nm wavelength but it follows the marble spectral curve in other regions.

There is slight difference between the response curve of the selected materials with and without the custom filter, though they all show good filter performance. In addition to the quantifiable optical performance of the filter, there are other properties that are somewhat more difficult to measure and not related to this research. These are associated with the quality of the materials and substrates. Substrates are indicated with respect to any optically worked part, such as flatness or curvature of surface, the amount of polish and the quality of any coating (Angus 2010, p. 646). These factors can potentially cause additional absorption at different wavelengths which is illustrated as blue and red lines in Figures 5.8 – 5.9 which demonstrate how EMR is affected after passing through a custom-designed. The absorption of EMR does not depend on the intensity of the EMR, despite the fact that under certain conditions the transparency of the medium can change, and that these changes are subject to the intensity of waves going through the medium. In these cases, storable (nonlinear) absorption occurs (Stankov 1988).

Attenuation is the reduction in the intensity of a light wave propagating through a medium by absorption of its photons (CTI 2016). Comparing Figures 5.8 and 5.9, it can be seen that at $\lambda > 400$ nm and $\lambda < 600$ nm when reflectance is low (e.g., green leaves) attenuation is minimal (i.e., the blue and red curves overlap), but when overall reflectance is greater (e.g., marble) a gap becomes noticeable between the blue and red spectra which indicates absorption is occurring at these wavelengths.

5.4. Chapter Summary

In VNIR wavelengths, the filter demonstrates acceptable opacity between 615 and 950 nm. In the remainder of the pass band (i.e., 400 nm – 615 nm and 950 nm – 1100 nm) transmission quality is high in that the curve is flat and transmission is >90%. The transmission decreases with increasing light intensity due to non-linear absorption. The performance of the filter in the pass regions can be explained by non-linear absorption, because greater attenuation occurs at higher reflectance conditions (William 2013). Transmission also can vary in different bands because of the energy characteristics of particular wavelengths, the minor difference of pass band curves indicates the variation between wavelengths is minor and the filter response is acceptable for the aim of this study.

Chapter 6

Verification of camera response

6. Measuring the camera spectral response

6.1. Introduction

This chapter reports on the evaluation of the custom-designed optical filter with a consumer grade digital camera at different wavelengths and transmission rates using a FieldSpec4® Hi-Res spectrometer. While this was an essential prerequisite before the remaining research in this thesis could take place, it is also a research element in itself.

6.2. Reflectance response of the camera with custom filter

Most advanced camera sensors utilize CCD or CMOS technologies that have numerous common elements, e.g., comparative structures, materials and basic operations. Both type of imagers to convert EMR into electric charge and process it into electronic signals. Both of these technologies have both positive qualities and shortcomings giving each advantages in different applications.

The CCD sensor is a silicon chip that contains an array of photosensitive elements. The term charge-coupled device refers to the technique by which charge parcels are transferred from the photosites to readout. Clock pulses make potential wells to move charge parcels around on the chip, before being changed over to a voltage by a capacitor. In a CMOS sensor, every pixel has its own particular charge-to-voltage transformation, and the sensor regularly incorporates amplifiers, commotion rectification, and digitization circuits, so that the chip yields digital bits. Sensors make digital images by changing over photon energy to electrical energy. The effectiveness by which every photon is changed over to an electron is the sensor's Quantum Efficiency (QE). The QE is computed by basically dividing the number of electrons by the number of photons. On the off chance that no electrons are made, the effectiveness is clearly zero, while if every photon makes one electron the productivity is 100%. Regularly, a sensor has diverse efficiencies at different light frequencies. For over 10 years, back-illuminated silicon CCD cameras have been common instrument for NIR imaging and spectroscopy because of their high resolution, generally modest cost, and adequate QE in this region of spectrum. However, even the best NIR CCDs do not give sufficient sensitivity at λ > 1200 nm (Figure 4.5). Consequently, the spectrometerr utilises InGaAs photo-diodes in the 1001 nm – 1800 nm wavelength range (Edmund n.d.).

Image has been removed due to copyright restriction.

Figure 6.1. Relative response curves of Si and three different types of InGaAs sensors. Note the good relative responsivity between 400 and 1100 nm for the Si sensors, and lack of response beyond 1100 nm (Hamamatsu 2015).

A typical digital camera utilizes an array of millions of tiny light photosites to record an image. In any case, the photosite would just create a mono colour image. A Bayer filter mosaic is a a colour filter array (CFA) for organizing RGB channels on a square matrix of photosensors. To capture colour pictures, a filter is put over every pixel so that particular wavelengths of EMR are transmitted. For all intents and purposes all contemporary digital cameras can only capture one of three essential colours in every pixel, thus they dispose of about 66% of the incoming light. Accordingly, the camera needs to approximate the other two main colours in order to have full colour in each pixel. The raw output of cameras with Bayer filters (Figure 6.2) is alluded to as a Bayer pattern image. To conquer the issue due to every pixel being sifted to record just one of the three essential colours, and not having the capacity to completely indicate red, green and blue, de-mosaicking calculations are utilized to interject the total arrangement of colours for every pixel value to get a full-colour picture. These de-mosaicking algorithms utilize the benefits of encompassing pixels in value estimations of every pixel.

Image has been removed due to copyright restriction.

Figure 6.2. Bayer filters split the light in three visible channels - blue, green and red - which are interpolated inside the sensor to form a full-colour image (Cheremkhin, Lesnichii & Petrov 2014).

It is important to understand the difference between spectrometer and camera sensor readings. Table 6.1 shows the key differences between these two sensors.

Table 6.1.Key differences between light measurement of the spectrometer and digital camera

	Function of a system	**Light detection component**	**Readout output**
ASD FieldSpec4® Hi-Res spectrometer	Sensing EMR	Diffraction grating which converts the very narrow band incident light to electrons	Digitized electrons through computer
Digital Camera	Sensing EMR	Bayer CFA which converts the very wide band incident light to pixel values	Blue, green and red band colour information per each pixel

The basic function of a spectrometer is to sense light, divide it into its spectral components, digitize the signal as a function of wavelength, and read it out and display to a computer. There are similarities to a digital camera, which also takes in light and divides it into red, green and blue bands. The colour (Bayer) filters in the camera act like a diffraction grating in a spectrometer, but with huge bandwidth (i.e., very low spectral resolution) rather than a narrow bandwidth in a spectrometer, and place the right colour in right position through interpolation. A key difference, however, is that the output of spectrometer is one-dimensional while that of an image sensor has two dimensions.

6.3. Data collection and analytics

The main purpose of this experiment within the overall research project is to compare the difference in readouts from the two devices on selected samples, and to examine are any relationships between them. As shown in Section 5.3.2, the spectrometer test for verifying the spectral response of the designed filter was satisfactory. The grey card used in this test is an approximate realization of a Lambertian scatterer and is a flat object of a neutral grey colour that derives from a flat reflectance spectrum (in natural light). In photography, a major use of grey cards is to provide a standard reference object for exposure determination. The white and black cards are considered to be grey cards of different reflectance. The black card has 10% reflectance and the white card 90% across the visible spectrum. The grey card has 50% reflectance.

To compare the performance of the two detectors — the spectrometer and the digital camera image – two types of measurements were conducted; one using the camera without the custom-designed filter and another using it with the filter. A no colour, homogeneous reflective object was sensed so that the image sensor just recorded the characteristics of light source. Figure 6.3 shows images of the white reference panel taken with and without the filter. The right-hand image appears reddish because after removing built-in IR blocking filter, more IR light leaks into the red band than into the blue and green bands (*cf.* section 5.1).

DSC09657.ARW
16/09/2015 12:17 PM
DSC-RX1
35mm F2.0
1/80 sec. F8.0 +0.0 EV ISO100

DSC09658.ARW
16/09/2015 12:17 PM
DSC-RX1
35mm F2.0
1/400 sec. F8.0 +0.0 EV ISO100

Figure 6.3. Images acquired with the Sony RX1 DSLR camera of the ASD white reference panel with the custom-built filter (left) and without the filter (right).

The images were acquired in RAW file format, i.e., unmodified ‘raw’ pixel information from the digital camera's sensor. The auto white balance used in acquiring RAW images does not affect DN values. To maintain a constant exposure, the camera was set to a fixed f-number so that the shutter speed could be adjusted automatically by the camera. By using a fixed f-number, different light fluxes acted on the sensor but there was no linearity related to the shutter speed times and the f-number. A digital number (DN) is typically used to describe the attributes of pixels without any physically meaningful units. In the experiments conducted at this point, the pixel values do not need to be interpreted as physically meaningful, quantitative values; and comparisons were made between the DN readouts of the two imaging devices.

To investigate that how the spectrometer performs in the visible light range, DN values were cropped for wavelengths between 400 and 700 nm and then divided into three bins: 400 nm – 500 nm (visible blue), 500 nm – 600 nm (visible green), and 600 nm – 700 nm (visible red) bands (see Table 6.2). The average DN value was calculated for each of those three bands. The test was then repeated with the 600 nm – 950 nm blocking filter (Figure 6.4).

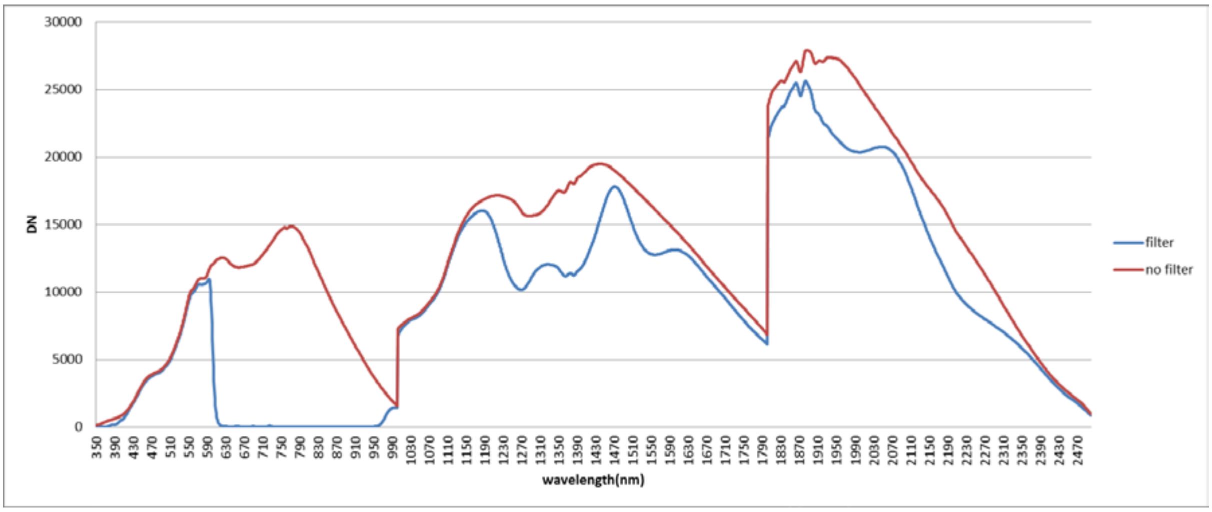

Figure 6.4. Raw DN (16 bit) values of the white reference panel with ASD Illuminator light with and without the custom-designed filter measured using spectrometer. The radiance of the light source increases as wavelength increases within visible range.

Table 6.2 shows the average DN values for blue, green and red bands recorded by the spectrometer with and without the custom filter. It should be noted that the DN is 16 bit and ranges from 0 to 65536. The very low DN value in red band can be explained by the use of the custom-designed filter, which blocks red light.

Table 6.2. Average DN values for blue, green and red with and without the custom-designed filter.

	Wavelength range (nm)		
Average DN	400-500	500-600	600-700
Without custom filter	2847	8751	12123
With custom filter	2690	8346	414

DN values from the spectrometer by default are 16 bits (from 0 to 65536) whereas the camera readouts are 8 bits (from 0 to 256). For the ease of comparison (Table 6.3), DN values of the spectrometer were downgraded to 8 bits. However, when the DN values from the two devices are compared initially differentiation between them was difficult, indicating more measurements from larger dataset would be needed for statistical analysis.

Table 6.3. Comparison of DN values acquired by the spectrometer and the Sony RX1 DSLR camera for the white reference panel with and without the custom-designed filter.

	400 – 500nm (filter)	500 – 600nm (filter)	600 – 700nm (filter)	400 – 500nm	500 – 600nm	600 – 700nm
Raw DNs from spectrometer in 16 bits	2690	8346	414	2848	8752	12124
Spectrometer's DNs converted to 8 bits	11	33	2	11	34	47
Amplify 5 times	53	163	8	56	171	237
DNs of Sony camera images	65	101	88	100	123	245

In the light source spectrum measured by the spectrometer (Figure 6.3), DN values consistently increase to approximately 780 nm. The high R-squared value of all three trend lines in Figure 6.6 confirms this increase and the slopes of the trend lines comply with slopes in visible spectrum in Figure 6.7, i.e., the greatest increase in reflectance occurs with the white card and the least with the black.

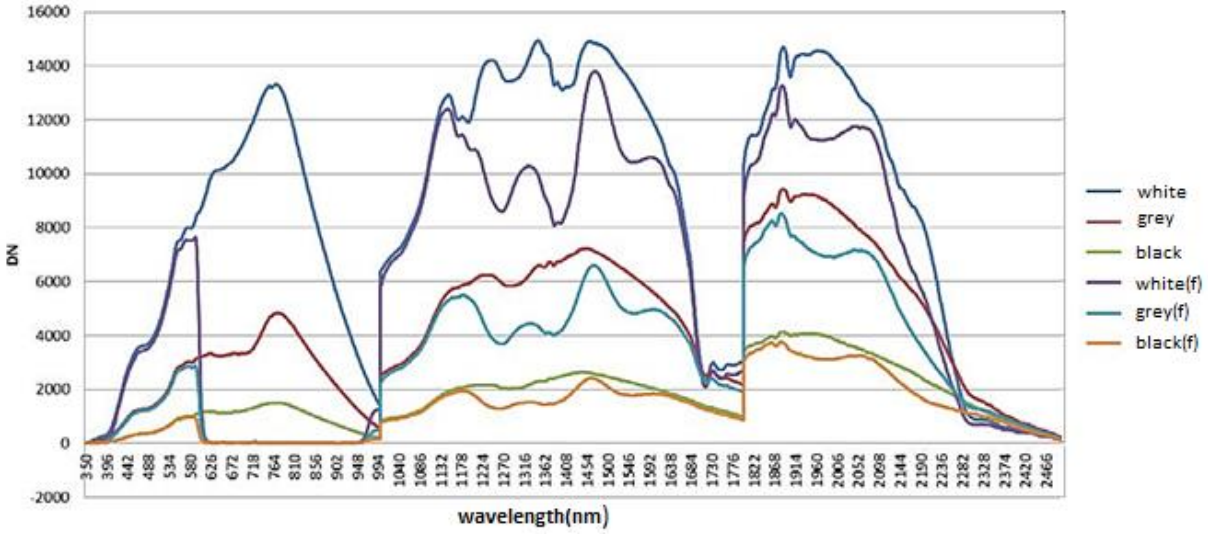

Figure 6.5. Raw DN (16 bit) responses of the white, grey and black photographic cards with and without custom-designed filter.

The camera readings lose their linearity for all three cards when converted from 16 to 8-bit indicating that the camera sensor does not behave the same as the detector in the spectrometer and, therefore, represents the characteristics of the light source differently. Bivariate linear regression was used to model the relationships between X and Y for the red, green and blue bands with and without filter (Figures 6.6 and 6.7).

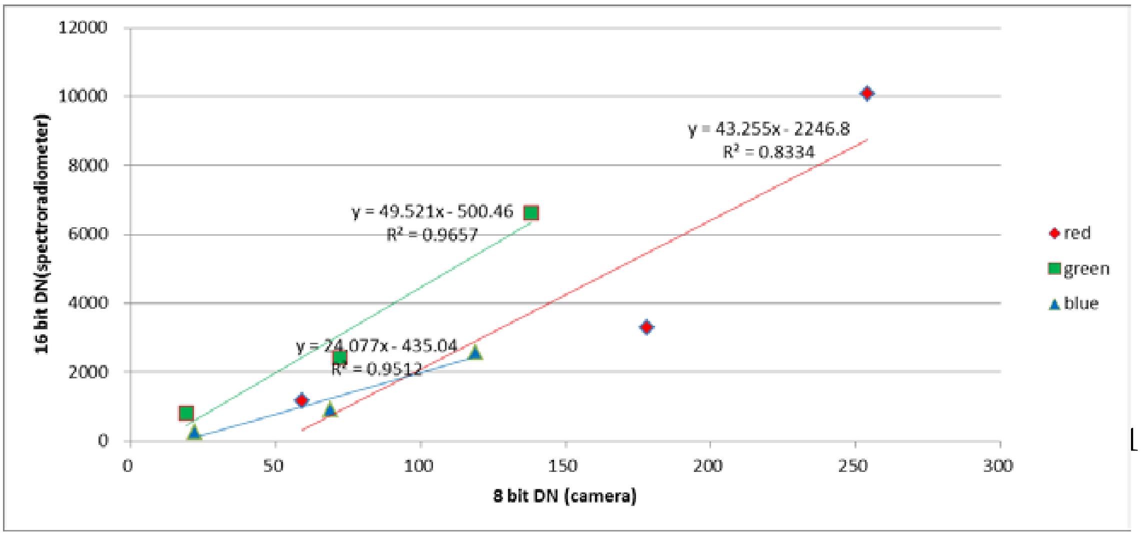

Figure 6.6. Linear regressions model for the white, grey and black cards in the red, green and blue bands, without the custom-designed filter. The linear regression model for green and blue DNs implies significant association between the two variables. This model for the red band implies weaker correlation between the camera and spectrometer readouts.

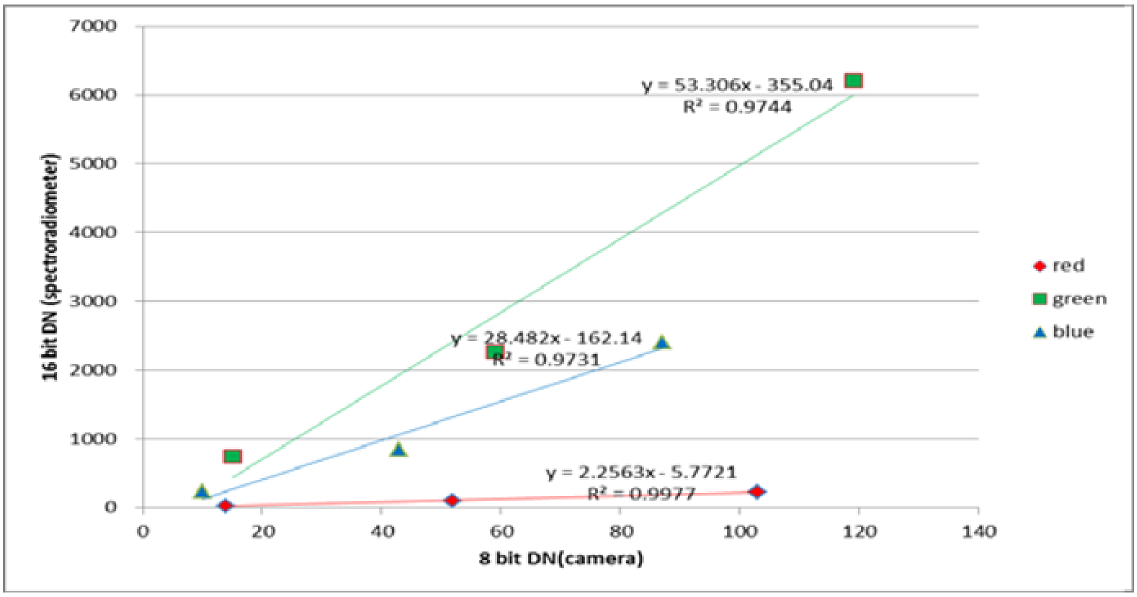

Figure 6.7.Linear regressions models for the white, grey and black cards in the red, green and blue bands with the custom-designed filter. High R-square values for red, green and blue bands shows a good linear relation for DN values in each band. It indicates how the correlation between the spectrometer and camera readouts is significantly enhanced after using the custom-designed filter.

In undertaking this analysis the FieldSpec4® Hi-Res ASD output was statistically standardized to 1 nm intervals to obtain 100 readings that corresponded to the 100 nm range of each of the red, green and blue bands, i.e., 400 nm – 500 nm, 500 nm – 600 nm, 600 nm – 700 nm.

Table 6.4. The regression models between ASD and camera responses with the custom-designed filter

Band	**Regression models with filter**
Blue	$y = 28.482x – 162.14$
Green	$y = 53.306x – 355.04$
Red	$y = 2.2563x – 5.7721$

where y is 16-bit DN of the spectrometer which has been averaged in each 100 nm bandwidth. X is the DN of RGB band in camera RAW image acquired by using Adobe Photoshop CC.

Figures 6.6 shows that the camera readings without the filter have linear relationship with the FieldSpec4® Hi-Res ASD readings for blue and green bands. Figure 6.7 implies that this relationship is improved when the custom-designed filter is used. These results were cross validated using out-of-sample testing to see if the different models performed equally well on data that was not used to develop the model. In this validation exercise, a standard 18% grey photographic card was used as the target sample, but the light source, position of devices and camera settings were not altered. The DN values for this target measured by both FieldSpec4® Hi-Res ASD and the camera with the filter are presented in Table 6.5. Then, using the linear regression model obtained in previous step, the predicted DNs was compared against the observed DNs and the sum of square of residuals between observed and predicted DNs was analysed (Table 6.6). Comparing the square of residuals shows the accuracy of prediction of the out-of-sample grey card is 93%, 73% and 99% for the red, green and blue band respectively when the custom-designed filter was used. This confirms that the modified digital camera has acceptable spectral response and could be used further in this research.

Table 6.5. Observed and predicted DN value for a grey card with 18% reflectance across the visible spectrum (18% grey card) and the custom-designed filter. In this table ASD stands for FieldSpec4® Hi-Res spectrometer and Sony refers to the Sony Rx1 DSLR camera.

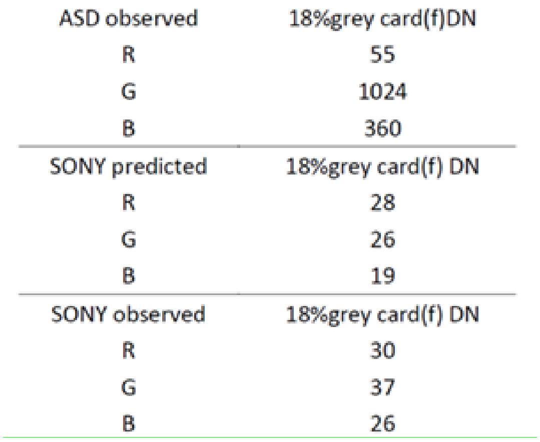

ASD observed	18%grey card(f)DN
R	55
G	1024
B	360
SONY predicted	18%grey card(f) DN
R	28
G	26
B	19
SONY observed	18%grey card(f) DN
R	30
G	37
B	26

Table 6.6. Sum of squares of the residuals between predicted DN values of the camera and observed DN values. Comparing the square of residuals shows the accuracy of prediction on grey card (highlighted by red, green and blue) is %93 for red band, %79 percent for green band and %99 for the blue band using the custom-designed filter.

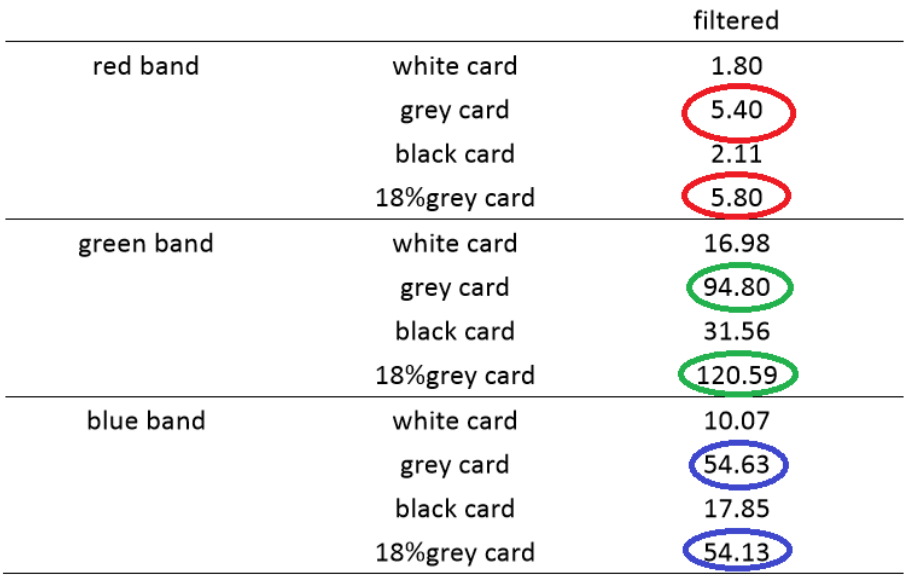

		filtered
red band	white card	1.80
	grey card	5.40
	black card	2.11
	18%grey card	5.80
green band	white card	16.98
	grey card	94.80
	black card	31.56
	18%grey card	120.59
blue band	white card	10.07
	grey card	54.63
	black card	17.85
	18%grey card	54.13

6.4. Chapter Summary

In this chapter the spectral response of the custom-designed filter as well as the relationship between FieldSpec4® Hi-Res ASD and camera sensor readouts were examined in order to verify the spectral reflectance characteristics of the modified camera. The custom-designed filter tested in this project has a sharp transition, or cut-off, between the zones of maximum and minimum transmission (Figure 6.5). This indicates strongly that it can be used for scientific and technical work.

The differences in the DN values acquired by the two devices for the same samples can be caused by many factors. Though both sensors are based on silicon photodiodes, the peripheral components derived from different designs and can significantly affect their outputs. Digital camera sensors are inherently sensitive to infrared light. After applying the external filter (*cf.* Appendix 2), λ = 600 nm – 950 nm light was blocked, and the DN values recorded by the red band is the response from a small portion of

NIR (λ = 950 nm – 1100 nm). Therefore, if the light intensity is strong enough or the exposure time is long enough, the camera sensor will present information in this frequency range.

As discussed in introductory chapter, longer wavelengths are scattered less than short wavelengths which means that the custom-designed filter has the potential to be able to penetrate gaseous smoke and other similarly sized particles in its NIR bandwidth. In the next chapter, the images obtained using this filter over an atmosphere with gaseous smoke from a bushfire and a controlled burn area are analysed, and the algorithms developed for image visibility enhancement are introduced.

Chapter 7

Algorithm development and testing

7. Algorithm Development

7.1. Introduction

This chapter explains the development of the image processing techniques applied to the data acquired by the modified, digital camera-and-filter system to penetrate gaseous smoke. As discussed in Sections 2.7 – 2.8, there are typically two typical methods are used to enhance the visibility of haze-affected imagery covered by haze. These are the single image and multiple images approaches; both to minimize or eliminate atmospheric scattering affects. The multiple images approach requires image data from more than one camera simultaneously making it difficult and inefficient to deploy. Although the single image approach is therefore the preferred method, and despite the fact that it has been evaluated and optimized over the past few years (Section 2.7); it has shown that these techniques are not suitable for the scene visibility enhancement if the entire scene is covered by smoke particles (Liu et al. 2011).

The method proposed and developed in this research thesis is inspired by both the single and NIR-guided image haze reduction methods (He, Sun & Tang 2011; Vanmali, Kellar & Garde 2015). As discussed in Section 2.9, the spectral sensitivity of a typical DSLR camera allows NIR radiation to be captured as a replacement for one of the three main colour (RGB) channels. In this research, the DSLR camera was modified to capture blue and green light, and a portion of NIR radiation ($\lambda = 950$ nm – 1100 nm) as a replacement for the red channel. As discussed in Chapter 5, one of the main criteria in designing an optical filter is the selection of a blocking band (from the blue, green and red bands) to preserve original image colour as best as possible. Because the red band is the closest spectrally to NIR, this band was sacrificed and replaced with NIR. It did not significantly degrade the original image colour and enabled a single image to collect co-registered blue, green and NIR bands simultaneously while preserving original colours as illustrated in Section 5.2. The selected range for the NIR wavelength enables the camera to capture EMR with almost 40 times less scattering amount at $\lambda = 1000$ nm compared to the blue light wavelengtha starting at $\lambda = 400$ nm (*cf.* Figure 5.5).

Figure 7.1 illustrates the procedure and workflow for designing the smoke penetration algorithm (SPA).

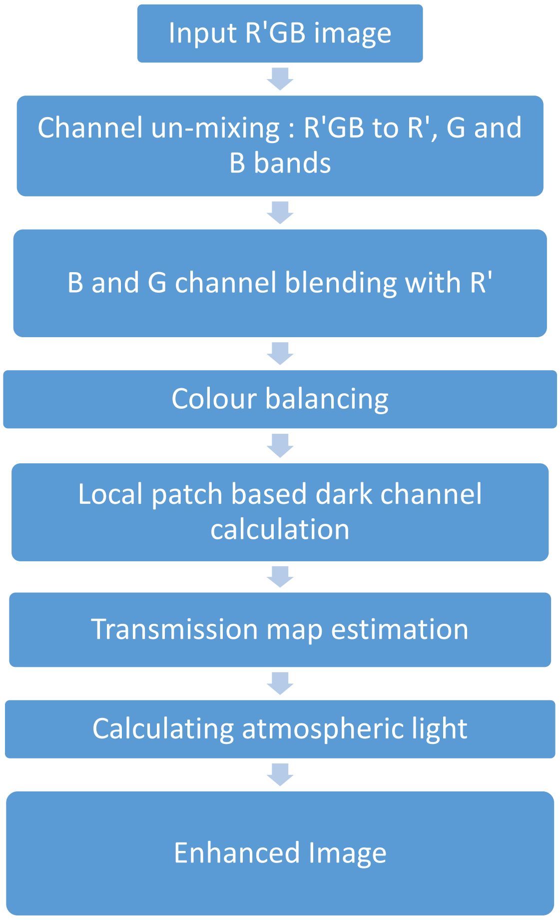

Figure 7.1.Workflow for the development of the smoke penetration algorithm (SPA) and image visibility enhancement in the research project. R' is the modified red channel which senses EMR between λ = 950 nm – 1100 nm.

As illustrated at Figure 7.1, after un-mixing the input image to three separate bands, the blue and green channels are blended by multiplying individual pixels by the corresponding pixels from the R' channel, as R' exhibits the minimum scattering effect. This is a key function in the smoke penetration algorithm (SPA) as builds up the image density and enhances the contrast globally. Colour balancing is applied to correct for the colour shift effects that may be caused by this blending operation. The resulting image is then divided into smaller windows (patches) so that low intensity pixels (dark pixels) can be identified. The intensity of these dark pixels can be used in accurate smoke transmission map estimation (He, Sun & Tang 2011). They also can be used to accurately estimate the light scattered by smoke particles or, so called atmospheric light. Therefore, by estimating these elements, a smoke-free image with the optimized scene visibility can be restored. These steps are discussed in detail in following sections.

7.2. Data used

Two data sets were collected over smoke, these included ground-based and aerial photography from a prescribed burn-off area using a modified DSLR Sony DSLR RX1 and Canon DSLR EOS-6D camera with the custom-designed filter to test the SPA (*cf.* section 3.3).

In addition to the custom-designed filter, another optical filter was experimentally used when collecting aerial imagery to evaluate the efficiency of the developed algorithm. That filter blocked blue visible light instead of red light, thereby allowing green and red light to pass. As a result, images captured using this experimental filter collected NIR radiation (λ= 700 nm – 1100 nm), green and red light. The logic for utilizing this filter was to optically limit the light scattering impact on collected images by blocking the blue channel which is more prone to light scattering compared to the other two channels. This experimental filter did not preserve the original image colour because the green and red channels were contaminated by the wide range of NIR wavelengths (*cf.* Section 2.9). The results from this use of this experimental filter have been published in (Chabok, Millington, Hacker, McGrath 2016)(Appendix 2).

Figure 7.2 provides a collection of some of images used for evaluating the SPA. These photos are captured using a modified DSLR camera equipped with the custom-designed filter from prescribed burn areas. It also includes an aerial image collected by ARA aircraft over a bushfire smoke (*cf.* Table 3.6).

Figure 7.2. Aerial and ground-based photos from smoke collected using the combination of modified, digital camera-and-filter system. Second image from top row was collected using the ARA research aircraft over a bushfire smoke and other photos were collected from prescribed burn area.

7.3. Algorithm development

The images used to test the development of the smoke penetration algorithm were captured using the modified single DSLR camera and custom-designed filter and consist of three bands: visible blue (400 nm - 500 nm), visible green (500 nm - 60 nm) and R’ between 950 and 1100 nm (Figure 7.3). These bands are internally co-registered inside the camera using the CFA filter and form a uniform single colour image, therefore working with separate bands does not require pixel co-registration. However, this would be a mandatory step if multiple imaging sensors were used in data collection.

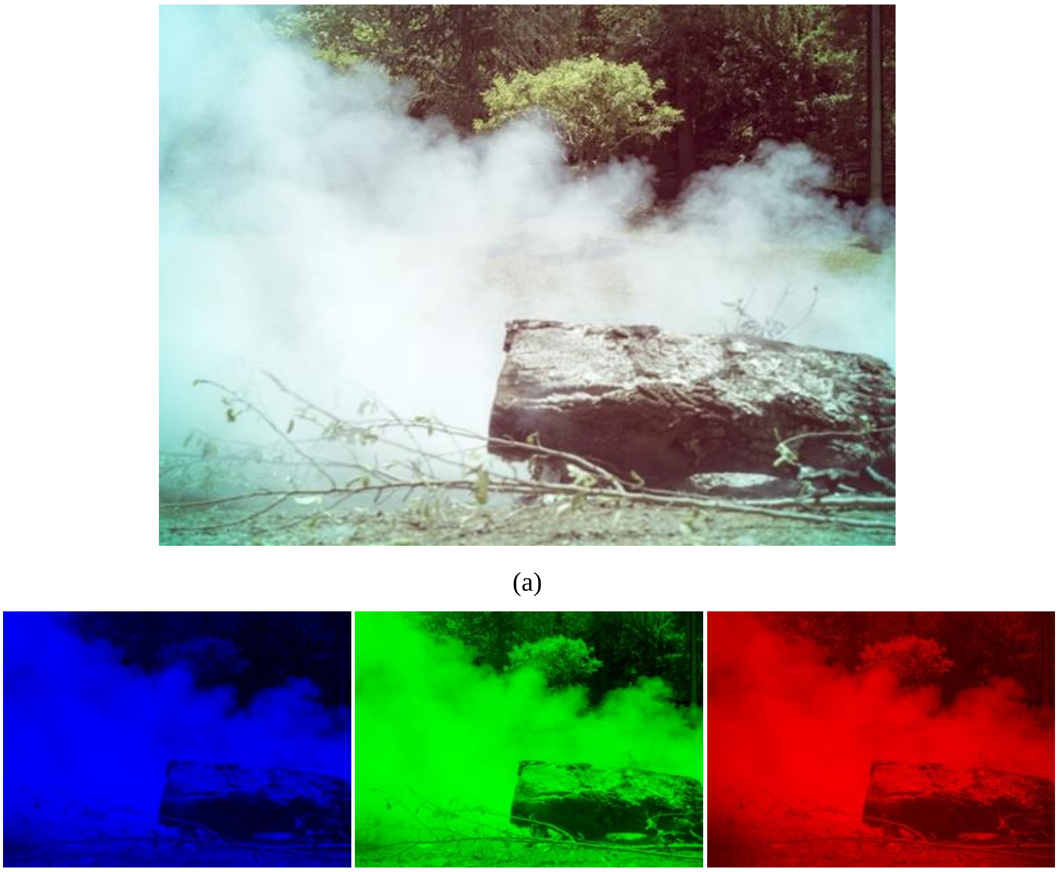

(a)

(b) (c) (d)

Figure 7.3. (a) Shows the input image captured by a ground-based camera divided into blue (400 nm – 500 nm) (b), green (500 nm – 600 nm) (c) and R’ (950 nm – 1100 nm) (d). This image is the top left-hand photograph in Figure 7.2

7.3.1. Channel blending

The first task in developing the SPA is to build up the image density. To do this the 400 nm – 500 nm, 500 nm – 600 nm and 950 nm – 1100 nm bands are extracted from the input image and three raster layers created from each of these bands. Given the fact that the NIR band exhibits less scattering than the two visible bands, the image density for the visible blue and green bands was built up by blending them with the NIR band. Equations 7.1 – 7.3 show the formulae used for this operation.

$$B^1_{(i,j)} = B_{(i,j)} \frac{NIR_{(i,j)}}{255} \tag{7.1}$$

$$G^1_{(i,j)} = G_{(i,j)} \frac{NIR_{(i,j)}}{255} \tag{7.2}$$

$$NIR^1_{(i,j)} = NIR_{(i,j)} \tag{7.3}$$

Where:

$B^1_{(i,j)}$, $G^1_{(i,j)}$ and $NIR^1_{(i,j)}$respectively are the new blue, green and NIR values at pixel (i,j) after blending with NIR channel, and *B* is blue channel, *G* is green channel, and *NIR* is the modified red with wavelength starting from 950 nm to 1100 nm. The result of channel blending for the input image is shown i Figure 7.4.

(a) (b)

Figure 7.4. (a) Input image, (b) Channel-blended image. This figure also uses the top left-image in Figure 7.2.

Applying these equations to an image results in a colour casting effect that offsets the image histogram for green and blue channels within the 0 – 255 range (Figure 7.5).

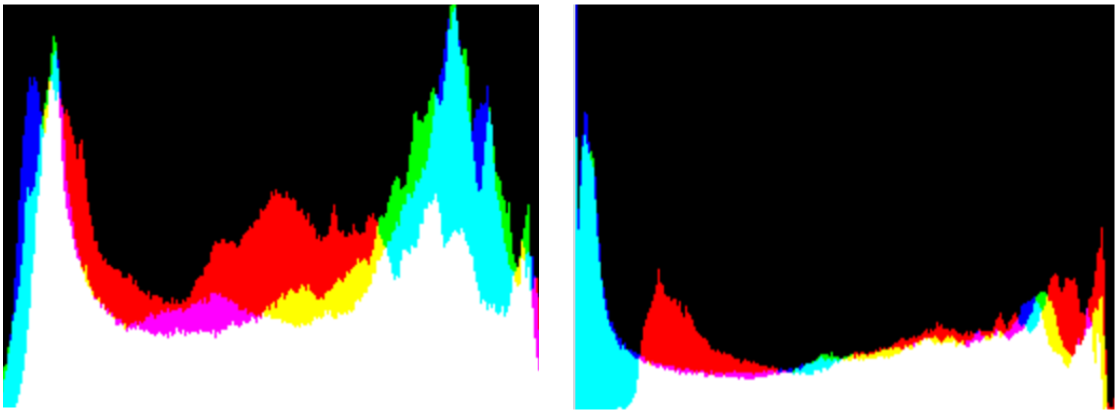

(a) (b)

Figure 7.5. (a) Shows the input image histogram before blending, and (b) after applying blending. It is clear from this pair of images that the blue and green channels are shifted after applying the blending operation.

Blending operation shifts the image colour from its original colour arrangement (Figure 7.4.b). To remove this shifting effect, the maximum and minimum value for each band was computed, and then based on Equations 7.4-7.6, colour balancing corrections were applied.

$$B^2_{(i,j)} = \frac{B^1_{(i,j)} - min(B)}{max(B) - min(B)} * 255 \tag{7.4}$$

$$G^2_{(i,j)} = \frac{G^1_{(i,j)} - min(G)}{max(G) - min(G)} * 255 \tag{7.5}$$

$$R'^2_{(i,j)} = \frac{R'^1_{(i,j)} - min(R')}{max(R') - min(R')} * 255 \tag{7.6}$$

Where $B^2_{(i,j)}$, $G^2_{(i,j)}$ and $R'^2_{(i,j)}$ are the corrected channels after applying colour balancing (Figure 7.6). The computed image after the application of Equations 7.4-7.6 was renamed to I : where $I_{(i,j)} = (B^2_{(i,j)}, G^2_{(i,j)}, R'^2_{(i,j)})$.

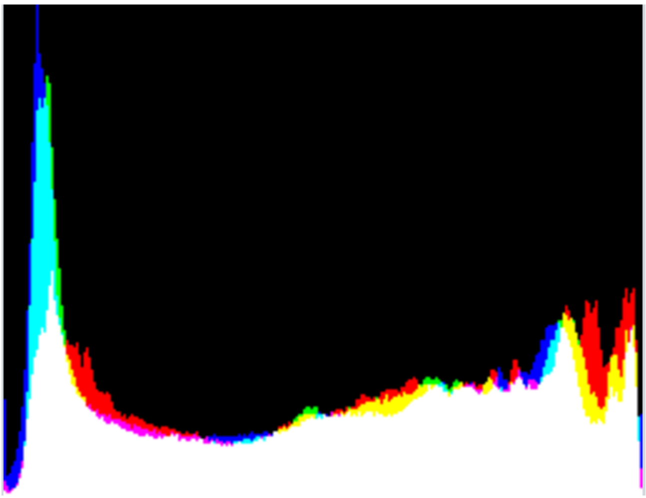

Figure 7.6. Corrected image histogram after applying colour balancing from 0 – 255 range.

7.3.2. Smoke modelling

Equation 7.7 shows the physically-based dichromatic model used in atmospheric optics for formulating haze (Narasimhan et al. 2002):

$$I_{(i,j)} = J_{(i,j)} t_{(i,j)} + a(1 - t_{(i,j)}) \qquad (7.7)$$

where $I_{(i,j)}$ is the DN of the pixel located at *(i,j)* coordinate from the image covered by smoke, $J_{(i,j)}$ is the DN of the pixel located at *(i,j)* coordinate from the smoke-free image, a is the path radiance, or atmospheric light, which is emitted by smoke, and $t_{(i,j)} \epsilon [0,1]$ is the medium transmission describing the portion of the radiation that is not scattered and reached the sensor. The aim in applying this equation is to recover a smoke- and haze-free image J from the input image I by estimating a and t.

For estimating transmission (t), He, Sun & Tang (2011) adopted the dark object subtraction technique in which the darkest pixels values are subtracted from the image as a single value based on their mean to remove spatially homogeneous haze. They named this technique the dark channel prior (DCP) method, and it is based on the statistics of smoke-free images. He, Sun & Tang (2011) used small windows across an image and found that on a clear day at least one colour channel had very low intensity in some pixels. In other words, there should be a local window located near the point of interest with the minimum intensity and in which the pixel has very low DN values. DCP-based approaches may fail if entire scene is covered by smoke. Therefore, to overcome this issue the blending operation introduced for building-up image density based on R' channel, discussed in the previous section, was used. Applying blending operation enables the DCP-based algorithms to locate and use low intensity pixel values from the R' channel.

7.3.3. Local patch-based dark channel estimation

To estimate the dark channel values, and input image is divided into smaller patches (Figure 7.7a) and the darkest pixel is calculated for each local patch using equation 7.8.

$$J_{(i,j)}^{dark} = min_{c\in\{r,g,b\}}\,(min_{y\in\Omega(i,j)}(J^{c}(y))) \qquad (7.8)$$

Where $J_{(i,j)}^{dark}$ is the dark channel of a colour image $J^{c}$for each local patch and $\Omega(i,j)$ is a local window of optional size, centered at *(i,j)* pixel coordinate.

Figure 7.7b shows the calculated dark channel for the input image with the local window size of 5 by 5.

(a) (b)

Figure 7.7. (a). The input image, (b) The dark channel image estimated using the equation 7.8, a smoke image is brighter than its smoke-free equivalent, and therefore the dark channel of the smoke image has higher intensity in regions with more smoke. Red window, Ω(i,j), represents a local patch in which the minimum pixel value is calculated for each image channel (R’, G and B).Minimum DN values for the red window on the left and right image are (170,230,231) and (107,107,107) respectively.

7.3.4. Transmission mapping

The intensity of the calculated dark channel introduced in the previous section is used to estimate smoke thickness or so-called transmission mapping. Equation 7.9 is obtained by applying the ‘minimum’ operation to equation 7.6 in a local patch $\Omega(i,j)$:

$$min_{y\in\Omega(i,j)}\,(I^c_{(i,j)}(y)) \quad = \min\,(J^c_{(i,j)}(y))t'_{(i,j)} + a^c(1 - t'_{(i,j)}) \qquad (7.9)$$

Where $t'_{(i,j)}$ is the medium transmission for the local patch. The other variables are defined at equation 7.7, and are independently applied to the three main colour channels for each local patch. Therefore equation 7.9 can be rewritten as equation 7.10 below:

$$min_{y\in\Omega(i,j)}\left(\frac{I^c_{(i,j)}(y)}{a^c}\right) \quad = min_{y\in\Omega(i,j)}\left(\frac{J^c_{(i,j)}(y)}{a^c}\right)t'_{(i,j)} + (1 - t'_{(i,j)}) \qquad (7.10)$$

After applying equation 7.10 to the three main channels (G, B, R’), all the pixels located in the local patch area, $\Omega(i,j)$, are replaced with the minimum value of these three channels as shown at equation 7.11 :

$$min_{c\in\{r,g,b\}}\,(min_{y\in\Omega(i,j)}\,\left(\frac{I^{c}_{(i,j)}(y)}{a^{c}}\right)) \quad = min_{c\in\{r,g,b\}}\,(\,min_{y\in\Omega(i,j)}\left(\frac{J^{c}_{(i,j)}(y)}{a^{c}}\right))t'_{(i,j)} + (1 - t'_{(i,j)}) \qquad (7.11)$$

Where $min_{c\in\{r,g,b\}}$ takes the minimum operation on three main colour channels. As discussed by He, Sun & Tang (2011), the dark channel of a haze-free image should tend to zero (Equation 7.12):

$$J^{dark}_{(i,j)} = min_{c\in\{r,g,b\}}\,(min_{y\in\Omega(i,j)}(J^{c}(y))) = 0 \qquad (7.12)$$

Because the atmospheric light (a^{c}) is always positive equation 7.12 can be rewritten as equation 7.13:

$$min_{c\in\{r,g,b\}}\,(\,min_{y\in\Omega(i,j)}\left(\frac{J^{c}_{(i,j)}(y)}{a^{c}}\right)) = 0 \qquad (7.13)$$

and therefore, by putting this at Equation 7.11, transmission $t'_{(i,j)}$ can be estimated as below as shown in equation 7.14:

$$t'_{(i,j)} = 1 - min_{c\in\{r,g,b\}}\,(min_{y\in\Omega(i,j)}\,\left(\frac{I^{c}_{(i,j)}(y)}{a^{c}}\right)) \qquad (7.14)$$

In real life conditions, even clear atmospheres contain a very small number of particles that cause light scattering and make distant objects in captured images look fuzzy. So, if the haze is removed thoroughly, the resulting image may look unnatural. For this reason, He, Sun & Tang (2011) introduced an optional constant haze parameter (0<ω≤1), see Equation 7.15 and 7.16, to retain a very small amount of haze in the image:

$$t'_{(i,j)} = 1 - \omega min_{c\in\{r,g,b\}}\,(min_{y\in\Omega(i,j)}\,\left(\frac{I^{c}_{(i,j)}(y)}{a^{c}}\right)) \qquad (7.15)$$

Or

$$t'_{(i,j)} = 1 - \omega J_{(i,j)}^{dark} \qquad (7.16)$$

Transmission estimations for the individual local patches across an image will contain some edge effects for each local patch due to the fact that the transmission is not always constant within a patch. To remove this, a 5x5 median filter is applied to each patch, which runs through each section of the local patch and replaces each pixel with the median of its eight neighbouring pixels (equation 7.17):

$$t'_{(i,j)} = med(1 - \omega J_{(i,j)}^{dark}) \qquad (7.17)$$

Figure 7.8b shows the estimated transmission map from the input image.

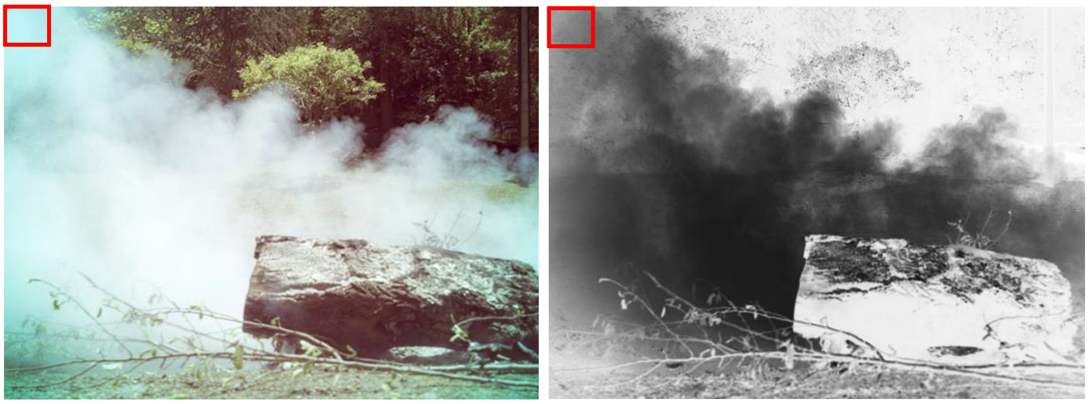

Figure 7.8. (a) The input image, (b) Estimated transmission map. Minimum pixel values for the red window on the left and right image are (170,230,231) and (116,116,116) respectively.

7.3.5. Estimating atmospheric light and restoring image DNs

Estimation of the atmospheric light, or the amount of the light scattered by smoke particles, is required for the production of the transmission map using equation 7.15. He, Sun & Tang (2011) found that the brightest pixel DN in the dark channel provides a good estimation of atmospheric light:

$$a = \max (J_{(i,j)}^{dark}) \qquad (7.18)$$

To restore the enhanced image, Equation (7.18) can be written as:

$$J_{(i,j)} = \frac{I_{(i,j)} - a}{\max\,(t_{(i,j)}, t_0)} + a \qquad (7.19)$$

From equation 7.19, if $t_{(i,j)}$ tends to zero then $J_{(i,j)}t_{(i,j)}$ will be very close to zero and therefore the enhanced image cannot be restored. To avoid this, a minimum value (t_0) is used to restrict the estimated transmission map from getting close to zero. A minimum value for t_0 is set to 0.1 for all the processed images displayed in this thesis. Depending upon the lighting conditions of the input image and optional constant haze value (ω) the resulting images may seem darker after the image restoration process. Thus, a discretionary histogram matching between the input and output images would enhance the visual appearance of the resulting image.

7.4. Results

Figure 7.9a shows the input image and Figure 7.9b shows the final result of applying the developed algorithm on the ground-based image introduced at the beginning of this chapter (Figure 7.1a). ω (see Equation 7.17) is set to 0.9 for all the images illustrated in this chapter. It can be seen that the scene visibility is significantly improved and enhanced after applying the SPA in each image. Figure 7.10 comprises zoomed-in sections of the images in Figure 7.9 and illustrate the effectiveness of the SPA developed.

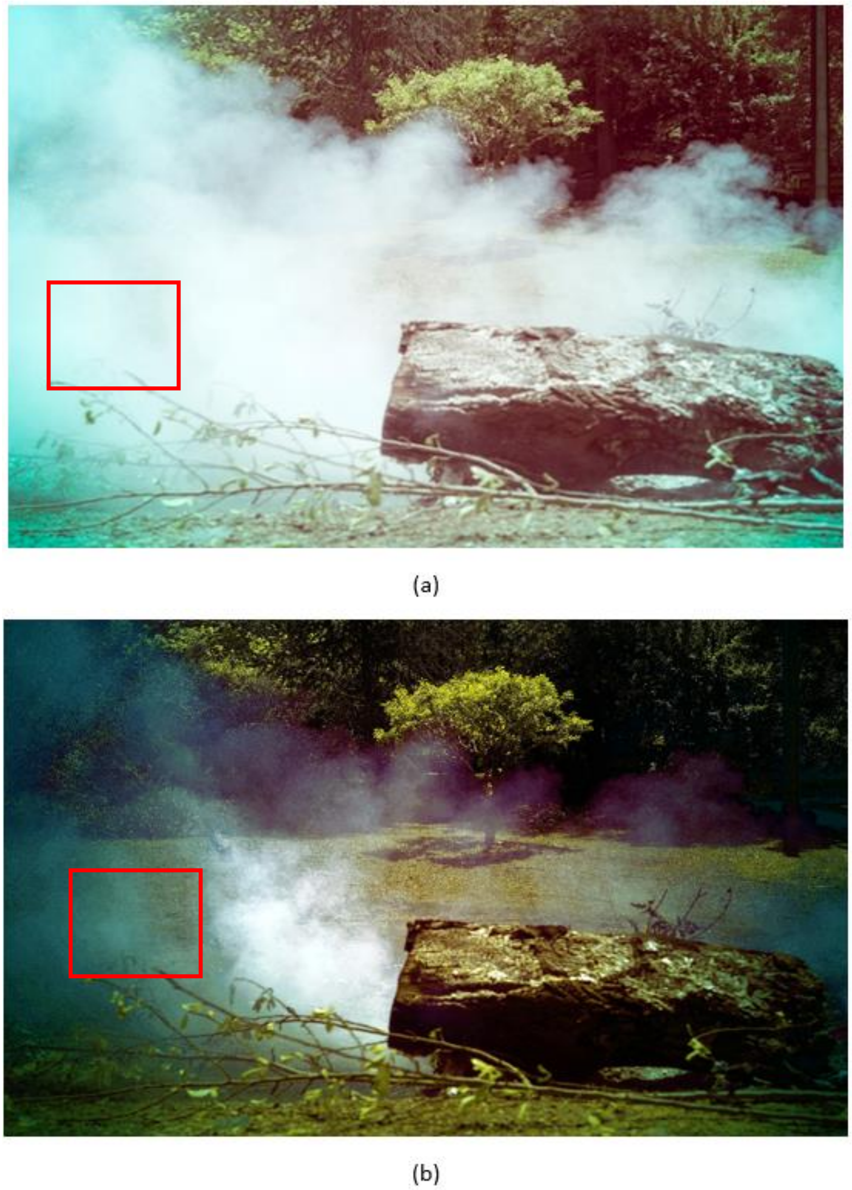

Figure 7.9. (a) The input image with smoke, (b) enhanced image after applying the SPA. Statistical summary of DNs for the pixels located inside the red window is listed at Table 7.1

Table 7.1. Statistical summary of DN values for the highlighted areas in red from Figure 7.9

	Input image (Figure 7.10a)			Output image (Figure 7.10b)		
	Min	Max	Mean	Min	Max	Mean
Red	214	252	232.15	88	229	137.90
Green	227	248	235.36	94	241	137.75
Blue	231	248	240.30	94	229	140.60

After applying the SPA, the enhanced image reveal some of the ground features that were previously obscured by smoke and emphasize that an image captured by the modified camera and custom-designed filter (Figure 7.9.a) by itself and without applying the SPA does not provide an adequate, clarity of vision in a smoke-affected scene.

Figure 7.10. Pairs of zoomed-in sections of the images extracted from Figure 7.10. In each pair the left-hand image shows the sections covered by smoke, while the right-hand image of each pair shows the enhanced sections after applying the SPA. See Table 7.1 for a statistical summary of DNs for the original image.

As discussed in Chapter 2, other haze removal methods are less efficient if the entire image is covered by smoke (Section 2.7). Figure 7.11 shows the effectiveness of the SPA for images covered entirely by smoke.

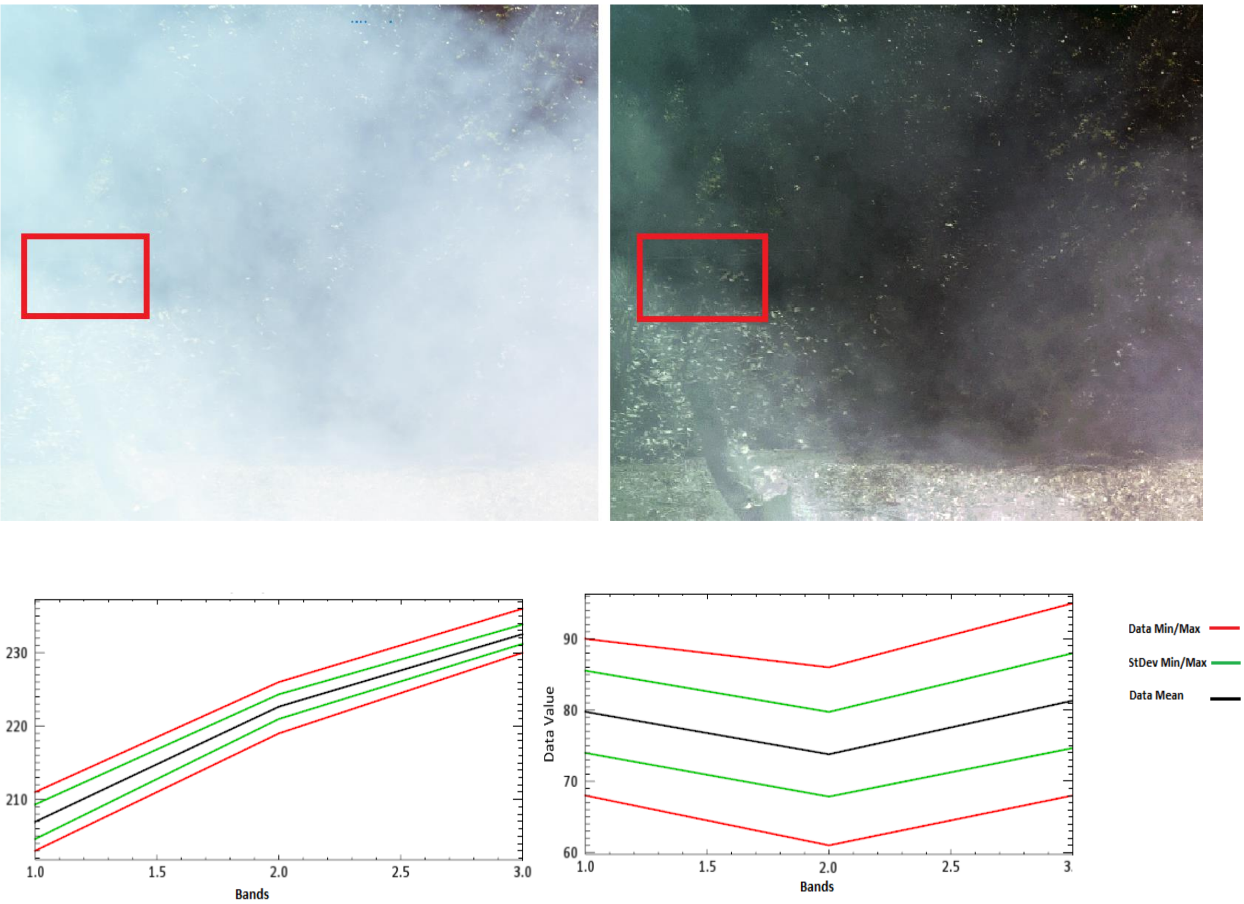

Figure 7.11. In the left-hand image the scene is mostly obscured by smoke. The right-hand image shows the scene after the SPA algorithm had been applied to the image. DNs for all the pixels in the area highlighted in red on both images used were extracted to generate statistical summary for minimum, maximum, mean and standard deviation of average DNs, which are shown in the graphs below the images.

Figure 7.11 demonstrates how ground features that were entirely covered by smoke and almost impossible to detect with the human eye, become visible after applying the SPA. For example, by looking at the input image one can hardly detect the trunk as the small tree in the left of the image, whereas it can be more clearly seen in the right-hand image. The statistical summary graphs of DNs from all the pixels located in the smoke region highlighted by the red rectangle confirms that before applying SPA, there was little discrimination between DNs but after applying SPA DNs were recovered and discriminated more successfully.

The airborne images displayed at Figure 7.12 were captured at an altitude of 600 m above the ground. After applying the SPA, visibility in the regions of gaseous smoke is greatly improved. Whereas for those regions that are covered by denser smoke, visibility improvement is less. This is because in the areas of dense smoke, there are also larger diameter particles that cause Mie and non-selective scattering (Section 2.5) in wavelengths between 950 nm – 1100 nm. The distance from the camera to ground objects plays a potentially important role in efficiency of the SPA. This is because as the distance between the camera and the ground increases the molecular scattering effect increases because more gaseous molecules occur along the pathway through the lower atmosphere. Figure 7.13 shows zoomed sections of the images from Figure 7.12 and compares the statistical graph of DNs for the pixels surrounded by red rectangle.

Figure 7.12. (a) the aerial imagery collected over a smoke-affected, and (b) the enhanced image after applying the SPA. This image was collected using modified CANON DSLR camera equipped with the custom-designed filter using the ARA research aircraft (*cf.* section 3.3).

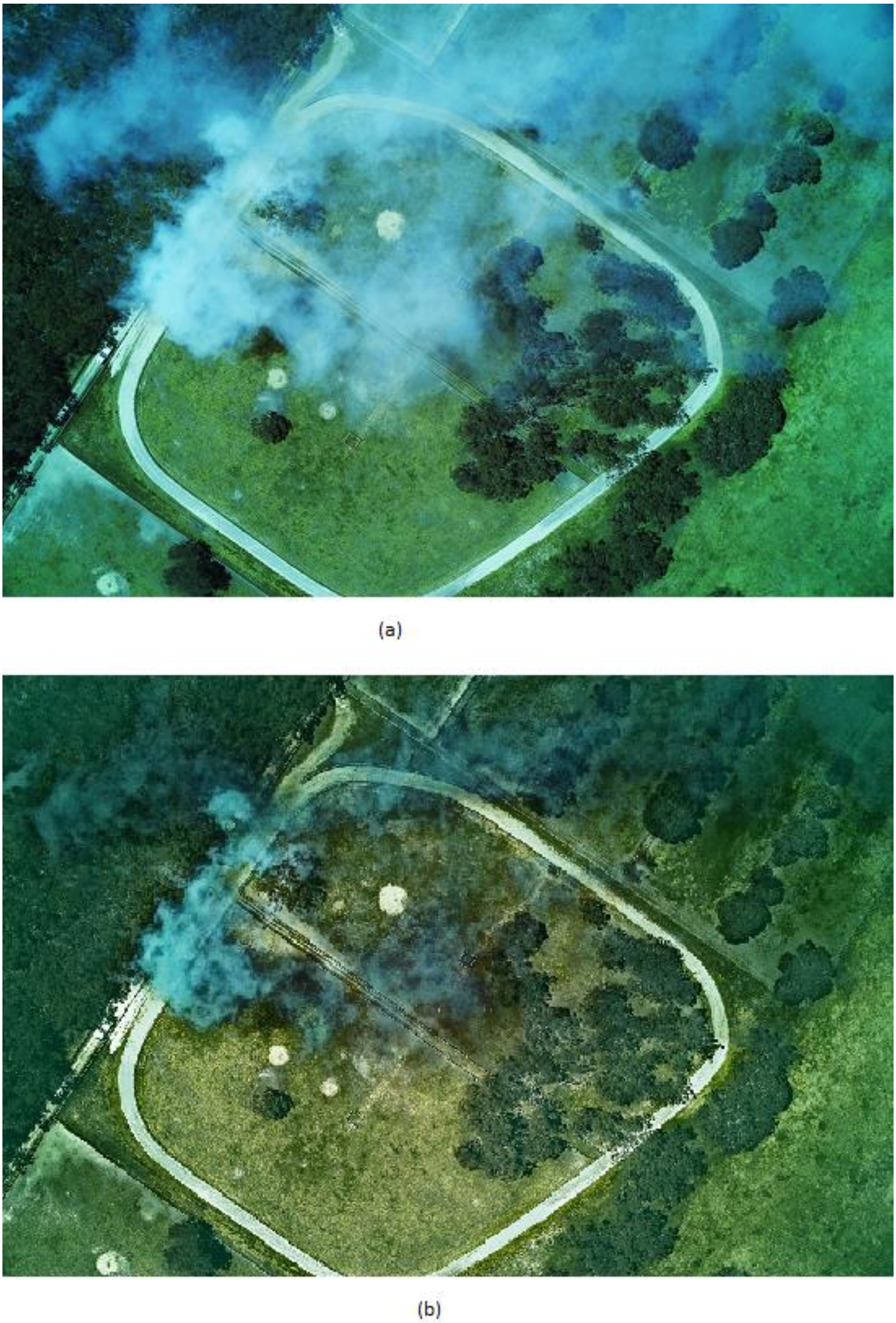

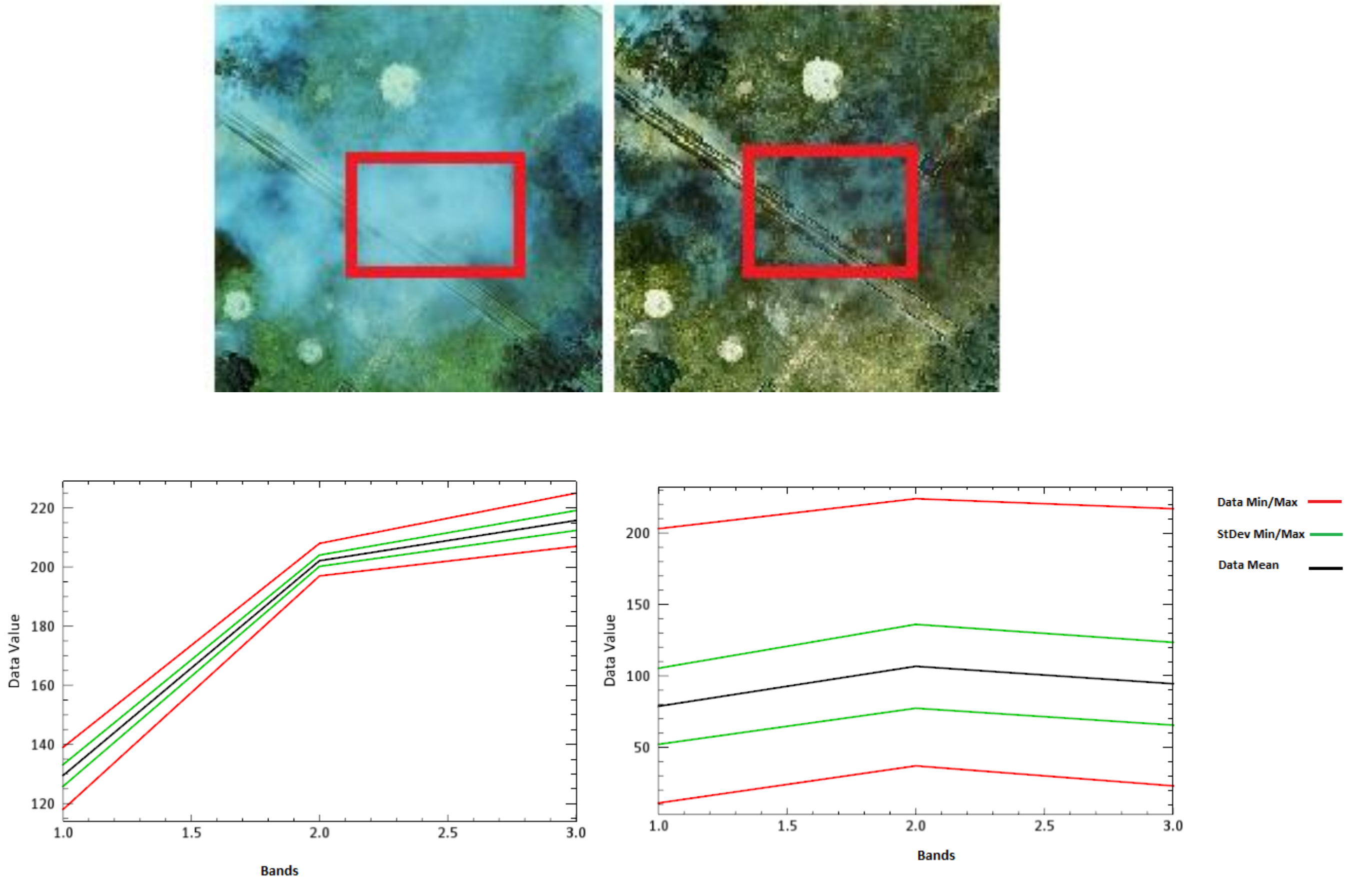

Figure 7.13. Zoomed sections of images from Figure 7.13. The left-hand image shows the situation before applying the SPA. The statistical for the red highlighted rectangle are shown below it. The right-hand image shows the situation after applying the SPA with the statistical summary below.

The graphs in Figure 7.13 again show SPA that there is minimal discrimination between the standard deviation, minimum, maximum and mean DNs of the pixels extracted from the image, as demonstrated by the green, red and black lines, before the SPA was applied. Whereas, after applying SPA there is much better discrimination.

Other results from images captured from a prescribed burn area in Belair National Park (*cf*. section 3.3) before and after applying SPA and improvements in the discrimination of DN statistics are illustrated in Figures 7.14 – 7.20.

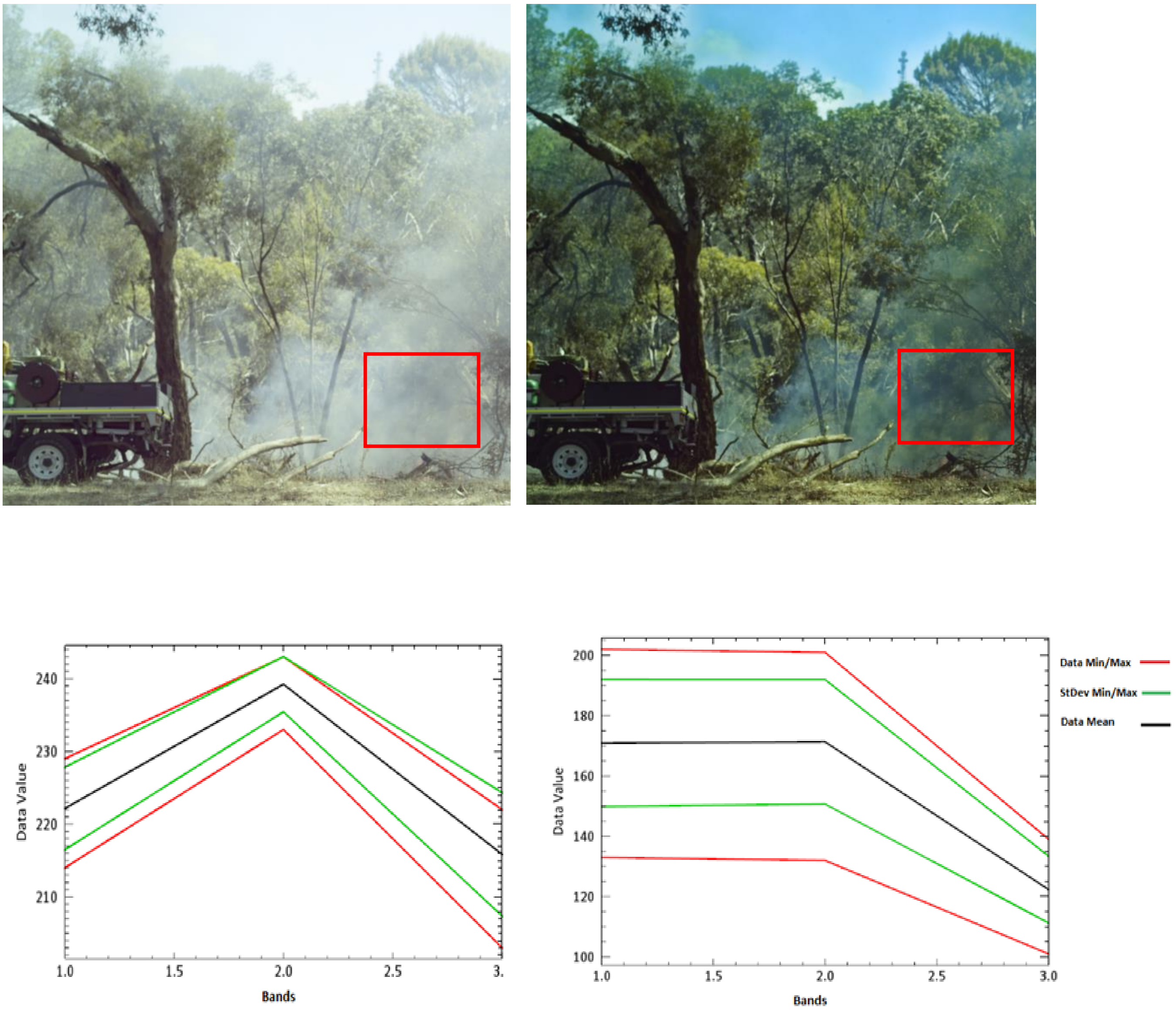

Figure 7.14. In the left-hand image the scene is partially obscured by smoke. The right-hand image shows the scene after applying the SPA algorithm. DNs for all the pixels in the area highlighted in red on both images used were extracted to generate statistical summary for minimum, maximum, mean and standard deviation of average DNs, which are shown in the graphs below the images for the left-hand and right-hand images respectively. These graphs show improved discrimination in the image DNs after applying SPA.

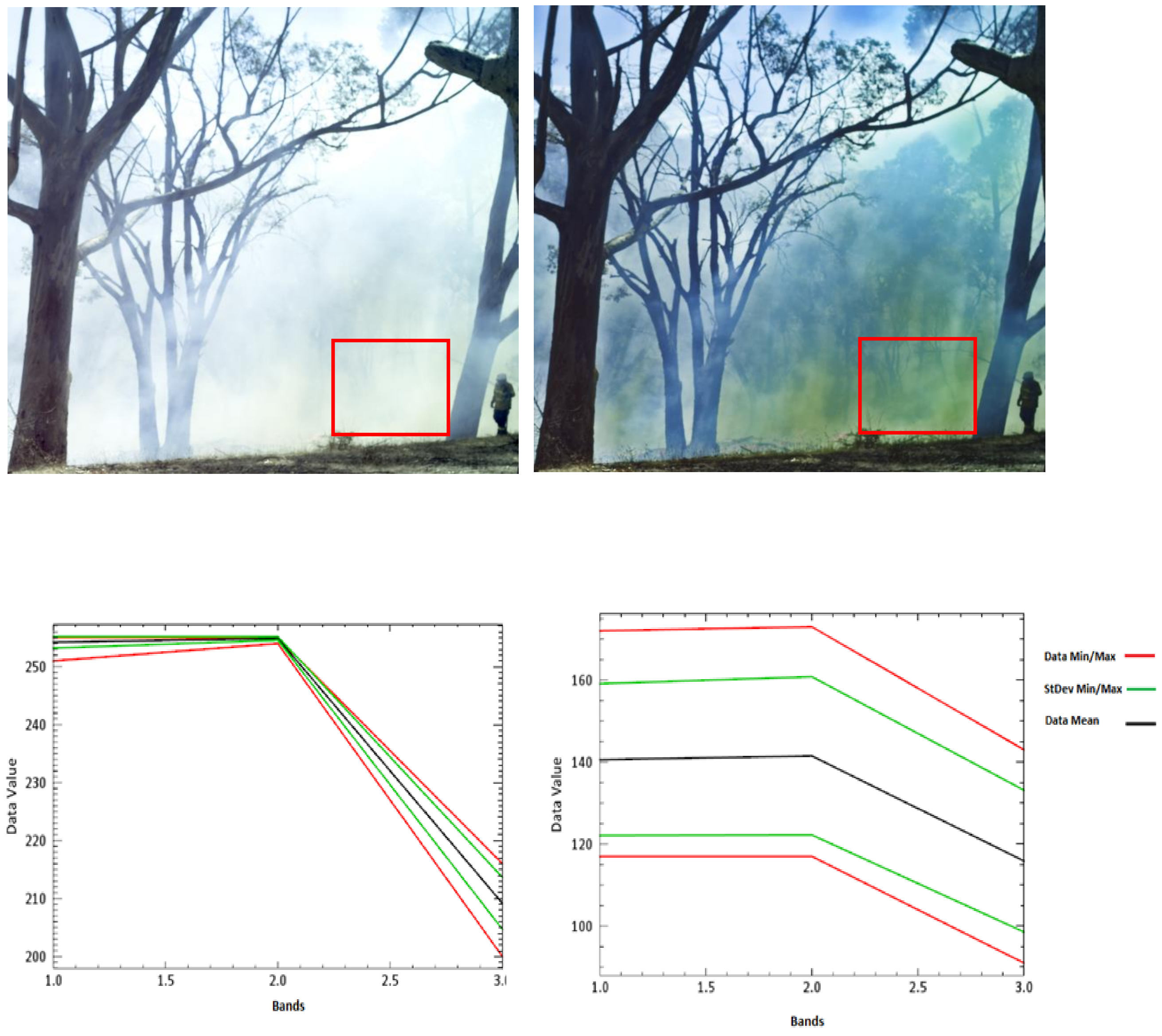

Figure 7.15. DNs for all the pixels in the area highlighted in red on both images (before and after applying the SPA) were extracted to generate statistical summary for minimum, maximum, mean and standard deviation of average DNs, which are shown in the graphs below the images for the left-hand and right-hand images respectively. These graphs show improved discrimination in the image DNs after applying SPA.

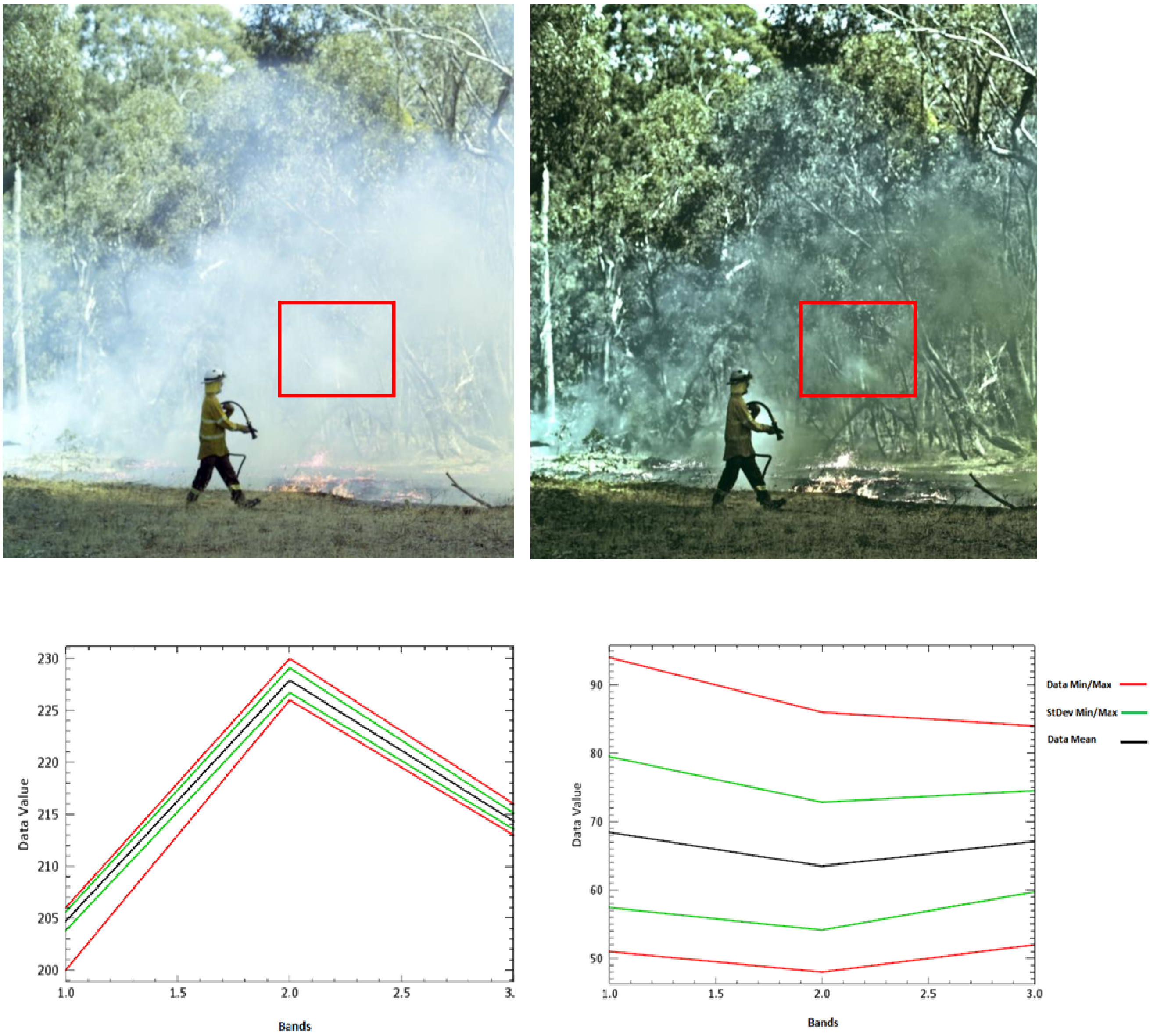

Figure 7.16. In the left-hand image the scene is partially obscured by smoke. The right-hand image shows the scene after applying the SPA algorithm. DNs for all the pixels in the area highlighted in red on both images used were extracted to generate statistical summary for minimum, maximum, mean and standard deviation of average DNs, which are shown in the graphs below the images for the left-hand and right-hand images respectively. These graphs show improved discrimination in the image DNs after applying SPA.

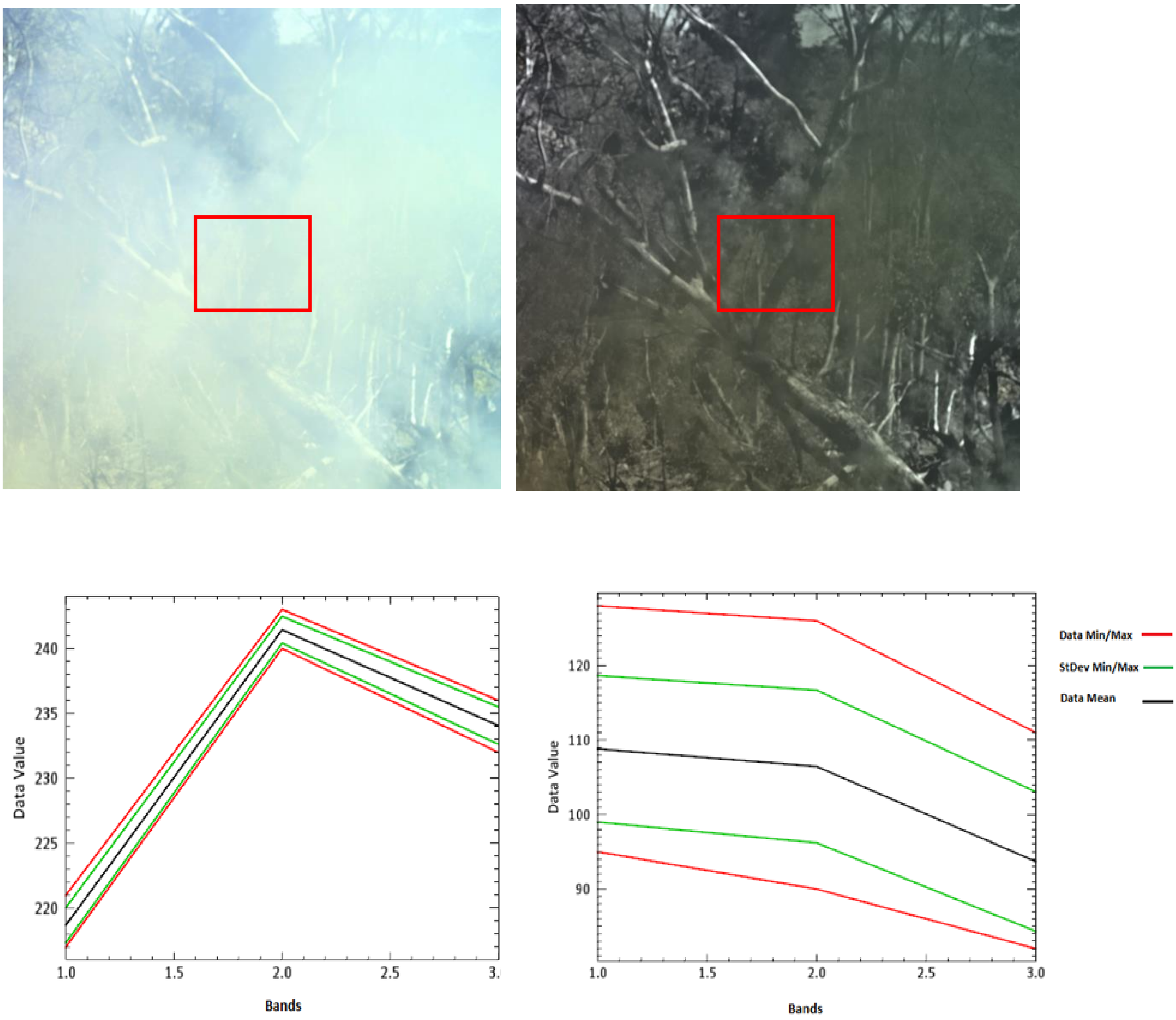

Figure 7.17. In the left-hand image the scene is mostly obscured by smoke. The right-hand image shows the scene after applying the SPA algorithm. DNs for all the pixels in the area highlighted in red on both images used were extracted to generate statistical summary for minimum, maximum, mean and standard deviation of average DNs, which are shown in the graphs below the images for the left-hand and right-hand images respectively. These graphs show improved discrimination in the image DNs after applying SPA.

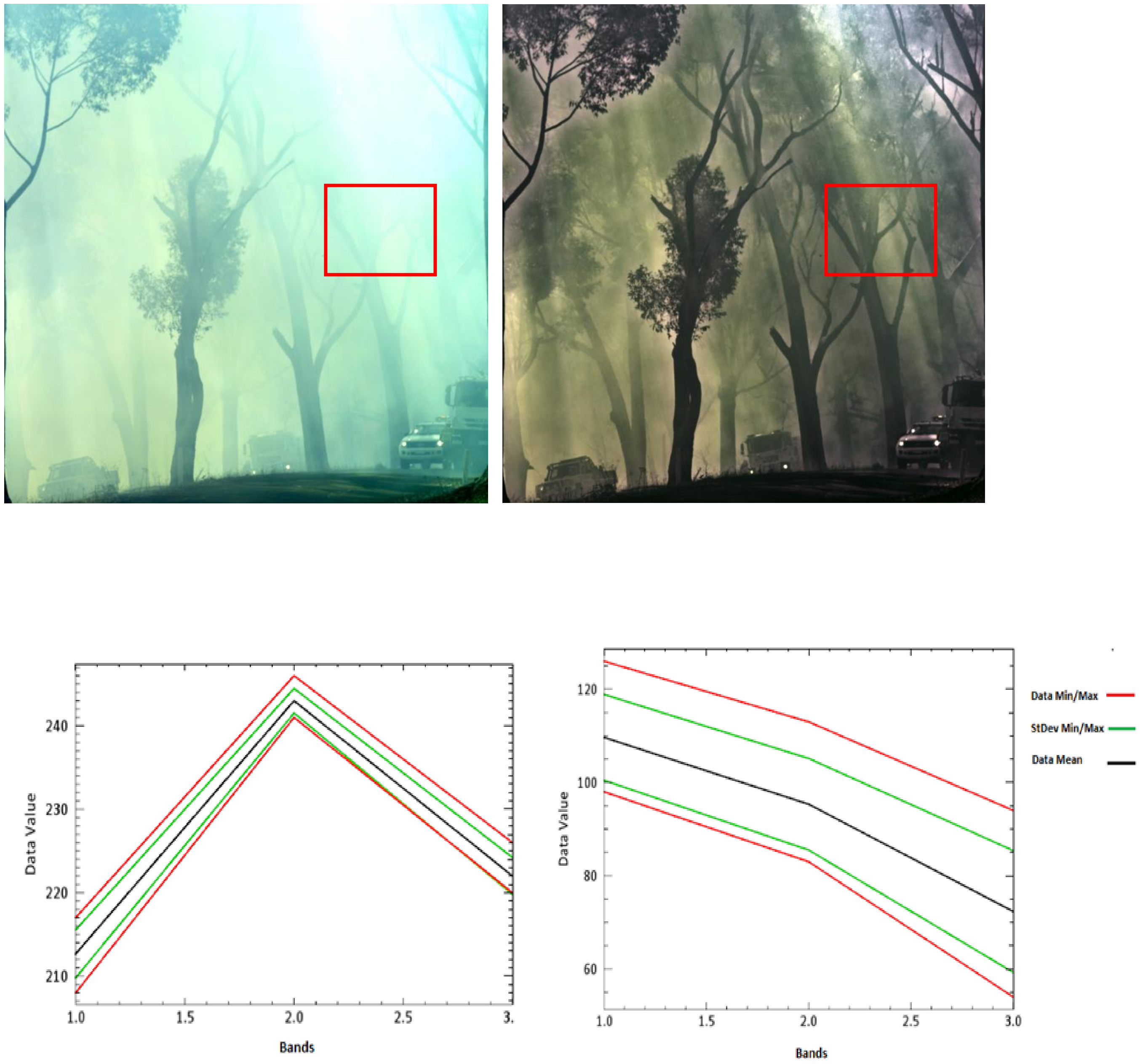

Figure 7.18. In the left-hand image the scene is mostly obscured by smoke. The right-hand image shows the scene after applying the SPA algorithm. DNs for all the pixels in the area highlighted in red on both images used were extracted to generate statistical summary for minimum, maximum, mean and standard deviation of average DNs, which are shown in the graphs below the images for the left-hand and right-hand images respectively. These graphs show improved discrimination in the image DNs after applying SPA.

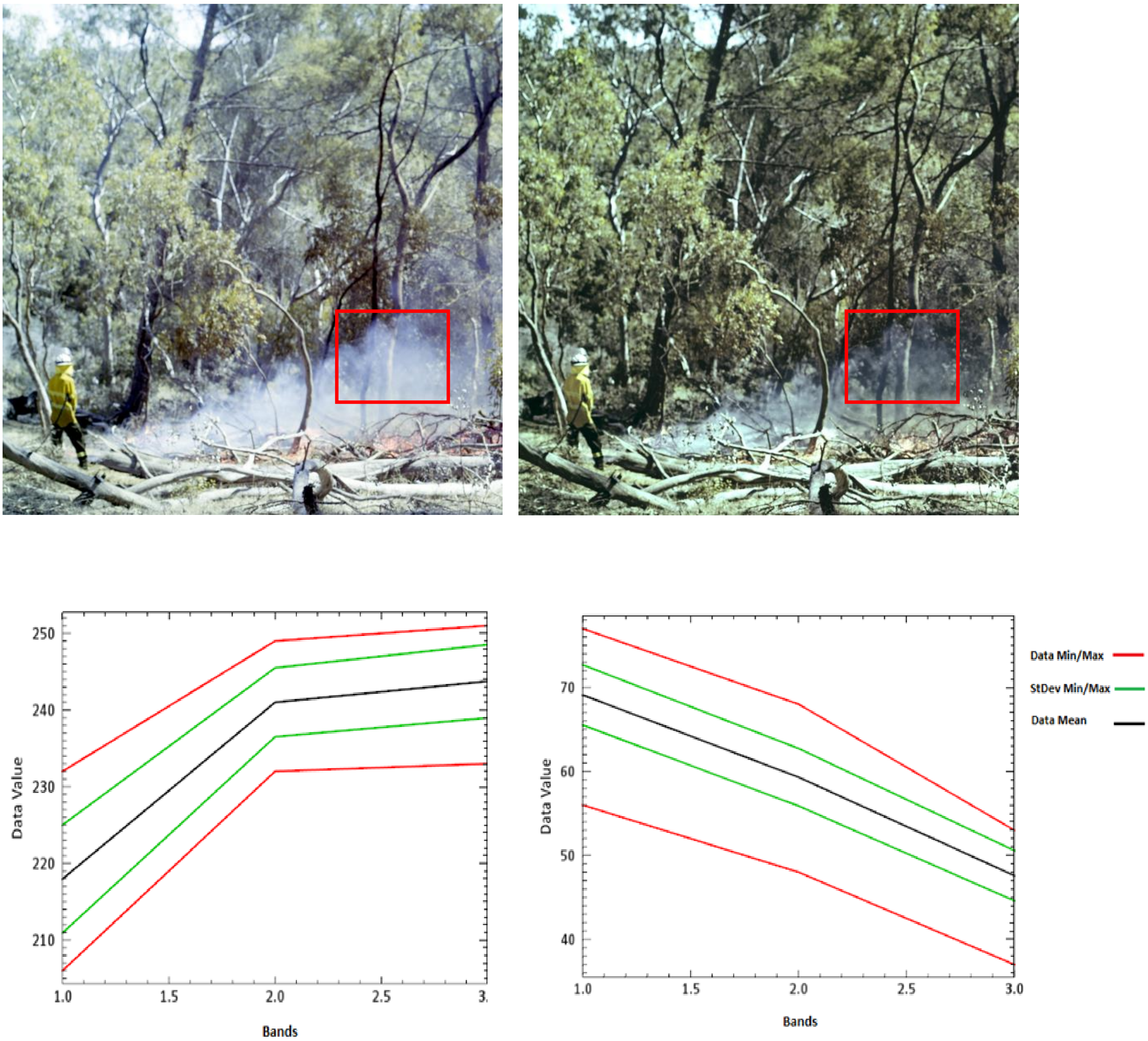

Figure 7.19. In the left-hand image the scene is partially obscured by smoke. The right-hand image shows the scene after applying the SPA algorithm. DNs for all the pixels in the area highlighted in red on both images used were extracted to generate statistical summary for minimum, maximum, mean and standard deviation of average DNs, which are shown in the graphs below the images for the left-hand and right-hand images respectively. These graphs show improved discrimination in the image DNs after applying SPA.

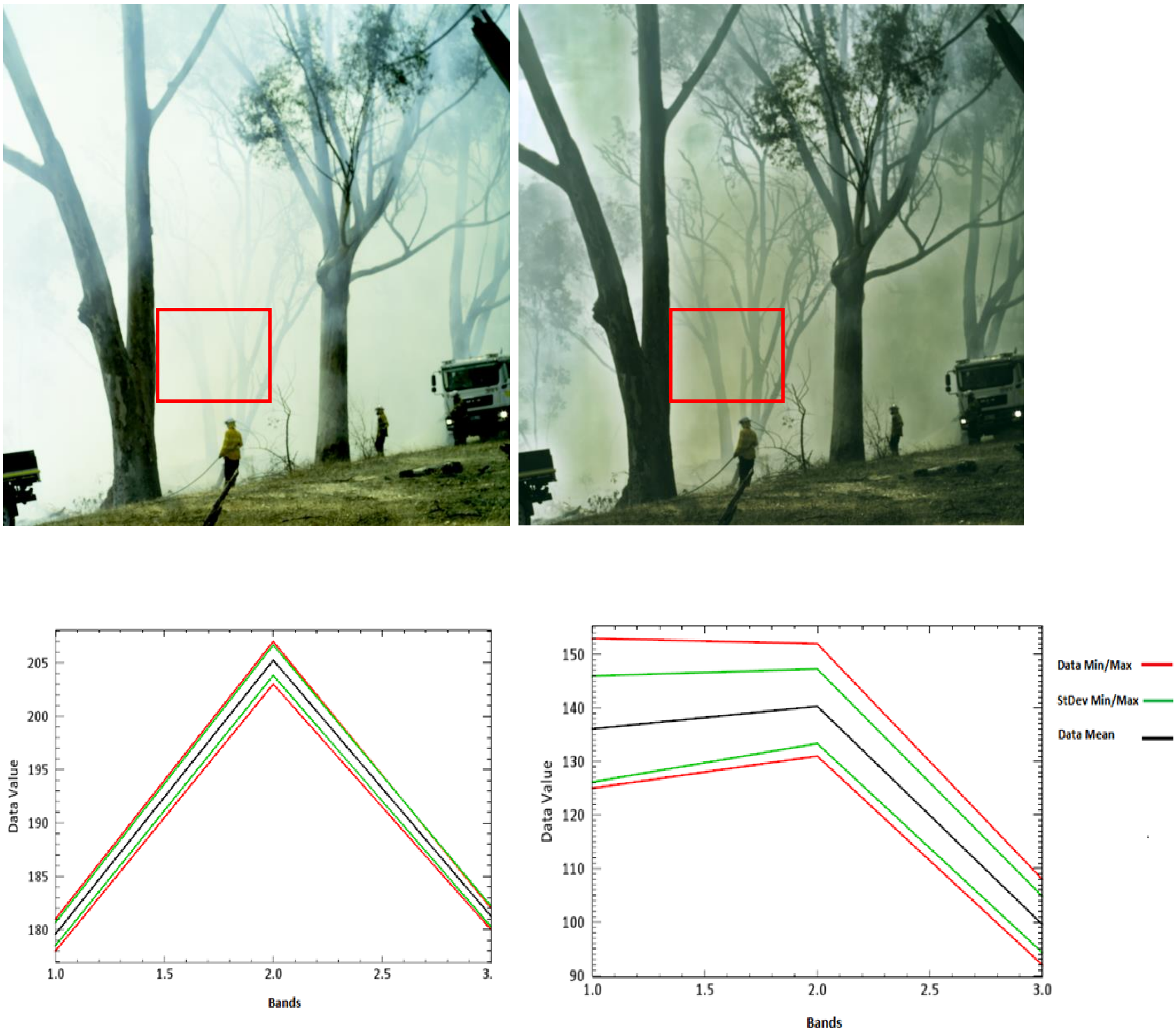

Figure 7.20. In the left-hand image the scene is mostly obscured by smoke. The right-hand image shows the scene after applying the SPA algorithm. DNs for all the pixels in the area highlighted in red on both images used were extracted to generate statistical summary for minimum, maximum, mean and standard deviation of average DNs, which are shown in the graphs below the images for the left-hand and right-hand images respectively. These graphs show improved discrimination in the image DNs after applying SPA

7.5. Chapter Summary

In this chapter, a novel technique, called the smoke penetration algorithm or SPA, was developed for enhancing scene visibility in the presence of smoke particles was developed based on improved dark channel prior method, which was proposed by He, Sun & Tang (2011). In this technique, blue and green channels are blended using a modified red channel. After applying colour balancing, the dark channel of the input image and atmospheric light are calculated, and a transmission map is estimated for image enhancement.

Two sets of data were used to evaluate the effectiveness of the SPA. One captured from a controlled burn using a 24 mega pixel modified DSLR camera and a custom-designed filter, and the other captured at 600 m altitude over a prescribed burn area using a 20 mpixel modified DSLR camera with the same custom-designed filter.

The SPA works effectively in improving scene visibility even in areas thickly covered by smoke particles; situations which normally would fail if previously proposed methods (Sections 2.6 – 2.7) were applied. As discussed in Section 5.3, smoke density and its distribution, distance of the camera from smoke particles and image resolution are important factors in successful scene visibility enhancement. The application of the SPA illustrated that if smoke particles are greater than the wavelength by a factor of > $\lambda/10$, then Mie and non-selective scattering come into play and, as a result of these types of scattering, the SPA does not provide significant improvements in visibility.

Chapter 8

Conclusions and Recommendations

8. Conclusions and Recommendations

8.1. Conclusions

As discussed in Chapter 1, smoke from bushfires can blanket areas up to hundreds of kilometres beyond a fire front depending on the severity of the fire, weather and terrain conditions. In general wind can spread dense smoke into a large volume of air which results in gaseous smoke and reduces visibility.

Advances in sensor development and remote sensing applications have enabled image capture in the EMS beyond visible light. The important point in the context of this research is that sensors with sensitivity to longer wavelengths are less prone to light scattering effect and as result can produce more clearer image data in areas covered by smoke particulates. Thermal sensors, as an example, collect radiated heat from objects with almost no effect from smoke particulates on the quality of the radiation detected. It was argued in this thesis that, although these sensors penetrate smoke, due to their relatively low spatial resolution and narrow fields of view, they cannot be utilized to detect small objects on the land surface. For example, using a thermal sensor to view through thick smoke layers and detecting fire flames makes them as extremely useful imaging tools for fire fighters but the monochromatic images that are produced would not be a preferred option if colour image interpretation is required. Similarly, if was flown over a relatively large area many images should be captured due to a small sensor footprint on the ground and often intensive post-processing and computer resources are required.

Therefore, the research reported in this thesis studied feasibility of utilizing a consumer-grade DSLR camera to penetrate smoke particulates without compromising spatial resolution and image colour as explained in Section 1.4. Three research was designed around three research questions:

7. Can images acquired by DSLR cameras, after modifications to full spectra, penetrate smoke? This question emanates from the first objective.

8. Is it feasible to design an optical filter to minimize the scattering effect on DSLR camera images without compromising true-colour? This question emanates from the second objective.
9. Can an image visibility enhancement algorithm be developed to improve smoke penetration from a modified camera setup? This question emanates from the third objective of this research.

The research literature on bushfire formation and development, combustion phases and fuel types were reviewed and followed by a review of smoke particle components and strategies for detecting them. Smoke particle size and characterization were likewise reviewed, and it was shown that incoming solar radiation can be partially scattered, absorbed or reflected with various magnitudes as a function of morphological and optical attributes of aerosols.

Low cost multi-spectral and TIR sensors are now available and deployable on small UAVs which can fly at low elevation and capture high-spatial resolution imagery without being affected by smoke particulates. However due to the narrow swath width of these sensors on the ground a large volume of raw imagery has to be captured to cover big areas and this requires powerful computing resources, experienced operators and specialized remote sensing software. Although with image processing methods such as pan-sharpening using a pair of high and low-spatial resolution images it is possible to enhance the quality of a low-resolution image (*cf.* section 2.6), these methods could fail if the high-spatial resolution image is covered by smoke.

Many researchers have worked on improving the clarity of images captured by a DSLR camera in hazy conditions (Section 2.7). These methods commonly are based on identifying parts of image with no or minimal haze contamination to estimate the haze density before attempting to enhance it. However, it is obvious that if there is no clean region in a captured image these methods will not effective. To address this, multiple image-based haze removal methods were reviewed (Section 2.8), these are based on utilizing NIR-sensitive cameras alongside normal consumer-grade colour cameras. These methods require very careful image positioning and co-registration prior to analysis, they can be very challenging to deploy and in practice are often very complicated to use.

A novel method based on a single and cost-effective consumer-grade camera to address these issues, as well as the main research problem as stated in Section 1.3, was designed, developed and executed – this includes the following elements:

- Modifying a consumer-grade DSLR using a reasonably well-known method;
- Designing and testing a custom-designed filter; and
- Developing a smoke penetration algorithm.

This method assumed that an image captured by a typical consumer-grade DSLR camera can potentially penetrate smoke. This assumption was simulated and verified using archive airborne hyperspectral, thermal and a consumer-grade camera imagery that had been simultaneously collected over an area covered by smoke from a bushfire (Section 4.2). Since the hyperspectral camera used for collecting these data was sensitive to EMR between 400 – 970 nm, which is almost same sensitivity range as a typical Silicon-based imaging sensor used in consumer-grade cameras, it was a valuable dataset to analyse and evaluate the feasibility of this research topic. Because of very high spectral resolution of these imagery (244 bands in the hyperspectral images), the light scattering effect and its impact on image visibility was analysed between 400 – 970 nm; and it was shown that by comparing the standard deviation of the reflectance values, significant improvements in image visibility and low reflectance were found at wavelengths > 950 nm. This confirmed that the first and second question posed for this research are valid; and that they could answered as follows.

A consumer-grade DSLR camera was modified to full spectra by removing its IR cut-off filter (Section 3.2.2). This modification enabled the three (red, green and blue) bands of the camera to capture NIR radiation. This caused a red appearance in the images captured because the blue, green and red bands are also sensitive for NIR exposure as illustrated in Figure 5.1. The image looks red because of spectrally mixed channels and difficulties in interpolation (Figure 5.2). To avoid this effect, a custom filter was designed that only allowed NIR radiation to be exposed in the red channel. It was shown that by transmitting NIR radiation between 950 – 1100 nm, as a replacement for the red band of the camera, the resulting images were less contaminated by NIR radiation and looked more natural (Figure 5.4). The custom-designed filter was then examined in a lab environment using a spectroradiometer and its performance and spectral response were confirmed (Section 5.3 and Appendix 1). For this test, a white panel with 100% reflectance and nine other materials (*cf.* Table 3.5) with various spectral response were used. The custom-designed filter spectral response test showed that using the filter absorbs EMR about 600 nm to 950 nm. Reflectance (transmission) starts to decrease dramatically at 584 nm (reflectance = 0.94). By 600 nm the transmission was dropped to 0.51 and by 615 nm dropped as low as 0.016. Beyond 950 nm transmission increased to 0.51 at 979 nm and 0.95 at 1007 nm. There was performance dip at λ = >1200 nm due to the physical characteristics of the custom-designed filter such as flatness or curvature of surface, the amount of polish and the quality of coating (Angus 2010, p. 646).

The spectral response of the modified camera and custom-filter combination was studied further in laboratory experimentation. To verify the spectral response of the modified camera and custom-designed filter, first the DN values of white, grey and black targets were measured using a FieldSpec4® Hi-Res ASD spectrometer. Then the modified camera with and without custom-designed filter was used to capture photographs from those targets respectively. Results from the spectrometer reading divided into three bins: 400 nm – 500 nm (blue), 500 nm – 600 nm (green), and 600 nm – 700 nm (red) bands. DN values from the spectrometer and camera readouts without custom-designed filter for each individual band were analysed and it was noticed that the R-square value of the DNs for red band is lower than that for green and blue bands without using the custom-designed filter (Figures 6.6). This linearity was significantly improved for red, green and blue bands after using the custom-designed filter confirming that DN values of the images captured by the modified camera and custom-designed filter can be compared and correlated to the DN values of the spectrometer (Figure 6.7).

To test the modified camera and custom-designed filter further a series of airborne and ground-based photos with smoke caused by a bushfire and controlled burn, the details of the fire environments and remote sensing methods are discussed in Section 3.3. Since the captured photographs contained NIR radiation between 950 – 1100 nm in the red band, this was used to develop a smoke penetration algorithm (SPA) to enhance the blue and green bands which were exposed more to smoke particulates.

The SPA is based on combination of both single and NIR-guided image haze reduction methods from the research literature (Chapter 2) and uses the dark channel prior concept. It first attempts to divide the input image into three separate bands, and then applies a blending operation by multiplying individual pixels of the blue and green bands with the corresponding pixels from the NIR (λ= 950 nm – 1100 nm) band. After applying colour balancing to the resulting image, dark pixels from small patches in the photographs are identified and used for smoke transmission mapping and path radiance estimation to enhance the image visibility. The results achieved after applying the SPA show significant improvements in visibility. Evidence for this comes from the DNs of both visual and statistical comparisons of selected regions of ‘test’ photographs, which was mostly covered by smoke, before and after applying the SPA.

The main limitation of this method, that was introduced in this research, is if entire or part of scene is covered by dense smoke there will be almost no visibility improvement in those areas. This is because in the areas of dense smoke, there are also larger diameter particles cause Mie and non-selective scattering. Mie scattering occurs when the diameter of the smoke particles is approximately the same as the incident wavelength. If EMR interacts with particles that are several times larger than the radiated wavelength, then Non-selective scattering occurs with strong forward scattering peak and smaller degree of backscattering (*cf.* section 2.5). In these cases (Mie or Non-selective scattering), imaging sensor does not receive the entire energy reflected from ground objects. In case of Rayleigh scattering in which the diameter of smoke particles is much smaller than incident light wavelength (<λ/10), camera sensor receives a portion of reflected energy from the ground objects and also from the molecular particles in the atmosphere. The proposed method in this research successfully estimated the reflected energy from smoke particles which is known as path radiance using the developed SPA (*cf.* section 7.3.2) and effectively enhanced the visibility of images captured using the modified camera and custom-designed filter combination.

To conclude, this research successfully answered the research questions that were asked based on identified research problem and research objectives were fulfilled. The key outcomes are:

1. Development of a custom-designed optical filter and a methodology for seeing through gaseous smoke using modified DSLR cameras which involved:

    a. Identification of the useful regions of the EM spectrum beyond visible wavelengths in DSLR camera sensors which effectively can penetrate smoke (i.e., > 950 nm).
    b. Preserving original image colour while transmitting NIR radiation > 950 nm.

2. Development of a smoke penetration algorithm to improve image visibility for images captured by a modified camera and custom-designed filter.

The proposed solution could be implemented in near real-time to enhance scene visibility as images are captured. For example, an unmanned aircraft equipped with this camera and filter, can transmit data to the ground station to be processed with SPA to enable decision makers to provide clear, high-resolution insights in fire environments.

The results from this study could potentially be used to design a low-cost smoke penetration sensor onboard a UAV. Small and lightweight optical cameras can be easily modified at relatively low cost to be exposed by EMR beyond the visible spectrum. Then, by using the custom-designed filter introduced in this research, collected imagery can be transmitted to a remote ground base station through a UAV’s built-in wireless communication protocol. Since the developed smoke penetration algorithm does not require huge computing resources, a typical transportable field computer can be used to run the developed algorithm on received imagery and provide cleaner vision to people who need it in near real-time.

The proposed approach in this research can be improved in number of ways. First, further analysis can be carried out on designing an optical filter to use wider spectral bands of the CMOS sensors in the NIR region, i.e. not limited to 950 nm – 1100 nm. Due to the limited budget for this research only a single custom optical filter was designed and examined, which was discussed in detail in Chapter 5. Other optical filters with wider bandwidths in the NIR region of the spectrum, 850 nm – 1100 nm, would potentially provide more information about the scene and smoke particles. A wider bandwidth can only be more efficient if maximum information can be transmitted over it. The term spectral efficiency is used to describe the rate of information being transmitted over a given bandwidth. Therefore, selecting any other camera and studying spectral response of its imaging sensor, especially in the NIR region, would have a significant impact on achieving improved results. Secondly, due to the lack of precise spectral analysis equipment available for this research such as a monochromator, it was impossible to measure the quantum efficiency of the camera sensors used in this research. CCD or CMOS sensors inside DSLR cameras have various quantum efficiencies which can be measured using a monochromator at any given spectral region. This would help in selecting a more suitable camera with higher spectral response in the NIR region. Thirdly, although the SPA algorithm developed in this research, which was adopted from the DOS method in remote sensing and proven to be providing promising results in seeing through smoke, as illustrated in Chapter 7, it can be replaced with any other remote sensing atmospheric correction algorithm. This is because of the fact that nature of the collected images using the modified DSLR camera and custom-designed filter contains extra per-pixel information in the NIR band with minimal smoke particle scattering effect, so other atmospheric correction algorithms in remote sensing and image processing literature could be adopted and examined for removing smoke particle effects.

8.2. Contribution to the body of knowledge

The significant original contribution to the body of knowledge in this thesis emerges from the topic and research area itself as a novel application of existing solutions. This has been accomplished by creating a synthesis, discussing previous work and providing a single original technique to tackle the identified research problem. The methods discussed in this thesis also contribute to the body of knowledge. Although there were other previous studies partially related to this research, such as implementing thermal or multispectral imaging technologies in addressing the research problem, this research introduced a novel methodology by taking a closer and more precise look at CMOS imaging sensors used widely in a consumer-grade cameras which was not previously studied in the context of this topic. Data collection method, deeper analysis and design logic for a custom spectral filter, combined with adopting known image processing methods, makes this research and its contribution to the knowledge even more outstanding.

The ability to solve a challenging issue in this research, which is a trending problem in bushfire literature, a result-oriented approach built round a valid hypothesis add to existing knowledge on the research topic. This research contributes to bushfire management, particularly in minimizing the risks to fire fighters and other people even in prescribed burn scenarios; as background visibility for firefighters is crucial in fire management. The findings of this research will contribute significantly when aerial or ground-based high resolution imagery with minimal smoke obstruction can be collected and made available in near real-time for fire fighters and rescue teams.

Finally, as discussed and illustrated in Chapter 4, the presence of smoke particles in collected aerial imagery causes image matching and pixel correlation algorithms to fail or produce non-reliable results. There are no previous studies on this specific topic, nor on how stereo imagery collected above smoke contaminated regions could be used for photogrammetry and topographic data production. Access to up-to-date elevation data in fire management to estimate ground slope, tree heights and other information is an invaluable source of information. These data cannot be produced using thermal imagery because of their low spatial resolution and a monochromic imaging sensor as discussed in Chapter 4. However, collecting imagery using a typical optical sensor over a smoke-affected area would specifically result in incorrect and less reliable elevation data as a result of this poor stereo image matching. The results of this research therefore also contribute to photogrammetry domain; specifically how the data could be implemented and optimized to produce reliable elevation data and large area image mosaics.

8.3. Recommendations

Identified directions for further investigation in improving and conducting follow up research include:

- *Improved image contrast after applying SPA.* After applying SPA resulting images may appear darker than the initial input images. This can be managed and maintained by applying colour mapping and histogram matching algorithms based on statistics of two images or pixel-based colour mapping by developing an adaptive colour correction filter.

- *Real-time visibility improvement in bad weather conditions and road sign detection.* Results from this research show that haze particles can be effectively removed from input imagery, this could be extended to develop a real-time haze and fog removal solution to assist drivers in detecting road signs, people, traffic lights and potential roadside hazards.

- *Improving efficiency of image matching tools by removing haze and smoke from airborne imagery.* To study large areas of interest in airborne remote sensing, image mosaicking tools are commonly used for stitching individual images together based on corrleation between common pixels and image matching between two or more overlapping images for constructing the digital surface model (DSM) required for image ortho-rectification process. This would simply fail or result in gap in the final mosaicked image if images are degraded by haze or smoke particles. Outcomes of this research can be applied for improving image matching techniques and noise-free 3D reconstruction in photogrammetry.

- *Deriving soil properties and qualities using images collected by the proposed camera and filter in this research.* It was illustrated that the modified camera and custom-designed filter have acceptable spectral reflectance in infrared region of spectrum with 950 nm< λ<1100 nm. This narrow range of wavelengths, combined with blue and green channels, could provide reasonably acceptable reflectance indices which can be used for studying soil properties for agricultural studies.

9. References

Aiger D., Mitra N.J., Cohen-Or D. 2008, '4-Points congruent sets for robust pairwise surface registration', *ACM SIGGRAPH 2008 Papers*. *ACM; Los Angeles, CA, USA*, pp. 1–10.

Allison S.R., Johnston M.J,Craig M., Jennings S., 2016, 'Airborne Optical and Thermal Remote Sensing for Wildfire Detection and Monitoring’, *Sensors*, no.16, p.1310.

Ambrosia V.G., Wegener S., Zajkowski T., Sullivan D.V., Buechel S., Enomoto F., Lobitz B., Johan S., Brass J., Hinkley, E., 2011, 'The Ikhana unmanned airborne system (UAS) western states fire imaging missions: From concept to reality (2006–2010)', *Geocarto Int.*, no. 26, pp. 85–101.

Andreae M.O., Merlet P., 2001, *'Emission of trace gases and aerosols from biomass burning'*, Glob Biogeochem Cycles, no. 15, pp. 955–66.

Angus MacLeod H. 2010, *Thin Film Optical Filters-Fourth Edition*, CRC Press, Boca Raton FL. USA.

Arrue B.C., Ollero A., De Dios J.,2000, 'An intelligent system for false alarm reduction in infrared forest-fire detection', *IEEE Intell. Syst. Appl*., vol.15, no.3, pp. 64-73.

Asbach C., Fissan H., Stahlmecke B., Kuhlbusch T.A.J., Pui D.Y.H., 2009, 'Conceptual limitation and extensions of lung-deposited Nanoparticle Surface Area Monitor (NSAM)', *J. Nanoparticle Res.*, no. 11, pp. 101–109.

Banu T.P., Borlea G.F., Banu C., 2016, 'The Use of Drones in Forestry', *Journal of Environmental Science and Engineering*, no. 5, pp. 557–562.

Bentham 1997, *A Guide For Spectroradiometry Instruments & Applications for the UltraViolet-Issues 2*, Bentham Instruments Ltd. UK, viewed 10 October 2015, <http://www.wonwoosystem.co.kr/pic/catalog/UVGuide.pdf >.

Berie H.T., Burud I., 2018, 'Application of unmanned aerial vehicles in earth resources monitoring: focus on evaluating potentials for forest monitoring in Ethiopia', *EUROPEAN JOURNAL OF REMOTE SENSING*, vol. 51, no. 1, pp. 326–335.

Blong, R. 2005, ‘Natural hazards risk assessment—An Australian perspective’. *Issues in Risk Science 4*, Benfield Hazard Research Centre, London.

Bond W.J., Woodward F. I., Midgley G. F. 2004, *‘The global distribution of ecosystems in a world without fire*’, New Phytologist, no. 165, pp. 525–538.

Bowman D. 2005, *‘Understanding a flammable planet – climate, fire and global vegetation patterns’*, New Phytologist, no. 165, pp. 341–345.

Bucholtz A. 1995, ‘*Rayleigh-scattering calculations for the terrestrial atmosphere*’, Applied Optics, vol. 34, no. 15, pp. 2765–2773.

BWTek n.d., *Spectrometer Knowledge*, USA, viewed 10 August 2015, <http://bwtek.com/spectrometer-part-3a-the-detector/>.

Campbell J.B., Wynne R.H. 2011, *Introduction to Remote Sensing, Fifth Edition*, Guilford Press, NYC, USA.

Çetin A.E., Dimitropoulos K., Gouverneur B., Grammalidis N., Günay O., Habiboglu Y.H., Töreyin, B.U.,Verstockt S.,2013, 'Video fire detection—Review', *Digit. Signal Process*., no. 23, pp. 1827–1843.

CFS 2015, *Bushfire History*, viewed 2 April 2016, <http://www.cfs.sa.gov.au/site/about/history/bushfire_history.jsp>.

CFS n.d., *Burning-off*, Adelaide, viewed 14 February 2016, < http://www.cfs.sa.gov.au/site/fire_safety/farm_fire_safety/burning_off.jsp>.

Chabok M., 2013, ‘Eliminating and Modelling Non-metric Camera Sensor Distortions Caused by Sidewise and Forward Motion of the UAV’, *ISPRS - International Archives of the Photogrammetry, Remote Sensing and Spatial Information Sciences*, vol. XL-1/W2, pp.73-79.

Chabok M., Millington A., Hacker J.M, McGrath A.J 2016, ‘*Visibility through the gaseous smoke in airborne remote sensing using a DSLR camera’*, Proc. SPIE, Fourth International Conference on Remote Sensing and Geoinformation of the Environment (RSCy2016), vol. 9688.

Chavez P. 1988, ‘An improved dark-object subtraction technique for atmospheric scattering correction of multispectral data’, *Remote Sensing of Environment*, vol. 24, pp. 450–479.

Chelsea E.S, Thilina J., Mark A.C., Kevin C.R, Erianto I.P., Bambang H.S., Ati D.N., Israr A., Donald R.B., Isobel J.S., Elizabeth A.S., Robert J.Y. 2016, *‘Field measurements of trace gases and aerosols emitted by peat fires in Central Kalimantan, Indonesia, during the 2015 El Niño’*, Atmos. Chem. Phys., no. 16, pp. 11711–11732.

Cheremkhin P.A, Lesnichii V.V, Petrov N.V 2014, ‘*Use of spectral characteristics of DSLR cameras with Bayer filter sensors*’, Journal of Physics, vol. 536, no. 1.

Chrysoulakis N.,Herlin I.,Prastacos P., Yahia H., Grazzini J., Cartalis C., 2007, 'An improved algorithm for the detection of plumes caused by natural or technological hazards using AVHRR imagery', *Remote Sens Environ.* ,no. 108, pp. 393–406.

Colarivision 2017, *DIY Infrared Conversion*, viewed 26 January 2017, https://kolarivision.com/diy-infrared-conversion/nikon-d70-infrared-conversion-tutorial/>.

Colomina I., Molina P., 2014, 'Unmanned aerial systems for photogrammetry and remote sensing: A review', *ISPRS Journal of Photogrammetry and Remote Sensing*, no. 92, pp. 9–97.

Connelly N.G., Geiger W.E., 1996, *'Chemical Redox Agents for Organometallic Chemistry'*, Chemical Reviews, no.2, pp. 877–910.

Crutzen P.J., Andreae M.O., 1990, *'Biomass burning in the tropics: impact on atmospheric chemistry and biogeochemical cycles'*, Science, no. 250, pp. 1669–1678.

Cruz M.G.,Gould J.S.,Hollis J.J, McCaw W.L.,2018, *'Hierarchical Classification of Wildland Fire Fuels for Australian Vegetation Types'*, fire2018, vol 1. no.13

Chrysoulakis N., Opie C., 2004, 'Using NOAA and FY imagery to track plumes caused by the 2003 bombing of Baghdad', *Int. J. Remote Sens.*, no.25, pp. 5247–5254.

Chun F., Jian-wen M., Qin D., Xue C., 2004, 'An improved method for cloud removal in ASTER data change detection', *in Proc. 2004 IEEE Int. Geosci. Remote Sens. Symp.*, vol. 5, pp. 3387–3389.

Corbitt RA, 1989, Standard handbook of environmental engineering. *McGraw-HiII*, New York, USA.

CTI Reviews 2016, *Astronomy, Physical Perspective*, Cram101 Textbook Reviews, NYC, USA.

Darmont Arnaud 2009, ‘Spectral Response of Silicon Image Sensors’, viewed 1 April 2014, < http://www.aphesa.com/downloads/download2.php?id=1>.

Delichatsios M.A., 2005, *'Piloted ignition times, critical heat fluxes and mass loss rates at reduced oxygen atmospheres'*, Fire Safety Journal, no. 40, pp.197–212.

Dennekamp M, Abramson MJ. 2011, ‘The effects of bushfire smoke on respiratory health’, Respirology, vol.16, no. 2, pp. 198-209.

Drysdale D., 2011, An Introduction to Fire Dynamics, 3rd ed. *Wiley*, UK.

Duff T.,Keane R.,Penman T.,Tolhurs K., 2017, *'Revisiting Wildland Fire Fuel Quantification Methods: The Challenge of Understanding a Dynamic, Biotic Entity'*, Forests, vol. 8, no.9, p.351

Du Y., Guindon B., Cihlar J., 2002, 'Haze detection and removal in high resolution satellite image with wavelet analysis', *IEEE Trans. Geosci. Remote Sens*., vol. 40, no. 1, pp. 210–217.

Edmund n.d., *Imaging Electronics 101: Understanding Camera Sensors for Machine Vision Applications*, EdmundOptics, Australia, viewed 8 May 2015, < https://www.edmundoptics.com.au/resources/application-notes/imaging/imaging-electronics-101-understanding-camera-sensors-for-machine-vision-applications/>.

Elvidge C.D, Keith D.M, Tuttle B.T, Baugh K.E 2010, ‘*Spectral Identification of Lighting Type and Character*’, Sensors 2010, vol. 10, pp. 3961-3988.

Fattal R. 2008, ‘Single image dehazing’, *ACM Trans. Graph.*, vol. 27, no. 3, p. 72.

Fateh T., Rogaume T., Luche J., Richard F., Jabouille F., 2014, *'Characterization of the thermal decomposition of two kinds ofplywood with a cone calorimeter—FTIR apparatus'*, Journal of Anal Appl Pyrol, no. 107, pp.87–100.

Feng C., Zhuo S., Zhang X., Shen L., Susstrunk S. 2013, ‘Near-infrared guided colour image dehazing’, *2013 IEEE International Conference on Image Processing*, pp. 2363-2367.

Fowler A., Boyd & El Gamal, Abbas & Yang, Dave & Tian, Hui., 1999, ‘*A Method for Estimating Quantum Efficiency for CMOS Image Sensors’*, Proceedings of SPIE - The International Society for Optical Engineering.

Fromm M.,Alfred J.,Hoppel K.,Hornstein J., Bevilacqua R., Shettle E.,Servranckx R.,Stocks B., 2000, *'Observations of boreal forest fire smoke in the stratosphere by Poam III, Sage II, and Lidar in 1998'*, Geophys. Res. Lett., no. 27, pp. 1407–1410.

Gade R., Moeslund T.B., 2014, 'Thermal cameras and applications: a survey', *Mach. Vis. Appl*., vol. 25, no.1, pp. 245–262.

Gann Richard, Friedman Raymond, 2013, *Principles of Fire Behaviour and Combustion*, Jones & Bartlett Learning, Burlington, USA.

Giannakaki E., van Zyl P., Müller D., Balis D., Komppula M., 2016, 'Optical and microphysical characterization of aerosol layers over South Africa by means of multi-wavelength depolarization and Raman lidar measurements', *Atmos. Chem. Phys*., no. 16, pp. 8109–8123.

Giglio L., van der Werf G. R., Randerson J. T., Collatz G. J., Kasibhatla, P., 2006, *‘Global estimation of burned area using MODIS active fire observations’,* Atmospheric Chemistry and Physics, no. 6, pp. 957–974.

Goldstein, E.B. 2009, *Sensation and Perception*, Wadsworth, Belmont, CA.

Golowczynski Matt 2016, *Digital Camera Sensor Explained*, Time Inc., viewed 26 January 2017, <http://www.whatdigitalcamera.com/technical-guides/technology-guides/sensors-explained-11457>.

Gong P., Pu R.L., Li Z.Q., Scarborough J., Clinton N., Levien L.M., 2006, 'An integrated approach to wildland fire mapping of California, USA using NOAA/AVHRR data', *Photogramm. Eng. Remote Sens.*, no. 72, pp. 139–150.

Guindon, B.; Zhang, Y. 2002, ‘Robust haze reduction: An integral processing component in satellite-based land cover mapping’, *ISPRS Commission IV*, Symposium 2002, viewed 10 May 2013, < http://www.isprs.org/proceedings/XXXIV/part4/pdfpapers/252.pdf >.

Hamamatsu Photonics K.K 2015, InGaAs Photodiodes, viewed 8 May 2015, < https://www.hamamatsu.com/resources/pdf/ssd/ingaas_kird0005e.pdf >.

Hao L. Q., Romakkaniemi S., Kortelainen A., Jaatinen A., Portin H., Miettinen P., Komppula M., Leskinen A., Virtanen A., Smith J. N., Sueper D., Worsnop D. R., Lehtinen K. E. J., Laaksonen A., 2013, ‘Aerosol Chemical Composition in Cloud Events by High Resolution Time-of-Flight Aerosol Mass Spectrometry’, *Environ. Sci. Technol.*, no.47, pp. 2645–2653.

Hadjimitsis D.G., Papadavid1 G., Agapiou1 A., Themistocleous1 K., Hadjimitsis1 M. G., Retalis A., Michaelides S., Chrysoulakis N., Toulios L., Clayton C.R.I., 2010, 'Atmospheric correction for satellite remotely sensed data intendedfor agricultural applications: impact on vegetation indices', 2010, *Nat. Hazards Earth Syst. Sci*., no. 10, pp. 89–95.

Haseli, Y., van Oijen, J.A., H de Goey, L.P. 2012. ‘Analytical solutions for prediction of the ignition time of wood particles based on a time and space integral method’, Thermochim. Acta, no. 548, pp. 65–75.

He K., Sun J., Tang X. 2011, ‘Single image haze removal using dark channel prior’, *IEEE Transactions on Pattern Analysis and Machine Intelligence*, vol. 33, no. 12, pp. 2341–2353.

Heaton E.A., Flavell R.B., Mascia P.N., Thomas S.R., Dohleman F.G., Long S.P., 2008, *‘Herbaceous energy crop development: recent progress and future prospects.’*, Current Opinion in Biotechnology, no. 19, pp.202-209.

Hinkley E.A., Zajkowski T., 2011, 'USDA forest service-NASA: Unmanned aerial systems demonstrations-pushing the leading edge in fire mapping', *Geocarto Int*., no. 26, pp. 103–111.

Hungate W.S, Watkins R., Borengasse M. 2007, Hyperspectral Remote Sensing, *CRC Press*, Boca Raton FL. USA.

Hyde Joshua C., Yedinak Kara M., Talhelm Alan F., Smith Alistair M.S., Bowman David M.J.S., Johnston Fay H., Lahm Peter, Fitch Mark, Tinkham Wade T., 2017, *'Air quality policy and fire management responses addressing smoke from wildland fires in the United States and Australia.'*, International Journal of Wildland Fire, no. 26, pp.347–363.

Jacqueline Lenoble, Lorraine Remer, Didier Tanre (ed.) 2013, *Aerosol Remote Sensing*, Springer Berlin Heidelberg, Berlin.

Jakovcevic T., Stipanicev D., Krstinic D.,2013, 'Visual spatial-context based wildfire smoke sensor', *Mach. Vis. Appl*., vol.24, no.4, pp. 707-719.

Jiang J, Liu D, Gu J, Süsstrunk S. 2013, ‘What is the space of spectral sensitivity functions for digital colour cameras?’, *IEEE Workshop on the Applications of Computer Vision(WACV)*‘,Tampa, FL, pp. 168–179.

John W., 2011, Aerosol Measurement Principles Techniques and Applications 4th ed., *Wiley*, Hoboken, NJ, USA.

Jones A.R., 1999, 'Light scattering for particle characterization', *Progress in Energy and Combustion Science*, no. 25, pp. 1–53.

Joseph G. 2015, *Fundamental of Remote Sensing*, University Press, India.

Kaplan Herbert 2007, *Practical Applications of Infrared Thermal Sensing and Imaging Equipment*, SPIE Press, Bellingham, Washington, USA.

Kaufman Y.J., Kleidman R.G., King M.D., 1998, 'SCAR-B fires in the tropics: Properties and remote sensing from EOS-MODIS', *J. Geophys. Res. Atmos*., no. 103, pp. 31955–31968.

Kipnis N. 1991, *History of the Principle of Interference of Light*, Birkhäuser Verlag, Basel, Boston, Berlin.

Klusek C., Manickavasagam S., Menguc M.P., 2003, 'Compendium of scattering matrix element profiles for soot agglomerates', *J. Quant. Spectrosc Radiat Transfer*, pp. 839-859.

Ko B., Park J., Nam J.Y., 2013, 'Spatiotemporal bag-of-features for early wildfire smoke detection', *Image Vis. Comput*., vol.31, no.10, pp. 786-795.

Kouimtzis C., Samara T., 1995, *Airborne Particulate Matter,* Springer, NYC, US.

Levin N., Ben-Dor E., Singer A. 2005, ‘A digital camera as a tool to measure colour indices and related properties of sandy soils in semi-arid environments’, *International Journal of Remote Sensing*, vol. 26, pp. 5475–5492.

Liang J., Ren L., Ju H., Zhang W., Qu E. 2015., ‘Polarimetric dehazing method for dense haze removal based on distribution analysis of angle of polarization’, *Optics Express*, vol. 23, no. 20, pp. 26146–26157.

Li Z.Q.,Khananian A.,Fraser R.H.,Cihlar J., 2001, 'Automatic detection of fire smoke using artificial neural networks and threshold approaches applied to AVHRR imagery', *IEEE. Trans. Geosci. Remote Sens.*, no. 39, pp. 1859–1870.

Lillesand T., Kiefe RW., Chipman J. 2015, *Remote Sensing and Image Interpretation, 7th Edition,* John Wiley & Sons, Hoboken, New Jersey, USA.

Liu C., Hu J., Lin Y., Huang S.W., Huang W. 2011, ‘Haze detection, perfection and removal for high spatial resolution satellite imagery’, *International Journal of Remote Sensing*, vol. *32,* pp. 8685–8697.

Liu C.C.,Kuo Y.C.,Chen C.W., 2013, 'Emergency responses to natural disasters using formosat-2 high-spatiotemporal-resolution imagery', *Forest fires. Nat. Hazards*, no.66, pp.1037–1057.

Liu L., Mishchenko M.I., 2005, 'Effects of aggregation on scattering and radiative properties of soot aerosols', *J. Geophys Res*., no.110, p.1211

Long J., Shi Z.W., Tang W., Zhang C.S. 2014, ‘Single remote sensing image dehazing’, *IEEE Geoscience and Remote Sensing*, vol. 11, pp. 59–63.

Lowe D.G., 1999, *'Object recognition from local scale-invariant features'* ,In Proceedings of the 7th International Conference on Computer Vision, pages 1150–1157.

Lyon R.E., Quintere J.G, 2007, *'Criteria for piloted ignition of combustible solids'*, Combust Flame, no.151, pp. 551–559.

Lyons W.A.,Nelson T.E.,Williams E.R.,Cramer J. A.,Turner T. R.,1998, *'Enhanced positive cloud-to-ground lightning in thunderstorms ingesting smoke from fires'*, Science, vol.282, no.5386, pp.77–80.

Makarau A., Richter R., Muller R., Reinartz P.,2014, 'Haze detection and removal in remotely sensed multispectral imagery', 2014, *IEEE Trans. Geosci. Remote Sens*., vol. 52, no. 9, pp. 5895–5905.

Madsen C.K., Zhao J.H. 1999, *Optical Filter Design and Analysis: A Signal Processing Approach*, John Wiley & Sons, Hoboken, New Jersey, USA.

Mangold K., Shaw J.A., Vollmer M. 2013, ‘The physics of near-infrared photography’, *European Journal of Physics*, vol. 34, no. 6, pp. 51–71.

Manickavasagam S., Menguc M.P., 19979, 'Scattering matrix elements of fractal-like soot agglomerates', *Appl Opt*, vol.36, no.6, pp. 1337–1351.

Manigrasso M., Stabile L., Avino P., Buonanno G., 2013, 'Influence of measurement frequency on the evaluation of short-term dose of sub-micrometric particles during indoor and outdoor generation events', *Atmos. Environ*., no.67, pp.130–142.

Martinez-de Dios J.R., Arrue B.C., Ollero A., Merino L., Gómez-Rodríguez F., 2008, 'Computer vision techniques for forest fire perception', *Image Vis. Comput*., vol. 26, no.14, pp. 550–562.

Mather P.M., Koch M. 2010, *Computer Processing of Remotely-Sensed Images: An Introduction, Fourth Edition*, John Wiley & Sons, Hoboken, New Jersey, USA.

Maynard A.D., Kuempl E.M, 2005, 'Airborne nanostructured particles and occupational health', *J. Nanoparticle Res*., no.7, pp.587–614.

Maynard A.D., Aitken R.J., Butz T., Colvin V., Donaldson K., Oberdörster G., Philbert M.A., Ryan, J., Seaton A., Stone V., 2006, 'Safe Handling of Nanotechnology', *Nature*, no.44, pp. 267–269.

McAllister S., 2013, *'Critical mass flux for flaming ignition of wet wood'*, Fire Safety Journal, no.61, pp. 200–206.

MCGRATTAN K., KLEIN B., HOSTIKKA S., FLOYD J., 2009, *Fire Dynamics Simulator (Version 5.3) - User's Guide.* National Institute of Standard and Technology ,Washington DC USA.

Mishchenko M.I., Travis L.D., Lacis A.A., 2002, *Scattering, absorption, and emission of light by small particles*, Cambridge University Press, Cambridge, UK.

Morvan D., Méradji S., Accary G.,2008, ‘Physical modelling of fire spread in Grasslands.’, *Fire Safety Journal*, vol. 44, no. 1, pp. 50–61.

Narasimhan S., Nayar S., ‘Vision and the atmosphere’, *International Journal of Computer Vision*, vol. 48, no. 3, pp. 233–254.

Norton A.J. 2000, *Dynamic Fields of Waves*, CRC Press, Boca Raton FL. USA.

NWCG SmoC 2014, *Wildland fire personnel transportation safety guidebook. National Wildfire Coordination Group Smoke Committee and University of Idaho*, viewed 1 March 2018, < https://www.frames.gov/download_file/view/3373/2114/>.

Ollero A., 2011, 'An Unmanned Aircraft System for Automatic Forest Fire Monitoring and Measurement', *J. Intell. Robot. Syst*., no.65, pp.533–548.

OnSemi 2015, *Image Sensor Colour Correction*, ON Semiconductors, viewed 20 April 2016, < http://www.onsemi.com/pub/Collateral/TND6114-D.PDF>.

Paysen Timothy, Ansley R.J., Brown J., Gottfried G., Haase S., Harrington M.,Narog M.,Sackett S.,Wilson R., 2000, 'Fire in Western Shrubland, Woodland, and Grassland Ecosystems', *USDA Forest Service Gen.Tech.Rep.RMRS-GTR-42*, vol. 2

Pohl C., Genderen J.V. 2016, *Remote Sensing Image Fusion: A Practical Guide,* CRC Press, Boca Rotan, FL. USA.

Poujol J., Aguilera C., Danos E., Vintimilla B., Toledo R., Sappa A.D. 2015, ‘Visible-Thermal Fusion based Monocular Visual Odometry’, *In Robot*, vol. 1, pp. 517–528.

Prabhat Prashant n.d., *Measurement of Optical Filter Spectra*, IDEX Corporation, viewed 20 July 2015,<https://www.semrock.com/Data/Sites/1/semrockpdfs/whitepaper_measurementofopticalfilter spectra.pdf >.

Porterie B.,Consalvi JL.,Loraud JC.,Giroud F.,Picard C.,2007, *'Dynamics of wildland fires and their impact on structures'*, Combust Flame, no.149, pp.314–328.

Qiyuan Xie, Heping Zhang, Yutian Wan, Yongming Zhang, Lifeng Qiao, 2007, 'Characteristics of light scattering by smoke particles based on spheroid models', *Journal of Quantitative Spectroscopy and Radiative Transfer*, vol. 107, no.1, pp. 72-82.

Qiyuan Xie, Hongyong Yuan, Liwei Song, 2007, 'Experimental studies on time-dependent size distributions of smoke particles of standard test fires', *Build Environ*, no. 42, pp. 640-646.

Rabatel G. Gorretta N., Labbe S. 2011, ‘Getting NDVI Spectral Bands from a Single Standard RGB Digital Camera: A Methodological Approach’, *CAEPIA 2011: Advances in Artificial Intelligence, La Laguna, Spain, 7–11 November 2011*, pp. 333–342.

Raman C.V., 1928, 'A new radiation', *Indian J. Phys*., no.2, pp. 387–398.

Rein G., 2016, *'Ssmouldering Combustion'*, SFPE Handbook of Fire Protection Engineering Chapter 19, no. 5, pp. 581-603.

Richter R., 1996, 'Atmospheric correction of satellite data with haze removal including a haze/clear transition region', *Comput. Geosci*., vol. 22, no. 6, pp. 675–681.

Rodriguez G., Pardo I., Olmo C., Rigol S. 2011, ‘Increasing the spatial resolution of thermal infrared images using cokriging’, *Procedia Environmental Sciences*, vol. 3, pp.117–122.

Rudin, L. I., Osher S., Fatemi E., 1992. ‘Nonlinear total variation based noise removal algorithms’, *Physica D*, vol. 60, no. 1-4, pp. 259–268.

Sabins, F.F. 1996, *Remote Sensing: Principles and Interpretation. 3rd Edition*, W. H. Freeman and Company, New York.

Sakamoto T., Gitelson A.A., Nguy-Robertson A.L., Arkebauer T.J., Wardlow B.D., Suyker, A.E., Verma S.B. 2012, ‘An alternative method using digital cameras for continuous monitoring of crop status’, *Agricultural and Forest Meteorology*, vol. 154-155, pp. 113–126.

San-Miguel-Ayanz J.,Ravail, N.,Kelha V.,Ollero A., 2005, 'Active fire detection for fire emergency management: Potential and limitations for the operational use of remote sensing', *Nat. Hazards* , no.35, pp. 361–376.

Schaul L., Fredembach C., Susstrunk S. 2009, ‘Colour image dehazing using the near-infrared’, *16th IEEE International Conference on Image Processing (ICIP), Cairo, 2009*, pp. 1629–1632.

Schechner Y., Karpel N. 2005, ‘Recovery of underwater visibility and structure by polarization analysis’, *IEEE Journal of Oceanic Engineering*, vol. 30, no. 3, pp. 570–587.

Schroeder W., Ellicott E., Ichoku C., Ellison L., Dickinson M.B., Ottmar R.D., Clements C., Hall D., Ambrosia V., Kremens R., 2014, 'Integrated active fire retrievals and biomass burning emissions using complementary near-coincident ground, airborne and spaceborne sensor data', *Remote Sens. Environ*., no. 140, pp. 719–730.

Smyth K.C., Shaddix C.R.,1996, 'The elusive history of m=1.57–0.56i for the refractive index of soot', *Combust Flame*, vol. 107, no.3, pp. 314–320.

Sonn S., Bilodeau G. A., Galinier P. 2013, ‘Fast and Accurate Registration of Visible and Infrared Videos’, *IEEE Conference on Computer Vision and Pattern Recognition Workshops, Portland-OR, 2013*, pp. 308–313.

Stankov K. 2009, ‘A Mirror with an Intensity-Dependent Reflection Coefficient’, *Applied Physics*, vol. 45, no. 3, pp. 191–195

Torero J.L., Simeoni A.,2010, *'Heat and mass transfer in fires: scaling laws, ignition of solid fuels and application to forest fires'*, Open Thermodyn Journal, no.4, pp. 145–155.

The Courier 2016, *Mt Bolton on Fire*, Adelaide, viewed 1 May 2017, <http://www.thecourier.com.au/story/3746465/update-properties-lost-as-bushfire-sweeps-across-mt-bolton>.

Thomas P.A., McAlpine R.S., 2010, *Fire in the Forest*, Cambridge University Press, NEW York, USA.

Thuillier G., Hers M., Simon P.C., Labs D., Mandel H., Gillotay D., Foujols T. 1998,’ The Visibility of Solar Spectral Irradiance from 350 to 850 nm As Measured By The Solspec Spectrometer During THE Atlas I Mission’, *Solar Physics*, vol. 177, pp. 41–61.

USGS 2017, *Solar Radiation in the Atmosphere*, LandSat USGS, viewed 1 June 2017, < https://landsat.usgs.gov/atmospheric-transmittance-information>.

Utkin A.B., Fernandes A., Simões F., Lavrov A., Vilar R., 2003, 'Feasibility of forest-fire smoke detection using lidar', 2003, *Int. J. Wildland Fire*, no.12, pp.159–166.

Vanmali A.V., Kellar S.G.,Garde V.M. 2015, ‘A novel approach for image dehazing combining visible-NIR images’, *2015 Fifth National Conference on Computer Vision, Pattern Recognition, Image Processing and Graphics (NCVPRIPG), Panta 2015*, pp. 1–4.

Vincent R. K., 1972, ‘An ERTS Multispectral Scanner experiment for mapping iron compounds’, *Proceedings of the Eighth International Symposium on Remote Sensing of Environment; October 2-6, 1972; Ann Arbor, MI*, pp. 1239–1247.

Voulgarakis A.,Field R.D.,2015, *'Fire Influences on Atmospheric Composition, Air Quality and Climate'*, Current Pollution Reports, Vol. 1, no. 2, pp. 70–81.

Voiland A. 2015, *Smoke Blankets Indonesia*, NASA, viewed 20 December 2016, < https://earthobservatory.nasa.gov/IOTD//view.php?id=86681>.

Wang W.T.,Qu J.J.,Hao X.J.,Liu Y.Q.,Sommers W.T, 2007, 'An improved algorithm for small and cool fire detection using modis data: A preliminary study in the southeastern United States', *Remote Sens. Environ.*, no.108, pp. 163–170.

Wang W., Gong W., Mao F., Pan Z., 2018,' Physical constraint method to determine optimal overlap factor of Raman lidar', *Journal of Optics*, vol.47, no.1, pp. 427–429.

Wang J., Asbach C., Fissan H., Hülser T., Kuhlbusch T.A.J., Thompson D., Pui D.Y.H., 2011, 'How can nano-biotechnology oversight advance science and industry: Examples from environmental, health, and safety studies of nanoparticles (nano-EHS)', J. *Nanoparticle Res*., no.13, pp.1373–1387.

Watts A.C., Ambrosia V.G., Hinkley E.A., 2012, 'Unmanned aircraft systems in remote sensing and scientific research: Classification and considerations of use' *Remote Sensing*, no. 4, pp. 1671–1692.

Werner D.,2015, 'Fire Drones.', *Aerosp. Am.*, no.53, pp.28–31.

Werf G.R.,Randerson J.T.,Giglio L.,Collatz G.J.,Kasibhatla P.S.,Arellano A.F.Jr., 2006, *'Interannual variability in global biomass burning emissions from 1997 to 2004'*, Atmos. Chem. Phys., no. 6, pp. 3423–3441.

William W. 2013, *Absorption of electromagnetic radiation*, AccessScience McGraw-Hill, viewed 21 April 2016, <http://accessscience.com/content/Absorption-of-electromagnetic-radiation/001600>.

Wilson W.E., Suh H.H. 1997, ‘Fine Particles and Coarse Particles: Concentration Relationships Relevant to Epidemiologic Studies’, *Journal of the Air & Waste Management Association.*, vol. 47, no.12, pp. 1238–1249.

Wu Z. J., Poulain L., Henning,S., Dieckmann K., Birmili W. Merkel M. van Pinxteren D., Spindler G., Müller K., Stratmann F., Herrmann H., Wiedensohler A., 2013, ‘Relating particle hygroscopicity and CCN activity to chemical composition during the HCCT-2010 field campaign’, *Atmos. Chem. Phys*., pp. 7983– 7996.

Xiang Li, Haohui Kong, Xinying Zhang, Bin Peng, Cong Nie, Guanglin Shen, Huimin Liu, 2014, 'Characterization of particle size distribution of mainstream cigarette smoke generated by smoking machine with an electrical low pressure impactor', *Journal of Environmental Sciences*, vol.26, no.4, pp. 827–833.

Xu Renliang , Scarlett Brian, 2002, Particle Characterization: Light Scattering Methods, *Springer*, Dordrecht, Netherlands.

Yang C., Westbrook J.K., Suh C.P., Martin D.E., Hoffmann W.C., Lan, Y., Fritz B.K., Goolsby J.A. 2014, 'An airborne multispectral imaging system based on two consumer-grade cameras for agricultural remote sensing', *Remote Sensing*, vol. *6*, no. 6, pp. 5257–5278.

Yuan C.,Zhang Y.M., Liu Z.X., 2015, 'A survey on technologies for automatic forest fire monitoring, detection and fighting using UAVs and remote sensing techniques', *Can. J. Forest*, vol. 45, no. 7, pp. 783–792.

Zajkowski T.J., Dickinson M.B., Hiers J.K., Holley W., Williams B.W., Paxton A., Martinez O., Walker G.W., 2016, 'Evaluation and use of remotely piloted aircraft systems for operations and research—RxCADRE', *Int. J. Wildland Fire*, no.25, pp.114–128.

Zahawi R.A., Dandois J.P., Holl K.D., Nadwodny D., Reid J.L., Ellis E.C., 2015, 'Using lightweight unmanned aerial vehicles to monitor tropical forest recovery', *Biological Conservation*, no. 186, pp. 287–295.

Zhai Yishu, Ji Dongjiang 2015, 'Single Image Visibility Improvement', *ISPRS; 30 August–2 September 2015, Toronto, Canada*, vol. XL-1/W4, viewed 5 June 2016, <http://www.int-arch-photogramm-remote-sens-spatial-inf-sci.net/XL-1-W4/355/2015/isprsarchives-XL-1-W4-355-2015.pdf >.

Zhang J., Yang C., Song H., Hoffmann W.C., Zhang D., Zhang G. 2016, 'Evaluation of an Airborne Remote Sensing Platform Consisting of Two Consumer-Grade Cameras for Crop Identification'. *Remote Sensing*, vol. *8*, no. 3, p. 257.

Zhao Jufeng, Zhou Qiang, Chen Yueting, Feng Huajun, Xu Zhihai, Li Qi 2013, ‘Fusion of visible and infrared images using saliency analysis and detail preserving based image decomposition’, *Infrared Physics & Technology*, vol. 56, pp. 93–99.

Zhao T.X.P., Ackerman S.,Guo W., 2010, 'Dust and smoke detection for multi-channel imagers', *Remote Sens.*, no. 2, pp. 2347–2368.

Appendices

10. Appendices

Appendix 1. Measurement of Optical Filter Spectral Response

This appendix contains all the spectroradiometric measurements conducted for verifying the custom-designed filter in lab environment using reference materials listed in Table 3.5.

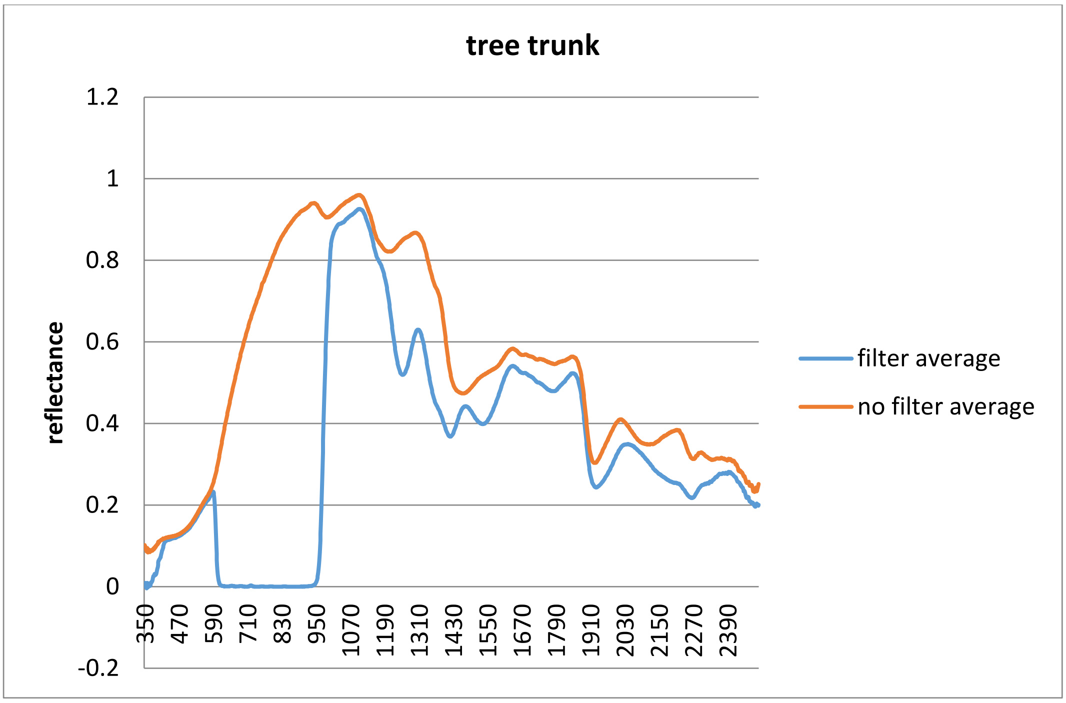

tree trunk
reflectance
1.2
1
0.8
0.6
0.4
0.2
0
-0.2
350
470
590
710
830
950
1070
1190
1310
1430
1550
1670
1790
1910
2030
2150
2270
2390
filter average
no filter average

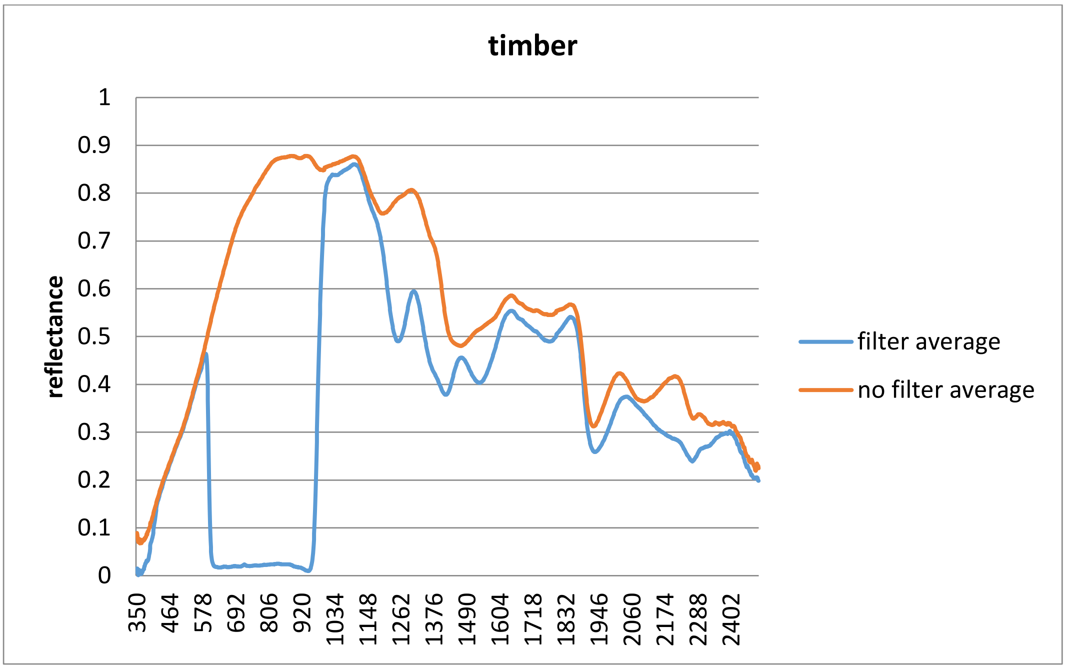
timber
reflectance
1
0.9
0.8
0.7
0.6
0.5
0.4
0.3
0.2
0.1
0
350
464
578
692
806
920
1034
1148
1262
1376
1490
1604
1718
1832
1946
2060
2174
2288
2402
filter average
no filter average

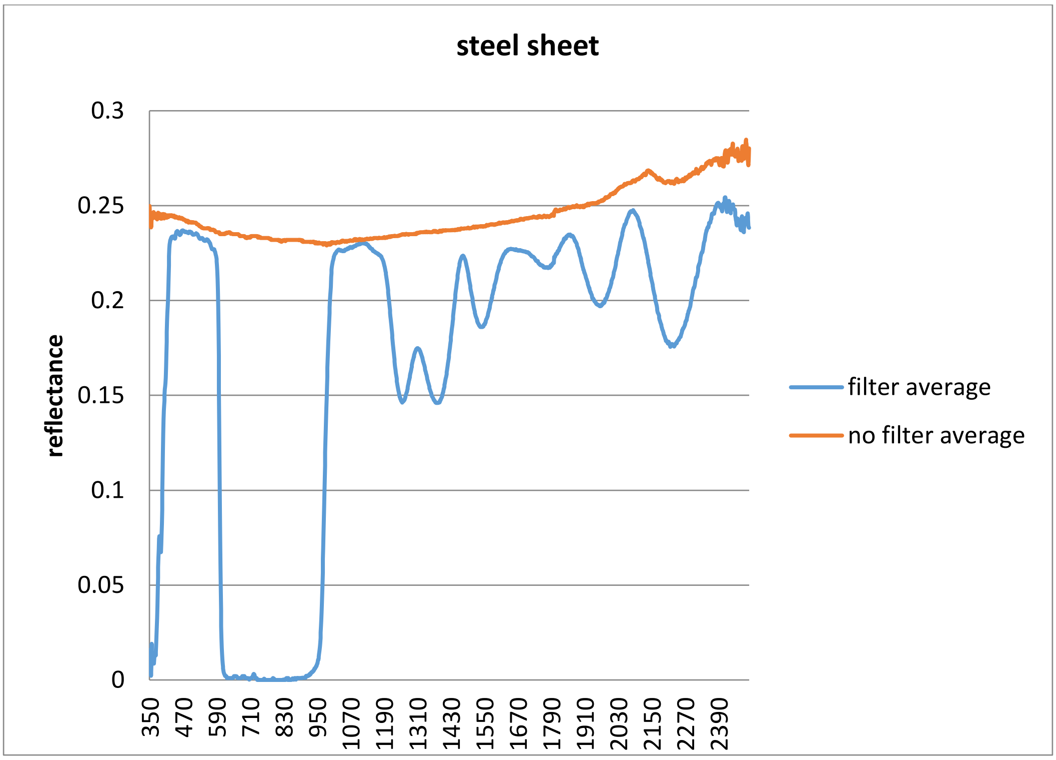
steel sheet
reflectance
0.3
0.25
0.2
0.15
0.1
0.05
0
350
470
590
710
830
950
1070
1190
1310
1430
1550
1670
1790
1910
2030
2150
2270
2390
filter average
no filter average

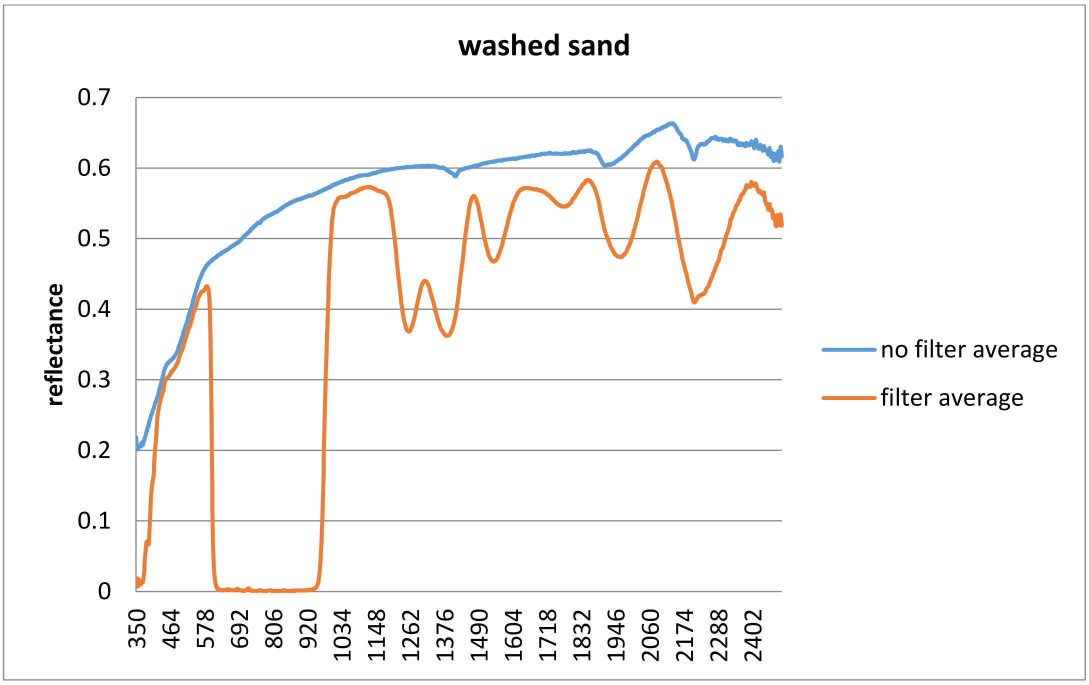
washed sand
reflectance
0.7
0.6
0.5
0.4
0.3
0.2
0.1
0
350
464
578
692
806
920
1034
1148
1262
1376
1490
1604
1718
1832
1946
2060
2174
2288
2402
no filter average
filter average

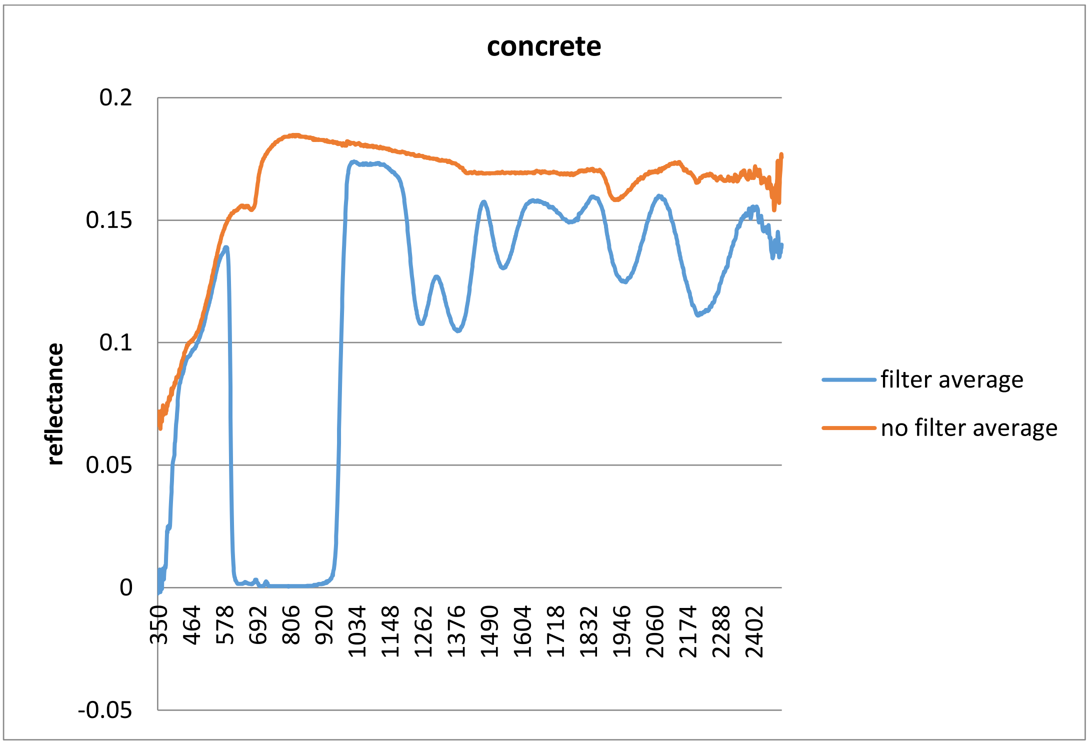
concrete
reflectance
0.2
0.15
0.1
0.05
0
-0.05
350
464
578
692
806
920
1034
1148
1262
1376
1490
1604
1718
1832
1946
2060
2174
2288
2402
filter average
no filter average

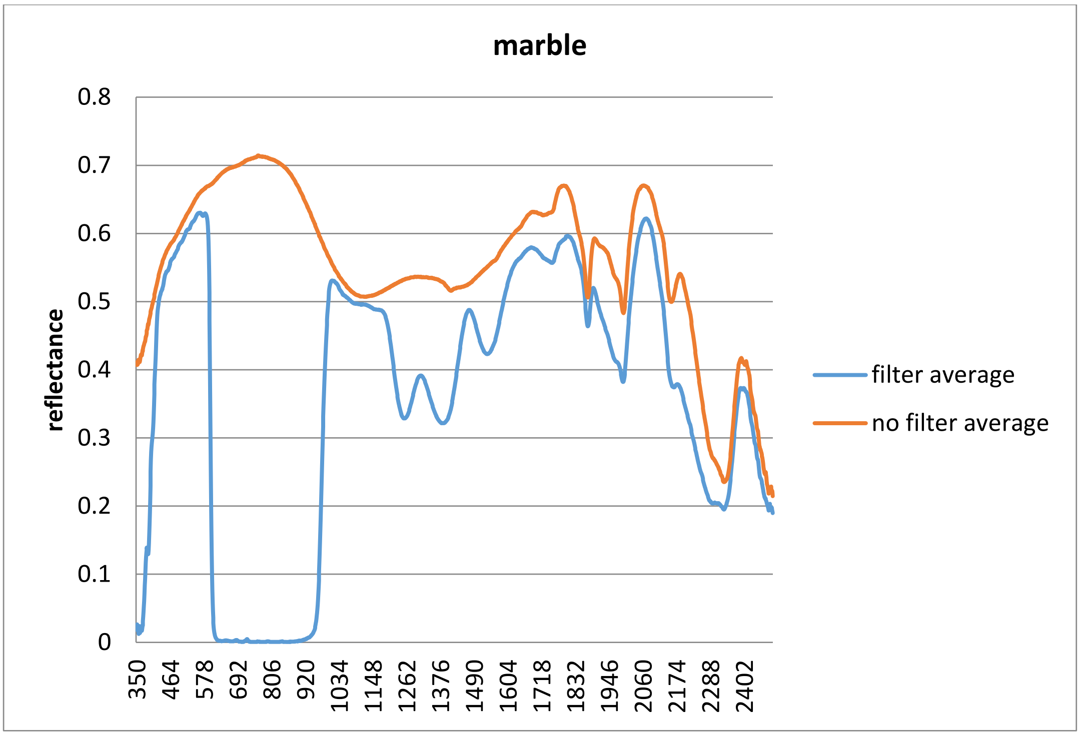
marble
reflectance
0.8
0.7
0.6
0.5
0.4
0.3
0.2
0.1
0
350
464
578
692
806
920
1034
1148
1262
1376
1490
1604
1718
1832
1946
2060
2174
2288
2402
filter average
no filter average

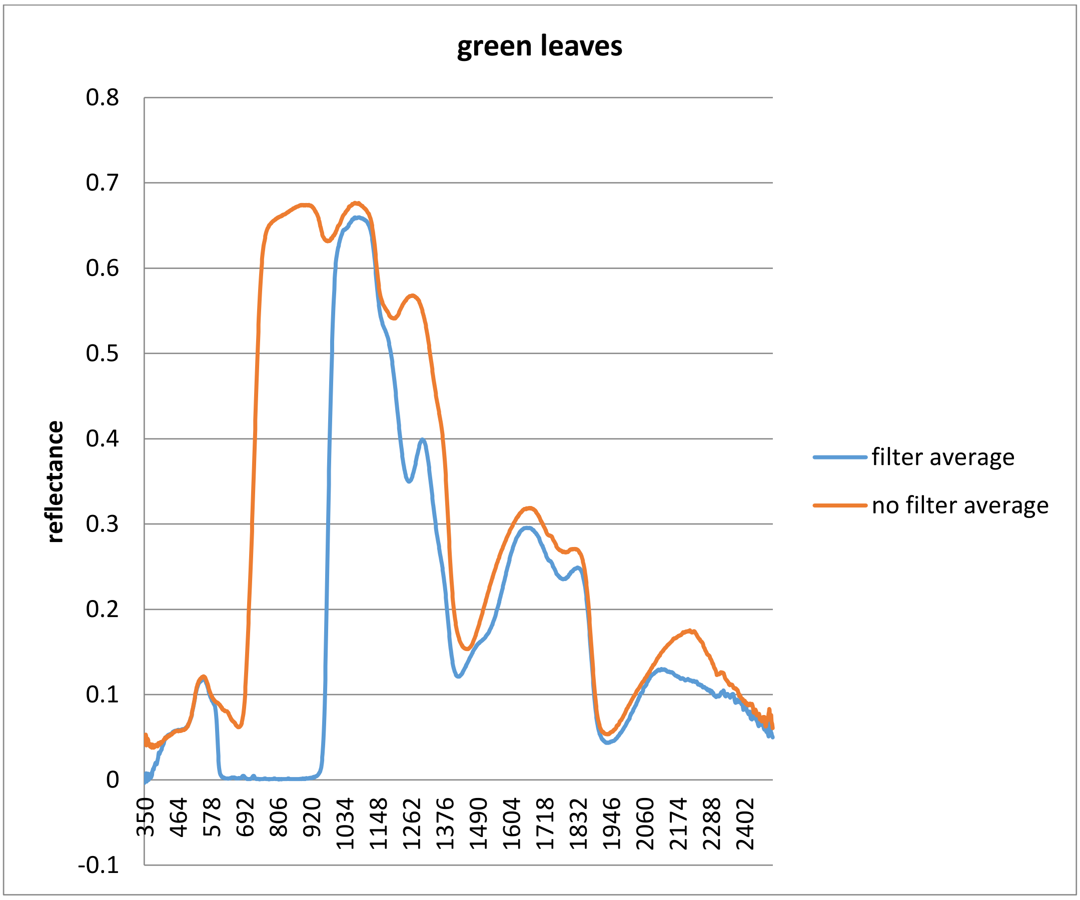
green leaves
reflectance
0.8
0.7
0.6
0.5
0.4
0.3
0.2
0.1
0
-0.1
350
464
578
692
806
920
1034
1148
1262
1376
1490
1604
1718
1832
1946
2060
2174
2288
2402
filter average
no filter average

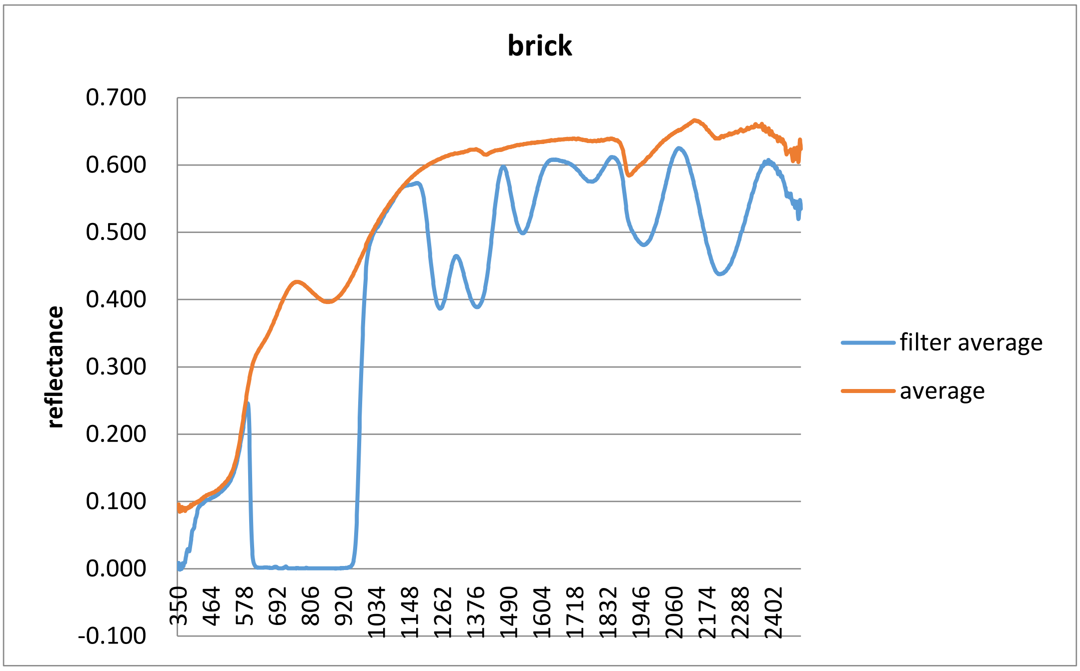
brick
reflectance
0.700
0.600
0.500
0.400
0.300
0.200
0.100
0.000
-0.100
350
464
578
692
806
920
1034
1148
1262
1376
1490
1604
1718
1832
1946
2060
2174
2288
2402
filter average
average

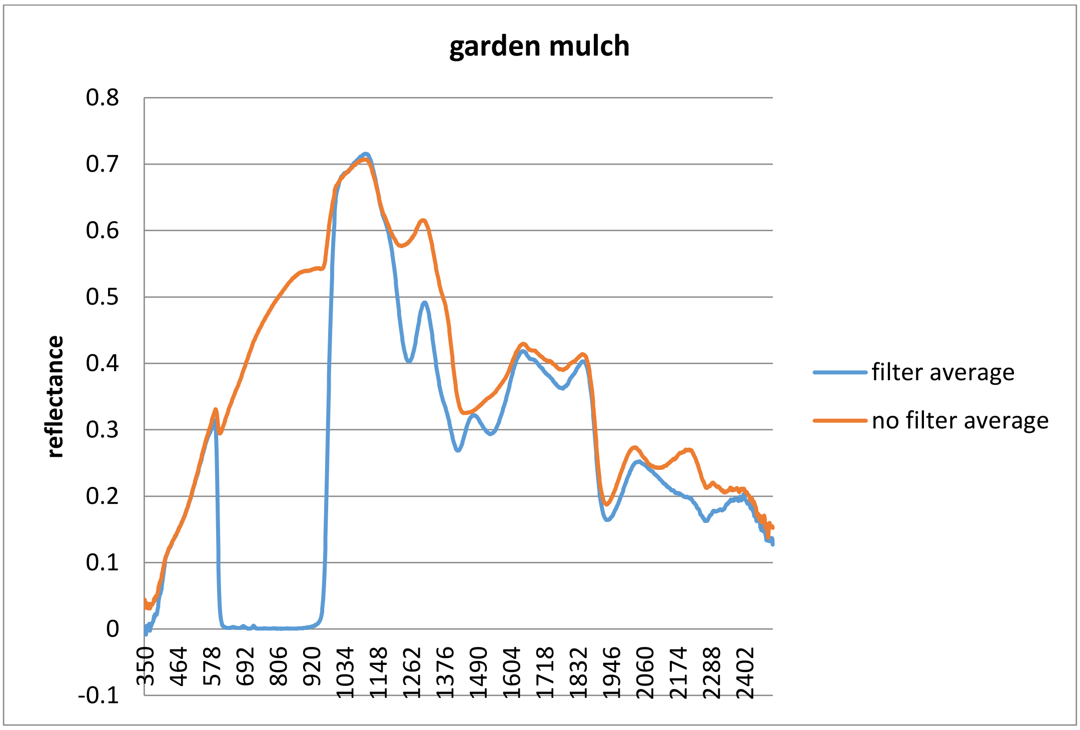
garden mulch
reflectance
0.8
0.7
0.6
0.5
0.4
0.3
0.2
0.1
0
-0.1
350
464
578
692
806
920
1034
1148
1262
1376
1490
1604
1718
1832
1946
2060
2174
2288
2402
filter average
no filter average

Appendix 2. Published Papers

This appendix contains two published papers:

Chabok M., 2013, ‘Eliminating and Modelling Non-metric Camera Sensor Distortions Caused by Sidewise and Forward Motion of the UAV’, *ISPRS - International Archives of the Photogrammetry, Remote Sensing and Spatial Information Sciences*, vol. XL-1/W2, pp.73-79

Chabok M., Millington A., Hacker J.M, McGrath A.J 2016, ‘*Visibility through the gaseous smoke in airborne remote sensing using a DSLR camera’*, Proc. SPIE, Fourth International Conference on Remote Sensing and Geoinformation of the Environment (RSCy2016), vol. 9688.

Eliminating and Modelling Non-metric Camera Sensor Distortions Caused by Sidewise and Forward Motion of the UAV

Mirahmad Chabok
chabok@dronemetrex.com

Dronemetrex Ltd. South Australia, Adelaide
Flinders University, School of the Environment, South Australia, Adelaide

KEY WORDS: UAV Photogrammetry, Motion Compensation, Distortion and Blur, Quick Processing

ABSTRACT:

This paper explains the critical importance of modelling and eliminating the effect of motion of an Unmanned Aerial Vehicle (UAV) as a result of air turbulence and unstable flight conditions on a camera sensor and the image geometry. A new method for improving the geometrical distortions caused by this motion is introduced. We have developed a hardware and software tool to minimize and model the geometric distortion of the image from commercial off-the-shelf (COTS) cameras which are commonly being used in aerial mapping UAVs. Due to the rolling shutter mechanism of the most common SLR cameras, sideway and forward motions of the UAV during image capture will have a strong effect on the image geometry and final product accuracies. As the amount of this random distortion varies from one photo to the next, a unique and robust camera calibration model cannot be established for interior orientation and image processing using photogrammetric methods, even by self-calibration. To achieve the highest possible accuracy, we also consider temperature effects on the camera calibration parameters. In this paper we show the results, accuracies and benefits of using this method compared with a typical UAV mapping system. To the best of our knowledge this is the first time that this method has been implemented in a UAV mapping system.

1. INTRODUCTION

Random geometric distortions on each individual photo will produce non-reliable, non-repeatable and inaccurate results irrespective of the kind and make of the software used for photogrammetric computations. The main reason for such distortions are sideways and forward motion of the camera coupled with the method of electronic recording and read out time of the CMOS imaging chip during exposure, in which every pixel is written at a slightly different time (see Figure 1 b). Our method is based on three steps. Firstly, we keep the camera aligned with pre-designed flight lines, i.e. drift free, during the exposure time by implementing a low weight robotic stabilized Camera Mount (CM) which compensates for Pitch, Roll and Yaw angles in a high vibration environment. (see Figure 1c). The CM receives the rotational corrections from the IMU with one degree resolution as well as the drift angle from a digital compass with two degree resolution and keeps the camera sensor aligned with the flight direction and nadir position which means that, the camera axis at triggering points will always be parallel (see Figure 2a) to the flight path. By doing so, the rolling shutter effect and pixel distortions will be aligned with the flight direction (see Figure 1c). Secondly, we estimate the Point Spread Function (PSF) which now has only one linear direction and is thus less complicated to estimate. Estimating the PSF with sub-pixel accuracy is very crucial to avoid un-desired effects. For sub-pixel PSF estimation we use the camera shutter speed and ground speed of the UAV at the time of exposure for each image. Thirdly, we then use the PSF for image deconvolution and for compensation for forward motion. For this purpose a software tool has been developed for automatic PSF calculation from GPS log files and applying the corrections for every single image. Furthermore, because the camera has a non-rigid body, the location of the principal point of the camera, and thus the focal length will vary with temperature. To achieve a stable interior orientation parameters, we perform the laboratory camera calibration for different temperatures and use the temperature based calibration parameters making use of the recorded actual internal temperature of the UAV. This procedure produces a distortion-free image with robust interior orientation ready to use for photogrammetric computations. At the same time, this method reduces the processing time substantially guaranteeing reliable and repeatable accuracies.

1.1 Related Work

Image motion compensation and the resulting image blur has been addressed in computer vision and image processing industries. Examples are feature tracking based on extracting the 3D motion of the camera [Liu et al.2009], using an Inertial measurement unit (IMU) for image motion de-blurring [Joshi et al.2010, Gruber et.al. 2012] and a mechanical image stabilization system in walking robots [Kurazume and Hirose 2000]. IMU based image de-blurring which has recently been introduced is IMU sensor dependent and suffers in restoring the geometric pixel distortions in a high turbulence flight environment. As Electro Magnetic Interference (EMI) and Radio Frequency Interferences (RFI) in UAVs can upset the IMU output rates and its accuracy, relying on IMU data for estimating the PSF will be unreliable in UAV photogrammetry except when using expensive high end IMUs. In our proposed method we first apply a low pass filter to the IMU data and then use this noise-free IMU data as an input to the CM for angular motion compensation. This method will keep the camera in nadir position, whereas the flight management software applies the drift corrections from the digital compass (See Figure 2a). The effect of temperature changes on the camera calibration parameters is shown in Figure 6 [6].

2. OUR WORKFLOW

Our image acquisition system compensates for side and rotational motion of the UAV during image capture and corrects for the UAV's crab angle. Therefore there will be no image warp and distortion from rotational movements of the camera and the only remaining issue will be the forward motion compensation and restoring the original un-blurred image.

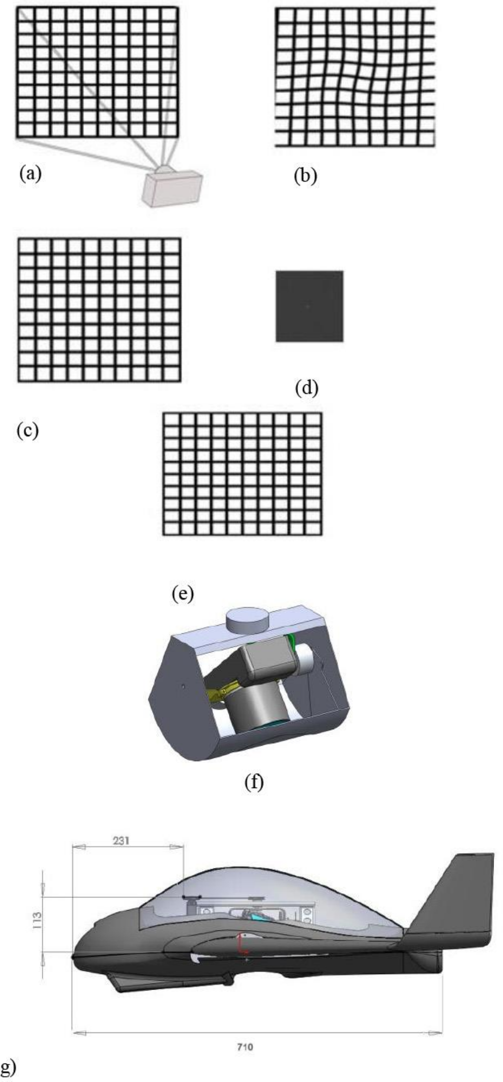

Figure 1: (a) camera sensor exposing the image with rolling shutter, (b) captured photo with side and forward motion of the UAV, image is warped and skewed, (c) captured photo with compensated side and rotational movements of the camera using our proposed method, pixels are stretched only in flight direction, (d) calculated PSF map based on ground and shutter speed, (e) Deconvolved image using generated PSF , image is un-blurred and distortion free, (f) CM with 400 grams net weight including the lens protection door for take-off and landing, (g) CM installed in TopoDrone-100 mapping UAV.

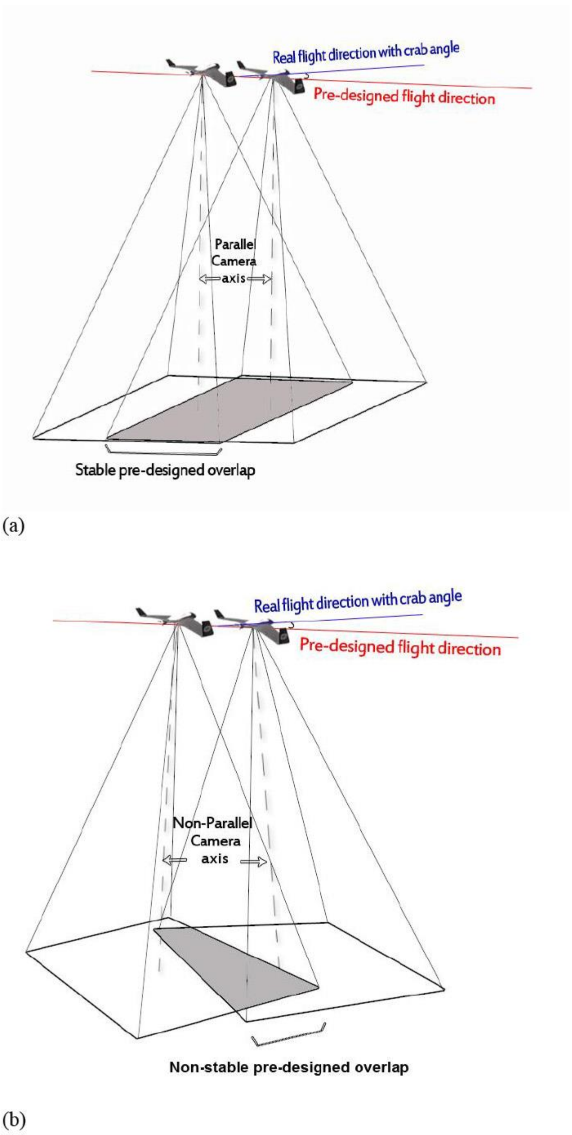

Figure 2: (a) shows our method for image acquisition using CM and parallel camera axis in all flight conditions with compensation for crab angle. Photos are taken in pre-designed flight direction with stable overlap, models are parallax free and tie points matching will be accelerated in aerial triangulation. Stereo models can be imported in stereo plotters for 3D feature extractions (b) shows the effect of non-parallel camera axis, captured images are not aligned with pre-designed flight direction and requires large overlaps to full-fill the minimum stereo overlap requirement, tie points matching requires more processing time.

2.1 Motion Blur Calculation

We estimate the linear blur amount for each photo using shutter and ground speed which is extracted from the GPS log file . The motion blur is calculated as follow [5]:

$$L_i = v_i \times t_i \times \frac{f}{c \times h_i} \times 10\text{^}3 \qquad (1)$$

where for every image *(i)*

L_i = motion size in pixel

v_i = linear ground speed for image (*i*) in km/h at the time of exposure

t_i = exposing time

f = focal length in mm

h_i = flying height above ground in meter

c = camera sensor pixel size in micron

In regards to the angular motion, we have logged the actual angular velocity for both UAV and CM during the flight in a stable direct flight path and normal weather condition.

Figure 3a. shows the pitch angle rotation rate of the UAV, the average rotation rate of the UAV is 0.3 rad/s whereas the average rotational speed of the CM is 0.03 rad/s according the Figure 3b. It can be seen in Figures 3c and 3d that the roll rate is almost identical to the pitch rate. The angular velocity of the CM is significantly smaller than that of the UAV which results in less blur from angular motion.

For example, the amount of blur caused from sideways and forward motion of a typical fixed-wing UAV can be calculated as follow with assuming :

Cruise speed: 80 km/h
Camera shutter speed: 1/1000 s
Camera's sensor size: 4 micron
Focal length: 28 mm
Flying height: 120 m

Using the Equation (1) the forward motion blur will be 4.7 pixels. (see Figure 4a)

To obtain the side motion blur, using Equation (2) and (3) derived from Figure 4 to convert the angular velocity to linear ground speed, the equivalent linear speed of the UAV in both pitch and roll direction will be 0.3 rad/sec × 120m=36 m/s or 129.6 km/h. Using Equation (1), the side motion blur amount will be 7.5 pixels. In our proposed method the linear speed for the CM using Equation (3) is 0.03 rad/s × 120m = 3.6 m/s or 12.96 km/h. The blur amount caused is only 0.7 pixels, we only apply the PSF in forward motion direction.

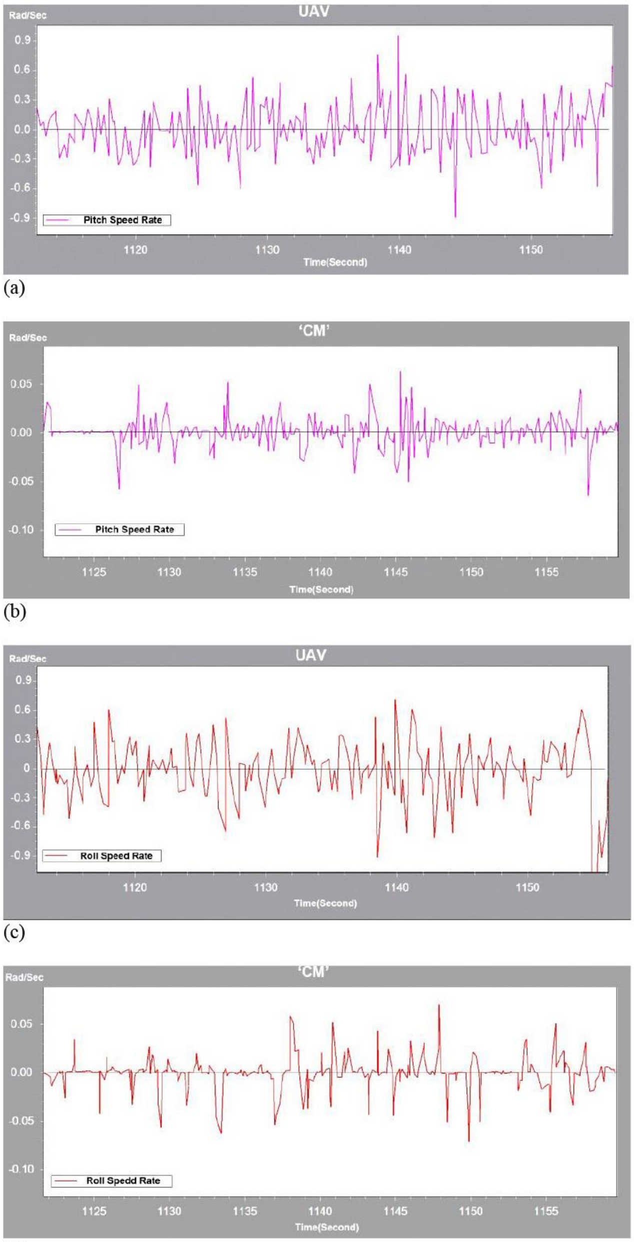

(a)

(b)

(c)

(d)

Figure 3. shows the angular velocity in rad/s at the same time period for : (a) the pitch rate of the UAV, (b) pitch rate of the CM , (c) roll rate of the UAV, (d) roll rate of the CM.

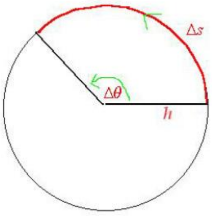

Figure 4. Converting angular speed to linear speed

$$\omega = \frac{\Delta\theta}{\Delta t} \tag{2}$$

where ω is the angular speed and Δt is time for $\Delta\theta$ rotation.

$$v = \frac{\Delta s}{\Delta t} = \frac{h \times \Delta\theta}{\Delta t} = h \times \omega \tag{3}$$

where v is the linear speed and h is the flying height above ground.

Depending on turbulence encountered, the angular velocity of the UAV can reach up to 200 °/s (3.5 rad/s), this means it takes 1.8 s for one revolution which is normal for a typical low weight fixed-wing UAV.

2.2 PSF Calculation

The captured image using our method will only have a forward motion blur in a known direction, Figure 1c, which is convoluted with the PSF as shown in Equation (4).

$$g(x,y) = f(x,y) * h(x,y) \tag{4}$$

where *g(x,y)* is the latent image, *f(x,y)* the blurred image and *h(x,y)* the PSF for every *x* and *y* pixel position. Noise is assumed to be zero in this equation. The blur amount and direction is known and is only in one direction, hence we use the general form of the linear uniform PSF function following [2]:

$$h(x,y) = \frac{1}{L}\prod_L (x\cos\alpha + y\sin\alpha) \tag{5}$$

$$\prod_L (u) = \begin{cases} 1 & \text{if} \quad -\frac{L}{2} \le u \le \frac{L}{2} \\ 0 & \text{if} \quad |u| > \frac{L}{2} \end{cases}$$

where α is the motion direction and L the blur length.

We calculate the Fourier Spectrum of *f(x,y)* in the frequency domain and remove the image motion blur with estimated noise variant using the 'Richardson-Lucy' iterative de-convolution algorithm [3], which is an iterative procedure for recovering a latent image that has been blurred by a known PSF function[4]. Pixels in the blurred image can be represented in terms of the original image and PSF function as :

$$d_i = \sum_j h_{ij} u_j \tag{6}$$

where h_{ij} is the PSF function, u_j is the pixel value at location *j* in the latent image, d_i is the observed value at position *i*. The statistics are performed under the assumption that u_j is Poisson-distributed which is appropriate for photon noise in the data. We use the following iterative equation from [3] to calculate the most likely u_j given the observed d_i :

$$u_j^{(t+1)} = u_j^{(t)} \sum_i \frac{d_i}{c_i} h_{ij} \tag{7}$$

where

$$c_i = \sum_j h_{ij} u_j^{(t)}$$

After recovering the blured image we apply temprature based camera calibration parameters to correct for principal point displacement, focal length and lens distortion. The radiometric corrections can be applied as a last step for high accuracy photogrametric computations.

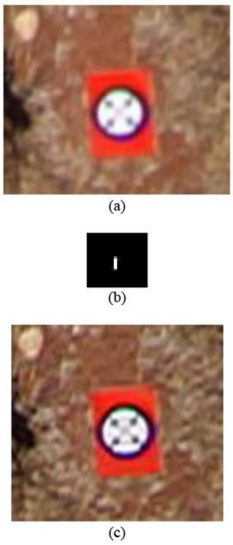
(a)
(b)
(c)

Figure 4: (a) part of an aerial image over signalized target (b) calculated PSF for 4.7 pixels, (c) corrected image

3. REAL WORLD EXAMPLES

To determine error caused by sideways and forward motion of the UAV and thus unstable interior orientation, we have performed a test flight over a test field area with 1.5cm GSD resolution and have processed the results twice, (1) with applying PSF and post processing and (2) without post-processing. The temperature differences at the flight time and camera calibration environment will cause inaccuracies [6]. In our case study the flight time temperature was 9 degree, with assuming 22 degree for a normal lab temperature the error caused from temperature effect would have been 0.015mm for focal length and principal point location (see Figure 6). To obtain a robust result we calibrated the camera in the laboratory using established calibration targets and at the same temperature as at the flight time which was 9 degree in our case study.

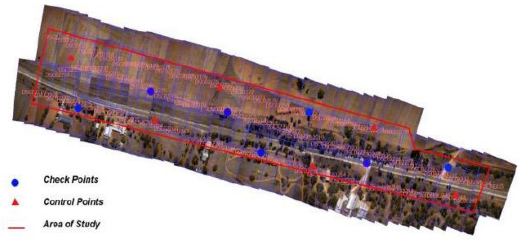

Figure 5. Test flight area with 1.6km length and 250m width. Non-signalized GCPs are acquired by RTK GPS equipment with 2cm horizontal and 4cm vertical accuracy.

	RMS_x(m)	RMS_y(m)	RMS_z(m)
Before post-processing, with 4.5 pixel motion blur	0.052	0.055	0.17
After post-processing without motion blur	0.034	0.039	0.048

Table 1. AT residuals of the check points

Table.1 shows that the RMS of the horizontal points after motion compensation, when considering a 2 pixel error for measuring non-signalized control points, is improved and in an acceptable range. This improvement is more obvious in vertical points and shows that the linear blur compensation in absence of the angular motion blur, has a greater effect on the vertical accuracy. It is expected to achieve better absolute accuracies within 1 pixel for horizontal and 2 pixels for height by using signalized control points.

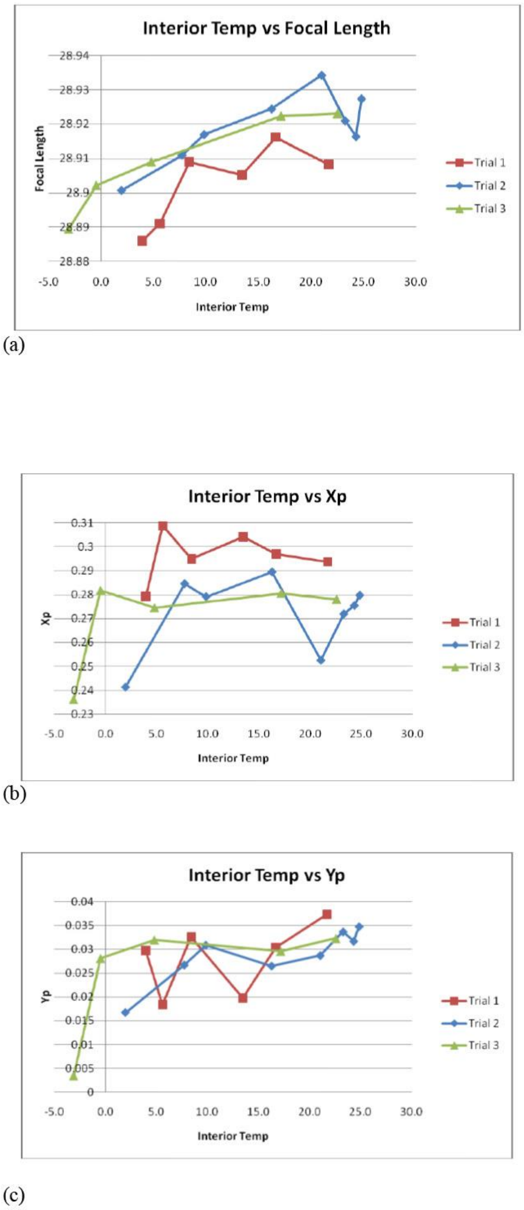

(a)

(b)

(c)

Figure 6. (a): shows the effect of temperature changes on the focal length which is approximately 0.01 mm per every 10 degrees temperature changes, i.e. 0.03mm for 30 degrees. (b) and (c) shows the effect of temperature changes on the principal point position(Xp,Yp). This is important when the camera is calibrated in the lab environment but is operated in a different temperature environment.

(a) (b) (c) (d) (e) (f) (g) (h)

Figure 7. (a), (b) ,(e) and (f) images before post-processing, (c) (d), (g) and (h) after post-processing. More details are visible after post-processing.

4. CONCLUSION

We have shown that for photogrammetry at highest accuracy, it is very important to model and eliminate the sideways and forward motion of the UAV. This will improve the height accuracy up to five times and will have a considerable impact on the horizontal accuracies and stability of the models. Camera motion during image capture with CMOS sensors will cause random geometric distortions and image warping, as well as image blur. The distortions and warping depend on the focal plane direction of the shutter and flight direction by corrupting the interior orientation parameters which are a fundamental issue for any photogrammetric approach. We also showed that by applying the correct PSF to each image, more details will be retrieved (see Figure 7b and d). This method can be applied for any metric and non-metric cameras with CCD or CMOS sensors to eliminate the amount of blur and pixel distortions caused from unexpected movements of the fixed wing, rotary UAVs or other imaging platforms and will eliminate the possible need for a repeat flight. Post-processing of the UAV images for eliminating the motion blur distortions and applying the temperature based camera calibration parameters and radiometric corrections, will produce perfect images for the highest grade photogrammetric processing. For future developments we are considering a custom designed miniature image processing chip for on-board processing and real-time blur corrections.

REFERENCES

[1] M. Cannon, Blind deconvolution of spatially invariant image blur with phase, IEEE Trans. Acoust. Speech Signal Process. 24 (1) (1976) 58–63.

[2] Jong Min Lee, Jeong Ho Lee, Ki Tae Park, Young Shik Moon, Image deblurring based on the estimation of PSF parameters and the post-processing. Optic 2012.

[3] W.H. Richardson, Bayesian-based iterative method of image restoration, J. Opt.Soc. Am. 62 (1) (1972) 55–60

[4] http://en.wikipedia.org/wiki/Richardson-Lucy_deconvolution

[5] Photogrammetry: geometry from images and laser scans, 2nd edition
By Karl Kraus University of Vienna Austria. pp. 155-157

[6] M. J. Smith , E. Cope, 2010. The effects of temperature variations on single-lens-reflex digital camera calibration parameters. International Archives of Photogrammetry, Remote Sensing and Spatial Information Sciences, Vol. XXXVIII, Part 5 Commission V Symposium, Newcastle upon Tyne, UK.

ACKNOWLEDGEMENTS

The author thanks A/Prof. Jorg M.Hacker for reviewing this paper.

Visibility through the gaseous smoke in airborne remote sensing using a DSLR camera

Mirahmad Chabok*[a], Andrew Millington[a], Jorg M. Hacker[a,b], Andrew J. McGrath[a,b]
[a] Flinders University, School of the Environment, South Australia
[b] Airborne Research Australia, South Australia
*mirahmad.chabok @flinders.edu.au

ABSTRACT

Visibility and clarity of remotely sensed images acquired by consumer grade DSLR cameras, mounted on an unmanned aerial vehicle or a manned aircraft, are critical factors in obtaining accurate and detailed information from any area of interest. The presence of substantial haze, fog or gaseous smoke particles; caused, for example, by an active bushfire at the time of data capture, will dramatically reduce image visibility and quality. Although most modern hyperspectral imaging sensors are capable of capturing a large number of narrow range bands of the shortwave and thermal infrared spectral range, which have the potential to penetrate smoke and haze, the resulting images do not contain sufficient spatial detail to enable locating important objects or assist search and rescue or similar applications which require high resolution information. We introduce a new method for penetrating gaseous smoke without compromising spatial resolution using a single modified DSLR camera in conjunction with image processing techniques which effectively improves the visibility of objects in the captured images. This is achieved by modifying a DSLR camera and adding a custom optical filter to enable it to capture wavelengths from 480-1200nm (R, G and Near Infrared) instead of the standard RGB bands (400-700nm). With this modified camera mounted on an aircraft, images were acquired over an area polluted by gaseous smoke from an active bushfire. Processed data using our proposed method shows significant visibility improvements compared with other existing solutions.

Keywords: smoke penetration, light scattering, visibility enhancement, bushfire mapping

1. INTRODUCTION

Smoke, fog, haze and particles in the atmosphere cause scattering of light and, consequently, compromise the quality of aerial images captured by a DSLR camera. Rayleigh's scattering law states that amount of radiation scattered by particles in the atmosphere increases with increasing wavelength [1], which means that scattering effect is more visible in the blue end of the visible spectrum. In contrast, Near Infrared (NIR) light is less scattered than visible light, consequently, NIR images will be less affected by smoke, haze and fog than standard RGB images. DSLR camera sensors are made of silicon which is inherently sensitive to NIR radiation, see Figure 3, but most DSLR cameras use a NIR cut-off filter in front of the sensor to prevent radiation between 700-1200nm contaminating the visible image. Radiation in the NIR

Fourth International Conference on Remote Sensing and Geoinformation of the Environment (RSCy2016),
edited by Kyriacos Themistocleous, Diofantos G. Hadjimitsis, Silas Michaelides, Giorgos Papadavid,
Proc. of SPIE Vol. 9688, 96880Q · © 2016 SPIE · CCC code: 0277-786X/16/$18 · doi: 10.1117/12.2241511

spectrum can however be easily acquired by modifying the camera and removing the cut-off filter [2]. The combination of NIR with RGB images has been widely used in recent studies [3]-[5] for image enhancement and haze removal. This approach requires exact co-registration of NIR and RGB images which is a non-trivial step in the processing workflow.

In airborne remote sensing and imaging, successful image registration and data fusion using multi sensors is subject to many factors such as exposure synchronization of the sensors, geometric distortion of the captured images caused by aircraft sideways and forward motions [6,7] and the movement of the smoke particles which can cause dynamic background movements and distortion in the captured images. Most advanced haze removal algorithms [8] involve two steps, modeling the haze and attempting to recover lost details. These algorithms are usually based on estimating a haze model and transmission map using a single image or a combination of multi sensor images. Multi image haze removal algorithms exploit the difference between two or more images of the same scene that have different properties [9], but these approaches are not applicable to dynamic scenes in airborne applications where ground objects and smoke particles can move quickly relative to each other.

In this research, we propose a simple and novel solution for aerial image clarity enhancement and smoke/haze effect reduction on captured image without using complex computational haze removal algorithms which allows its implementation in near real-time applications such as search and rescue operations, target detection and firefighting.

2. BACKGROUND

2.1 Electromagnetic Light Scattering

Electromagnetic radiation (EMR) reflected by objects on the ground and in the atmosphere and detected by downward-looking space or airborne sensors, is exposed to scattering processes twice, once on its journey from the sun to the earth's surface and then after being reflected by materials at the surface of the earth back to the atmosphere (and sensor). Air molecules, haze or smoke particles in the path of EMR change the direction of the light. This is known as scattering effect which, in turn, reduces the image contrast and changes the spectral signature of ground objects as seen by the sensor, see Figure 1. The amount of scattering depends on the size of the particle and the wavelength of the radiation. According to molecular scattering (Rayleigh) theory, for particle size smaller than wavelength ($< \lambda/10$) scattering is inversely proportional to the fourth power of the wavelength. Therefore, short wavelengths visible light will be scattered more than longer wavelength visible or NIR radiation, see Figure 2. With increasing particle size, the physical interactions between light and particles change from Rayleigh-type to Mie-type scattering. When the particles are large ($> \lambda/10$), spherical, and diverse, the dependency between scattering intensity and wavelength disappears and all wavelengths are equally scattered. Gaseous smoke particles follow the Rayleigh scattering law.

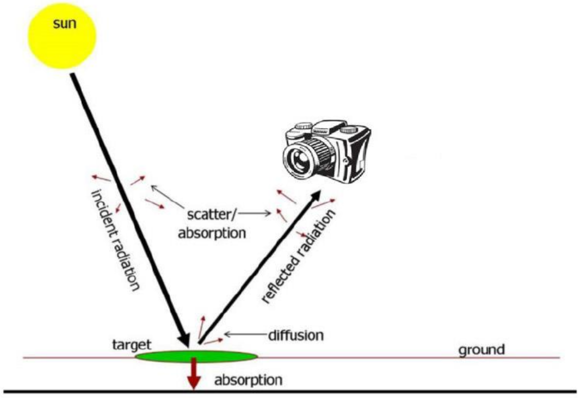

Figure 1. Schematic view of EMR travelling from its source to a ground target and the scattering, absorption and diffusion effects while being captured by imaging sensor. Light scattering commonly compromises spatial resolution, and smoke particles lead to lack of visibility in imagery.

(Modified from http://fcaglp.fcaglp.unlp.edu.ar/referenciacion/index.php/Sensores_Remotos)

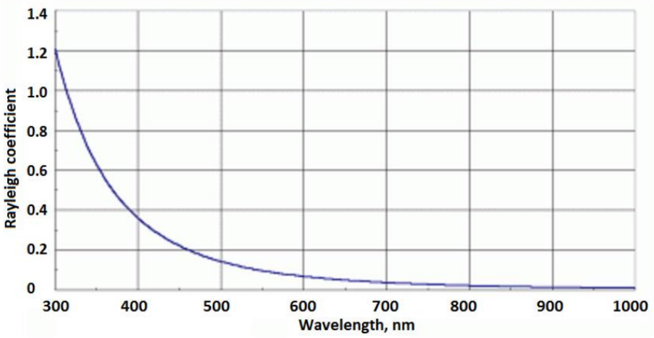

Figure 2. Rayleigh-type scattering, note that longer wavelength (NIR radiation) is scattered less than that at short wavelengths. For example, radiation at 400nm (visible blue) is scattered 40 times more than NIR at 1000nm.

(Image source: http://www.pages.drexel.edu/~brooksdr/DRB_web_page/papers/UsingTheSun/using.htm)

2.2 Optical Spectral Filters

Optical filters are devices that selectively transmit light at different wavelengths. The optical properties of filters are completely described by their frequency response, which specifies how the magnitude and phase of each frequency component of an incoming signal is modified by the filter. Optical filters transmit selected light in a particular range of wavelengths (or colours), while blocking all other wavelengths [10]. We use a custom designed bandpass filter in front of the modified camera to block wavelengths under 470nm and transmit from 470 to 1200nm, which enables the modified camera to capture R, G and NIR bands in one image, see Figure 4. As discussed above, NIR radiation is less scattered by smoke particles in the air and, thus has stronger penetration capability, than visible light in the atmosphere. We take advantage of this to enhance the visible RG bands with the NIR channel and attempt to improve the visual quality of the captured image by implementing a custom image processing algorithm.

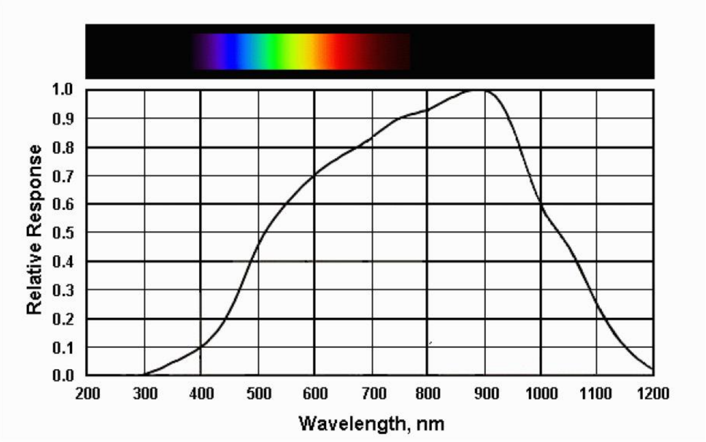

Figure 3. Response curve of a silicon based camera sensor at visible and NIR wavelength. Silicon photo diodes are sensitive to EMR from approximately 200-1200nm.

(Modified from https://en.wikipedia.org/wiki/Photodiode)

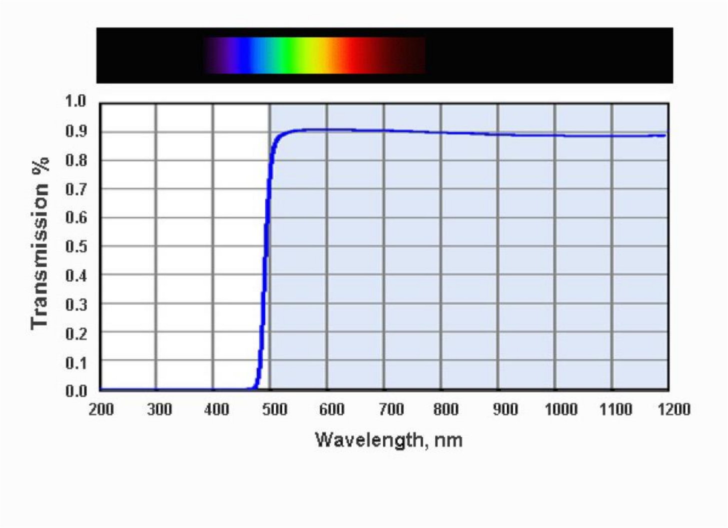

Figure 4. Spectral transmission curve of the custom-designed filter used in this study which transmits the light in the blue shaded area and blocks the wavelengths in the white area.

3. IMAGE OPTIMIZING AND ENHANCING

This process first attempts to optimize the corresponding pixels for the G and R channels using the NIR band, considering the fact that NIR bands contains more information from the scene, to produce an intensity image. This is implemented using Equations (1) and (2) to blend the NIR with the G and R bands by multiplying each pixel in the NIR channel by its corresponding pixel in the G and R bands, with each pixel containing a single colour.

$$f(NIR, G) = NIR * G \tag{1}$$

$$f(NIR, R) = NIR * R \tag{2}$$

$$R_1 = f(NIR, B),\ G_1 = f(NIR, G)$$

$$I = \ (R_1, G_{1,} NIR)$$

f(NIR,G) and f(NIR,R) are the channel blending functions between the NIR and G bands and NIR and R channels, respectively. A composite image (I) is then formed by combining the enhanced R, G and initial NIR channels. A minimum-maximum linear contrast stretch is used to optimize the new image in which the original minimum and maximum values of the data are assigned to a newly specified set of values that utilize the full range of available brightness values.

$$g(x, y) = \frac{I(x,y) - \min}{max - min} * 255 \tag{3}$$

In Equation (3), g(x,y) represents the output image and, I(x,y) the input image, while "min" and "max" are the minimum and maximum intensity values of each channel in the current image.

The modified camera system fitted with the optical filter was mounted on an aircraft and flown over an active bushfire that was producing smoke and the captured data was then processed as shown in Figure 5 and 6.

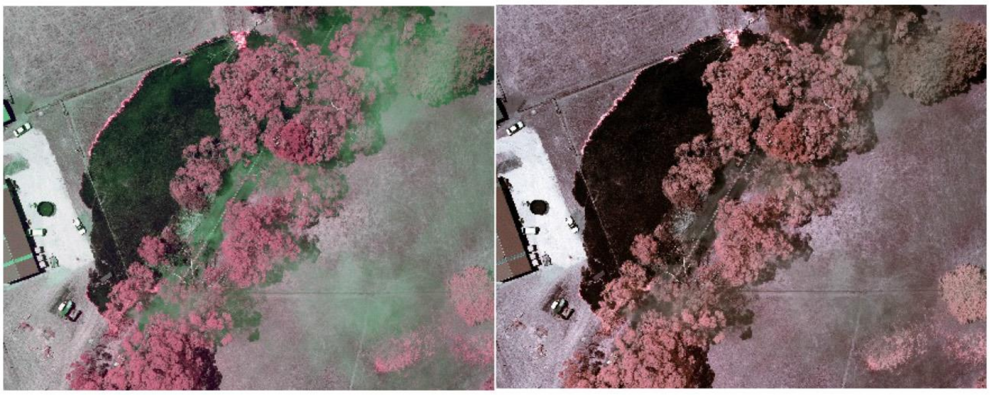

Figure 5. Left: original image captured by the modified camera. Right: modified image showing the result of applying Equations (1) to (3) based on our proposed method. The effect of Rayleigh scattering caused by smoke particles is greatly reduced in right hand resulting image and more scene details are visible without introducing noise or loss of details.

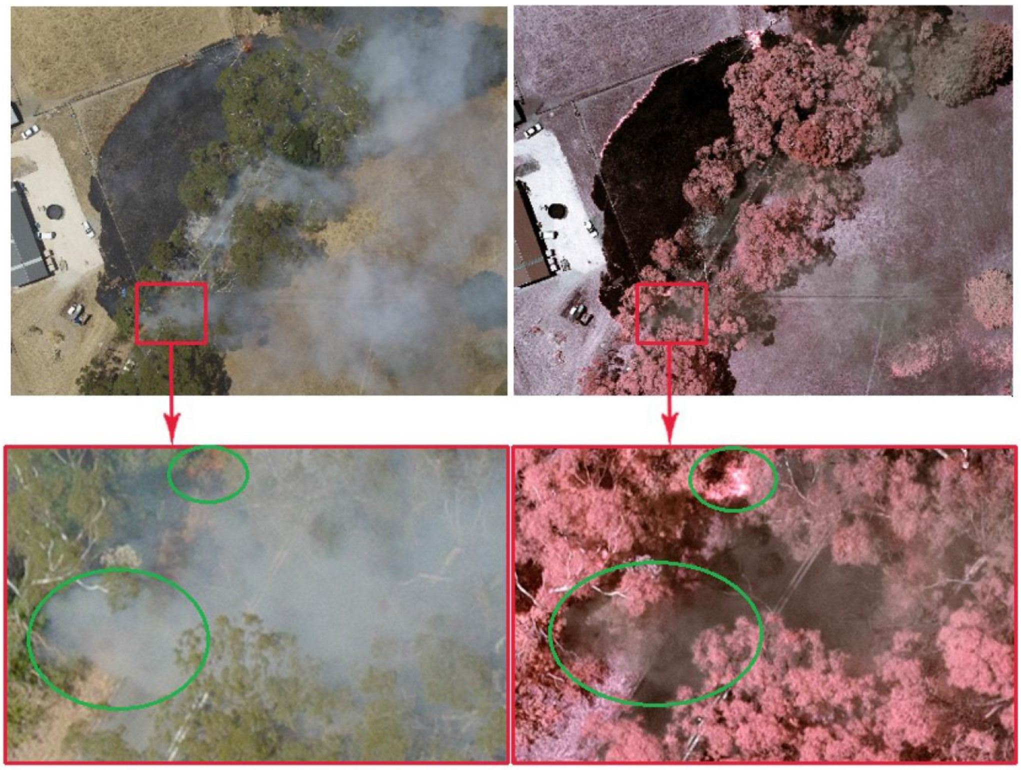

Figure 6. Top left: image captured by a non-modified RGB camera for comparison purposes. Top right: image captured by the modified camera and processed as described above. Bottom left and right: zoomed-in section of the corresponding images above showing that smoke has largely blocked visibility of the ground objects (left image), whereas objects on the ground are visible using the proposed smoke/haze reduction method (right image). The green circles emphasise identical areas in the images in the bottom row.

4. CONCLUSION

In this paper we have introduced a novel method for airborne image visibility enhancement in bushfires or similar situations in which smoke or haze particles restrict the visibility of important ground objects in captured images. This method employs a modified camera which is able to capture composite colour images containing R, G and NIR bands, and then applies channel blending and linear contrast enhancement on a pixel-by-pixel basis. Processed results from a sample image captured over an active bushfire show the practicality and efficiency of this solution. Compared to other image enhancement solutions using coincident multi sensor image capture, this method does not require any image co-registration between NIR and visible bands which results in a simple image processing methodology and can therefore be implemented in real time applications. Obviously, the approach depends strongly on the density of the smoke/haze particles and would fail for scenes covered by dense smoke.

REFERENCES

[1] A. J. Cox, A. J. DeWeerd, and J. Linden, "An experiment to measure mie and rayleigh total scattering cross sections," Am. J. Phys. vol.70, 620 (2002).

[2] N. Salamati, A. Germain, and S. Süsstrunk, "Removing shadows from images using color and near-infrared," Proc. IEEE Int. Conf. on Image Processing (ICIP), 1713-1716 (2011).

[3] C. Feng, S. Zhuo, X. Zhang, L. Shen, and S. S¨usstrunk, "Nearinfrared guided color image dehazing," Proc. IEEE Int. Conf. on Image Processing (ICIP), 2363–2367 (2013).

[4] L. Schaul, C. Fredembach, and S. S¨usstrunk, "Color image dehazing using the near-infrared," Proc. IEEE Int. Conf. on Image Processing (ICIP), 1629–1632 (2009).

[5] K. He, J. Sun, and X. Tang, "Single image haze removal using dark channel prior," IEEE Transactions on Pattern Analysis and Machine Intelligence, vol. 33, no. 12, 2341-2353 (2011).

[6] J. Zhang, "Multi-source remote sensing data fusion: status and trends," International Journal of Image and Data Fusion, vol.1, 5-24 (2010).

[7] M. Chabok, "Eliminating and Modelling Non-metric Camera Sensor Distortions Caused by Sidewise and Forward Motion of the UAV," Int. Arch. Photogramm. Remote Sens. Spatial Inf. Sci., XL-1/W2, 73-79 (2013).

[8] K. Gudnayak, P. Panda, and N. Panda, "A survey on image dehazing methods," International Journal of Engineering Research and Technology (IJERT), vol. 2, issue 10, 462-466 (2013).

[9] R. Blum and Z. Liu, [Multi-sensor image fusion and its applications], Boca Raton, FL: CRC Press (2006).

[10] Christi K. Madsen, Jian H. Zhao. [Optical Filter Design and Analysis: A Signal Processing Approach], John Wiley & Sons, Inc., NY. (1999).